

Plasmonic-catalytic Nanoparticles for the Hydrogen Evolution Reaction

Master's program in chemistry and molecular science
Study tracks Advanced spectroscopy in chemistry
Master's thesis

Author:
Md Mofakkharulhashan

Supervisor
Pedro H. C. Camargo

Examiners:
Pedro H. C. Camargo
Markku Vainio

University of Helsinki
Faculty of science
Helsinki 2024

Faculty: Faculty of Science
Degree programme: Chemistry and Molecular Science
Study track: Advanced Spectroscopy in Chemistry
Author: Md Mofakkharulhashan
Title: Plasmonic-catalytic Nanoparticles for the Hydrogen Evolution Reaction
Level: Master's thesis
Month and year: June 2024
Number of pages: 60+24
Keywords: Nanoparticles, Plasmonic, electrocatalyst, Noble metal, sustainability, catalysis
Supervisor: Pedro H. C. Camargo
Where deposited: Helsinki University Digital Archives HELDA/e-thesis
Additional information:
Abstract:
The development of active, stable, and cost-effective electrocatalysts for the hydrogen evolution reaction (HER) is paramount for the large-scale deployment of hydrogen-based clean energy technologies. Despite its apparent simplicity, the HER serves as a bridge between fundamental electrocatalysis research and practical catalyst design. Water splitting, a highly efficient and environmentally friendly method for hydrogen production, necessitates a stable, active, and abundant catalysts. While platinum (Pt)-based materials reign supreme in acidic electrolytes for their exceptional HER efficiency and durability, their scarcity and high-cost limit their widespread application. This study introduces a strategy to decrease the Pt loading in the catalyst by developing nanoparticles containing an ultralow Pt loading supported on tungsten oxide ($W_{18}O_{49}$). Remarkably, the activity of this developed system approaches that of commercially available 20% (wt.) Pt/C catalysts, even with a noble metal content of less than 2 wt.%. Notably, the optimal sample, $Pt_{1.6}/W_{18}O_{49}$ (containing 1.6 wt.% Pt), demonstrates a superior Tafel slope and requires a mere 46 mV overpotential to achieve a current density of 10 mA cm^{-2}. This work suggests that catalyst design and controlled synthesis can promote the HER and facilitate faster electron transfer even at low Pt loadings. This system exhibits exceptional stability, maintaining its performance for over 24 hours without significant degradation. This synergistic approach, employing minimal Pt supported on a $W_{18}O_{49}$ matrix, paves the way for addressing real-world challenges in hydrogen production.

Acknowledgments

I would like to express my sincere gratitude to the master's program Advanced Spectroscopy in Chemistry (ASC) and its network of esteemed universities. This work was made possible by the generous funding from the Erasmus+ program of the European Union.

My deepest gratitude goes to Professor Pedro H.C. Camargo for his invaluable guidance and mentorship throughout this project. His constant support and accessibility were instrumental in its successful completion. I also extend my sincere appreciation to Dr. Hugo L. Sousa Santos for his insightful discussions and unwavering encouragement, which significantly aided my progress during both the internship and thesis research. Special thanks to my examiner Professor Markku Vainio for his valuable and insightful comments that helped to finalize the work. I also acknowledge the positive and collaborative environment fostered by the Plasmonic Lab's members, which provided invaluable support.

I owe my thanks to all my ASC friends in Helsinki and other universities for making this journey so memorable. On a broader academic scale, Special thanks go to my esteemed professors, colleagues, and friends in Bangladesh who played a crucial role in inspiring me to pursue a European master's degree, particularly during the application process. Professor Dr. Balaram Roy, Dr. Md. Nazim Uddin, and Dr. Md. Shamsuzzoha, your guidance and supports are profoundly appreciated.

Finally, I would like to express my sincere appreciation to my mother and brother. Their unwavering prayers and moral support have been a constant source of strength throughout my career.

This thesis is dedicated to the memory of my father.

Helsinki, June 2024
Md Mofakkharulhashan

Table of contents

Abstract……..……..i
Acknowledgments…..…….……..…ii
Table of contents…….……..iii
List of abbreviation……v
1 Introduction ……..……1
2 Literature review……..…4
2.1 Nanoparticle and Catalysis……..……..…..4
2.1.1 Pt Nanoparticle and Catalysis…….……7
2.2 Plasmonic materials …….……11
2.2.1 Basic concept of LSPR metals nanoparticle…….……..11
2.2.2 Non-noble metal plasmonic materials……16
2.2.2.1 WO_{3-x}-based materials…….……..20
2.3 Electrochemical hydrogen evolution reactions……..……28
2.3.1 Hydrogen Evolution Reaction…….……..29
2.3.2 Electrochemical parameters to evaluate HER catalyst.……31
2.3.2.1 Overpotentials ……31
2.3.2.2 Tafel slops……...33
2.3.2.3 Electrochemical Impedance Spectroscopy……33
2.3.2.4 Stability……35
2.3.2.5 Turnover frequency (TOF)……36
2.4 Final remark from the literature review……..……..37
3 The objective of the thesis……37
4 Experimental section……38
4.1 Materials……..……38
4.2 Synthesis……..……39

4.3 Characterization……..……39

4.3.1 Atomic Emission Spectroscopy ……..……..39

4.3.2 UV-Vis spectrometry and Diffuse reflectance spectrometry……..…41

4.3.3 Electron Microscopy ……..…43

4.3.3.1 Scanning Electron Microscopy…….……44

4.3.3.2 Transmission Electron Microscopy…… 45

4.3.4 X-Ray diffraction……..….47

4.3.5 Electrochemical Measurements…….…..….48

4.4 Result …….……..49

4.4.1 Atomic emission spectroscopy……..…….49

4.4.2 Structural characterization SEM and TEM of Pt-$W_{18}O_{49...}$……..…50

4.4.3 UV-Vis/DRS……..……51

4.4.4 X-ray diffraction (XRD). ……..……52

4.4.5 Raman spectroscopy……..…….53

4.4.6 X-ray photoemission spectroscopy (XPS)……..…….54

4.4.7 Electrochemical measurement……..……55

4.5 Discussion ……..…….59

4.6 Conclusion...……..…..…….60

5 References…….……61

Appendices

List of abbreviations

HER	Hydrogen evolution reaction
OER	Oxygen evolution reaction
SMSI	Strong metal-support interaction
LSPR	Localized surface plasmon resonance
HOMO	Highest occupied molecular orbital
LUMO	Lowest unoccupied molecular orbital
VB	Valence band
CB	Conduction band
RHE	Reversible hydrogen electrode
EIS	Electron impedance spectroscopy
CV	Cyclic voltammetry
LSV	Linear sweep voltammetry
TOF	Turnover frequency
DRS	Diffuse reflectance spectroscopy
XRD	X-ray Diffraction
SEM	Scanning electron microscopy
TEM	Transmission electron microscopy
UV-Vis	UV-Vis spectrophotometry
WE	Working electrode
RE	Reference electrode
CE	Counter electrode
MP AES	Microwave plasma atomic emission spectrometry
NIR	Near infrared region
DFT	Density Functional theory

1. Introduction

Global energy consumption has been on a steady rise for the past ten years, fueled by both industrial expansion and population growth. A recent study[1] predicts a significant rise in global energy consumption, reaching 30 Terawatt (TW) by 2050 compared to 16 TW in 2010. Currently, however, dependance on conventional sources like natural gas, coal, and oil remains high, accounting for roughly 80% of energy consumption. Renewable sources[2] such as wind, hydropower, and solar photovoltaics contribute only about 20%. Alarmed by the rising demand for energy, the scientific community is pushing the boundaries of clean technology. Their focus is on harnessing eco-friendly resources and diversifying the energy sources. This two-pronged approach aims to create a sustainable, long-term solution that combats environmental issues and mitigates the effects of global warming.[3] In the quest for environmentally friendly energy solutions to meet our rising consumption demands, molecular hydrogen emerges as a promising alternative for the next generation. Its clean-burning nature and potential for diverse applications make it a strong contender in the race for a sustainable future.[4,5] Because of potentially nonpolluting characteristics[6] (combustion byproduct is pollution-free water), renewability[7] and highest gravimetric energy density[8] make it a potential candidate for the low carbon future.[8,9] Despite the promise of hydrogen as a clean energy source, current production methods often rely on steam reforming of fossil fuels. This process not only consumes these finite resources, but also releases harmful CO_2 emissions. To truly achieve a renewable and clean energy future with a successful hydrogen economy, developing methods for hydrogen generation that don't emit toxic or unwanted gases is essential.[10]

Electrochemical water splitting for hydrogen generation has garnered significant attention due to its potential for being a low-cost, environmentally friendly, clean, and sustainable process. This technology offers a promising path toward a future powered by renewable energy.[11,12] While water electrolysis offers a promising path for clean energy production by splitting water into hydrogen and oxygen gas, the process requires an additional energy input to overcome an inherent energy barrier. This energy barrier, known as overpotential, hinders the efficiency of the reaction. Fortunately, catalysts play a crucial role in reducing this overpotential, allowing for the efficient production of hydrogen and oxygen gas.[13] Effective catalyst design for

electrochemical reactions hinges on achieving a delicate balance between several key surface properties. The ideal catalyst exhibits an optimal hydrogen binding energy, ensuring strong intermediate adsorption without hindering its subsequent release. This translates to a balance between the Gibbs free energy of adsorption and desorption. Additionally, modern catalyst development prioritizes high selectivity, Earth abundance, and the ability to function under mild conditions with minimal waste generation. However, it's important to remember that heterogeneous catalysis is inherently a surface-driven phenomenon. As a result, decreasing the size of the catalyst typically leads to a desirable increase in the surface-to-volume ratio, further enhancing its efficiency.[14]

Nobel metals, particularly platinum group metals (PGMs) like platinum (Pt), palladium (Pd), ruthenium (Ru), iridium (Ir), and rhodium (Rh), exhibit exceptional catalytic activity for the hydrogen evolution reaction (HER). This superior performance stems from their unique ability to achieve low free energy for hydrogen adsorption compared to other materials. Notably, the platinum surface displays a moderate M-H bond strength, which is a key factor contributing to its high catalytic efficiency in HER.[15] For platinum (Pt) catalysts employed in various reactions, the size, shape, and crystal phase are utmost factors influencing their catalytic activity. The ability to precisely control the exposure of active catalytic sites significantly influences performance by maximizing their accessibility to reactant molecules. By optimizing these parameters, scientist can effectively engineer Pt catalysts to maximize the number of exposed Pt atoms on the surface, thereby enhancing their overall catalytic activity.[16] The morphology of a catalyst plays a critical role in its performance as it dictates the arrangement of atoms on its surface. By strategically employing surfactants or reducing agents with varying reduction potentials, it is possible to tailor the catalyst's morphology to optimize its catalytic activity.[17]

While earth-abundant transition metal sulfates, nitrates, and phosphate[18] demonstrate promising catalytic activity for HER, Pt-based electrocatalysts currently reign supreme in terms of activity. However, their widespread application is hampered by the high cost and limited availability of platinum. Fortunately, strategies exist to mitigate these limitations. Utilizing supported materials and minimizing catalyst

loading by maximizing exposed surface area can significantly enhance HER activity with these more affordable alternatives.

This literature review provides a comprehensive overview of nanomaterials and their catalytic properties, with a specific emphasis on the unique characteristics of Pt nanomaterials. Additionally, it delves into the fundamentals of plasmonic and non-noble plasmonic materials. Finally, the review focuses on the electrochemical HER. The experimental section details the synthesis and characterization of catalytic plasmonic materials. Our electrochemical studies confirm that light irradiation can significantly enhance the activity of these materials. Notably, the use of light allows for a substantial reduction in the amount of Pt-supported plasmonic material required for efficient HER.

2. Literature Review

2.1 Nanomaterials and catalysis

The term "nano," derived from the Greek word for "dwarf," emerged in the 1960s, marking a paradigm shift in scientific exploration. Prior research had extensively examined the behavior of atoms and molecules within macroscopic structures. However, the latter half of the 20th century witnessed a burgeoning interest in the unique properties exhibited by nanoscale, non-molecular assemblies containing thousands of atoms. Notably, the visionary physicist Richard Feynman posited that the study of materials at the nanoscale, specifically those ranging from a few to a hundred nanometers, held the potential to unlock revolutionary technological advancements.[19]

Scientific focus has shifted towards understanding the unique phenomena and properties of nanomaterials. Particularly, at the nanoscale, materials like semiconducting quantum dots exhibit a fascinating property their physical and chemical characteristics are dictated not only by their composition but also by their size and shape. This dependence on size and shape opens doors to a new level of control over material properties, paving the way for innovative technological advancements. For instance, by precisely controlling the size and shape of quantum dots, scientists can tailor their light-emitting properties, enabling the development of next-generation displays and solar cells. Similarly, manipulating the size and shape of nanoparticles can influence their catalytic activity, leading to the design of more efficient catalysts (Figure 1) for clean energy production and environmental remediation.[19] For instance, the performance of platinum (Pt) as a catalyst for the HER, exhibits significant activity differences depending on its morphology. Notably, Pt arranged in a nanoarray structure demonstrates considerably higher performance compared to flat films. This observation highlights the profound influence of nanoscale organization on material properties, a key concept in nanotechnology.[20] Metal nanoparticles exhibit a remarkable tunability of their properties, selectivity, and catalytic activity. This exceptional control originates from the ability to manipulate their size and morphology.[21–25]

Homogeneous catalysts, those sharing the same phase as their reactants, offer several advantages. Their readily accessible catalytic sites enable extensive control over reaction pathways. Additionally, these systems are often considered highly tunable, with ligand and metal modifications readily optimizing their performance. However, a major limitation of homogeneous catalysts lies in their separation from the reaction mixture. Even trace amounts of metal contamination can significantly impact industrial processes. To address this challenge, chemists have increasingly explored heterogeneous catalysts, offering a more practical solution for large-scale applications.[26,27]

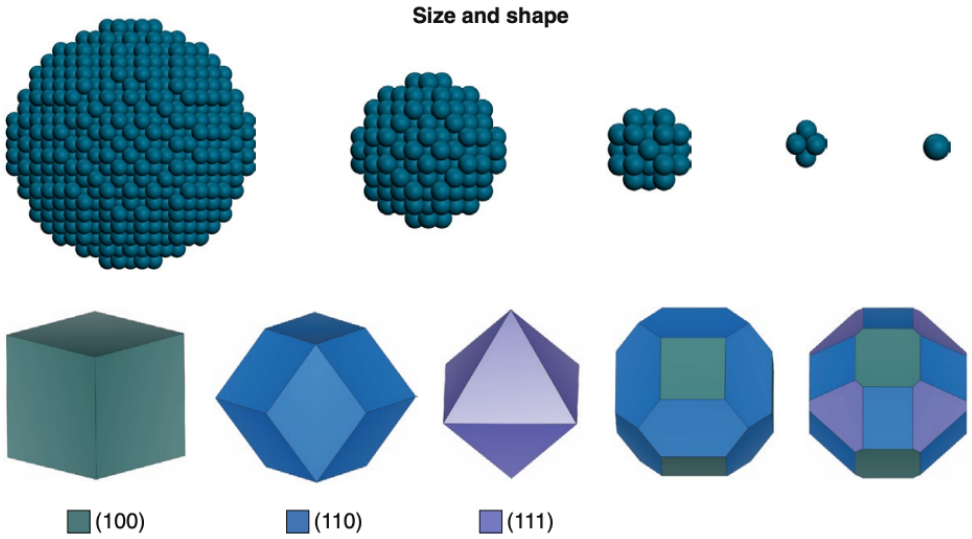

Figure 1: Schematic representation of nanoparticle with size and morphologies. (Reproduced with permission).[28]

In heterogeneous catalysis, nanostructured materials are particularly attractive due to their superior catalytic activity. This enhanced performance is directly linked to the increased active surface area that arises from the smaller size of these materials. A larger surface area provides more reaction sites for the reactants to interact with the catalyst, ultimately leading to a faster and more efficient reaction.[29] Heterogeneous catalysts play a crucial role in numerous chemical reactions by providing well-defined adsorption sites. These sites facilitate the reduction of activation energy, thereby accelerating the reaction. However, the electronic properties of the catalyst surface are not uniform. They can vary significantly depending on the crystal facet exposed, which determines the arrangement of atoms on the surface.[30] Research suggests that the

location of metal atoms on a catalyst surface can significantly impact their activity. Face sites, defined as the flat atomic planes of the material, have been shown to exhibit different catalytic behavior compared to edge sites[3], which are the junctions between these planes. For instance, a study by Tan et al. demonstrated that face sites (specifically the [100] plane of Pt) can contribute up to 75% of a catalyst's activity, while edge sites displayed minimal activity in their experiment.[31] This research explores a novel class of catalysts characterized by cooperative interactions between multiple immobilized species on their surface. These multifunctional catalysts demonstrate exceptional performance in one-step synthesis reactions.[32]

Nanoparticles significantly enhance the catalytic process by increasing the active particle area of the catalyst. This expanded surface area dramatically improves the contact between the reactants and the catalyst surface. This phenomenon closely resembles the behavior of homogeneous catalysts, where reactants are uniformly surrounded by catalyst molecules, leading to a more efficient reaction.[26] Heterogeneous catalysts offer a distinct advantage in separation processes due to their inherent insolubility in the reaction solvent. This characteristic simplifies catalyst recovery after the reaction. Additionally, by precisely controlling the size and shape of these catalysts, scientists can fine-tune their chemical and physical properties, optimizing their performance for specific reactions.[26] However, the catalytic performance can be improved by exposing the crystal plane because different plane introduces different atomic arrangements (Figure 1) that enhance the electronic interactions. Special morphologies, such as nano frames[33–35], nanocages[36], branched structure[37], convex structure[38,39], ultrathin nanowire[40–42] and core-shell structures show exceptionally higher activity than their unique nanostructure. For example, Pt nanoparticles with the [110] crystal plane orientation have demonstrated superior catalytic activity for the hydrogen evolution reaction (HER). This specific orientation allows for a significant reduction in the amount of Pt metal required for efficient catalysis.[43,44] Consequently, this focus on the unique properties of nanomaterials has driven extensive research into manipulating their surface structures. A key area of investigation involves utilizing less metal while maintaining desired functionality. One approach to achieving this goal involves modifying the morphology, or shape, of nanoparticles using halide additive[45], surfactants[46], and reducing agents of different

reducing power[47]. Unlike some other materials, the ability of certain metals to form diverse shapes is restricted. This limitation arises from two key factors: internal strain and susceptibility to oxidation etching.[48]

Despite the remarkable capabilities of advanced nanotechnology in synthesizing materials with desired size, shape, and composition, significant scientific hurdles remain in achieving precise control over the morphology and properties of nano-catalysts. This lack of complete control presents a critical challenge in tailoring these catalysts for optimal performance in specific applications.[49]

2.1.1 Platinum Nanoparticles

In 1839, William Grove, a pioneering scientist, laid the foundation for fuel cell technology. He achieved this by utilizing a platinum (Pt) wire as an electrode in a sulfuric acid solution. This innovative setup not only produced electricity but also served as the first model for future fuel cells.[50] Platinum (Pt) has emerged as a material of significant research interest due to its exceptional catalytic activity and stability in acidic electrolytes. However, single-atom Pt catalysts, while unsupported and offering high dispersion, necessitate high Pt loadings. This is a consequence of their inherently high overpotential, an energy barrier that hinders efficient catalysis. Unfortunately, a high concentration of Pt particles can lead to agglomeration, which reduces the overall surface area and ultimately diminishes the catalyst's activity.[51] Carbon support materials play a crucial role in mitigating the limitations associated with metal catalysts. Their high surface area provides ample space for the dispersion of metal nanoparticles, maximizing their active sites. Additionally, the suitable porosity of these supports facilitates the mass transport of reactants and products. Furthermore, their high corrosion resistance ensures catalyst stability. Ultimately, these combined properties of carbon supports contribute to enhanced electron transfer processes, leading to improved catalytic activity.[52] Since the 1990s, carbon-supported materials have emerged as a mainstay in various fields due to their compelling combination of properties. These materials boast low cost, high electrical conductivity, and a large surface area, making them highly versatile and advantageous for numerous applications.[53] Enhanced corrosion resistance positions oxidative materials as

attractive candidates for catalyst supports.[54,55] Among sp^2-bonded materials, graphene stands out due to its exceptional combination of properties. Notably, its ultra-high specific surface area, unique ultrathin sheet structure, and remarkable physical stability position it as a highly promising material for various applications.[56] Studies have demonstrated that reduced graphene oxide (rGO) exhibits a superior surface area compared to carbon black and carbon nanotubes. This enhanced surface area makes rGO a more effective catalyst support material.[57] Supported platinum nanoparticles tend to aggregate due to surface oxidation on the carbon support. This oxidation process can adversely affect the performance of the catalyst in several ways. First, it can reduce the overall surface area of the platinum available for reaction, as the nanoparticles clump together. Second, oxidation can alter the electronic properties of the platinum surface, diminishing its catalytic activity. Finally, in the case of platinum alloys, oxidation may preferentially affect one component of the alloy, leading to a loss of the synergistic effects that contribute to the catalyst's function.[58] Optimizing catalyst and carbon support design remains a significant challenge for the scientific community.[59]

Table 1 Carbon-based support materials.

Supporting materials with surface area, particle size, and conductivity

Carbon support	Surface area ($m^2\ g^{-1}$)	Particle size (nm)	Conductivity ($S\ cm^{-1}$)	Reference
Carbon black	254	30	2.77	82
Carbon nanotubes	50-1000	1-5 μm	0.3-400	83-85
Carbon nanofiber	50-1000	30-100 μm	200-900	84,86,87
Carbon nanohorns	300-400	40-50 nm	4.95-7.07	88
Graphene	>2000	10-20 nm	10^3- 10^4	88,89

Generally, Pt-C is used as a commercial electrocatalyst, but scarcity and high cost limited its application.[60,61] However, because of carbon corrosion nowadays researchers trying to replace carbon-supporting material as it affects a serious amount of Pt loss, cell performance decay, and the stability of the catalyst.[62] In response to these challenges, metal oxides such as WO_3, TiO_2, and IrO_2 have emerged as promising

candidates due to their inherent stability in harsh oxidative environments. This characteristic makes them suitable replacements for more traditional materials that degrade under these demanding conditions.[63] Wu et al. identified titanium dioxide (TiO_2) as a promising material for catalyst supports due to its unique nanostructured geometries, including nanoarrays, nanowires, and nanosheets.[64] One limitation of TiO_2 is its insufficient electrical conductivity. Fortunately, other stable titanium oxides exhibit considerably higher conductivity, making them more attractive for certain applications. Doping TiO_2 with specific elements further enhances its performance, improving both its activity and mitigating the agglomeration effect.[65,66] Studies have demonstrated that titanium dioxide (TiO_2) based support materials exhibit a stronger interaction with noble metals compared to carbon-based supports. This enhanced interaction, known as strong metal-support interaction (SMSI), can significantly impact the performance of catalysts.[67,68]

Monoclinic sub-stoichiometric $W_{18}O_{49}$ possesses a unique structure characterized by edge-sharing, distorted W-O octahedra. This configuration gives rise to a remarkable number of oxygen vacancies within the material. Notably, these vacancies endow $W_{18}O_{49}$ with tunable electronic properties, making it a promising candidate for various applications.[69–71] Extensive experimental and theoretical investigations have revealed the promising role of oxygen vacancies in water splitting for the HER. These vacancies act as excellent adsorption sites for reaction intermediates, such as H, significantly enhancing the catalytic activity. Consequently, materials with engineered oxygen vacancies are considered highly promising candidates for bifunctional electrocatalysts in water-splitting systems.[72,73]

Transition metal carbides (TMCs) have emerged as attractive support materials for catalysts due to their unique combination of properties. Notably, their high electrical conductivity facilitates efficient electron transfer between the catalyst and the reactants. Additionally, TMCs exhibit remarkable stability in acidic environments, making them suitable for a wide range of catalytic applications.[74] Building upon the potential of transition metal carbides, Tang et al. investigated their synergy with platinum for HER. Their research revealed that Pt/WC hollow spheres exhibited superior HER performance compared to traditional Pt/C catalysts.[75] The Ti3C2-

supported Pt/Ni composite exhibits demonstrably lower Tafel slopes and overpotentials compared to commercially available Pt/C catalysts.[76] Two-dimensional (2D) support materials, like Mxenes, play a crucial role in facilitating reaction kinetics. They achieve this by offering abundant active sites, which enhance the transfer of charge between the deposited nanocrystals and the support material itself.[77]

Beyond selecting suitable support materials, precise control over the morphology of Pt nanoparticles plays a crucial role in catalyst performance. This study demonstrates that the use of nanotubes (NTs)[78], nanowire (NW)[79], nanodendrite (ND)[80], and porous structures[81] significantly enhances the density of exposed Pt active sites, effectively mitigating aggregation. This translates to improved catalytic durability and activity.[82] Research continues to explore the use of earth-abundant metals as catalyst supports. By forming alloys with these metals, scientists aim to modulate reaction pathways and suppress unwanted side reactions. This approach ultimately improves catalytic performance, enabling systems to function effectively with significantly reduced Pt content.[83]

The utilization of a single catalyst can lead to the adsorption of electrocatalytic oxidation intermediates on its surface, hindering further reaction progress. The introduction of a second metal can address this limitation by promoting the desorption of these intermediates. This regeneration of active sites ultimately enhances the overall reaction kinetics.[84] Recent research has explored Pt-M (where M represents transition metals like Ru, Pd, Ni, and Cu) catalysts for their ability to leverage underutilized sites on noble metals like Pt. The open, three-dimensional geometry of these bimetallic structures is believed to enhance interaction between the components, potentially leading to improved catalytic performance.[85]

2.2 Plasmonic materials

This chapter delves into the fundamentals of plasmonic, the interaction of light with matter, and its potential application in converting solar energy into chemical energy. We will explore the concept of localized surface plasmon resonance (LSPR), a key phenomenon in plasmonic. Additionally, we will examine non-metal plasmonic materials as a promising alternative to traditional materials. Finally, the chapter will discuss the significant advantages of combining plasmonic materials with catalysts for enhanced solar energy conversion efficiency.

2.2.1 Basic concept of LSPR effect of metal NPs

Plasmonic materials exhibit a fascinating phenomenon known as Localized Surface Plasmon Resonance (LSPR). It arises from the interaction between incident light and the collective oscillation of electrons on the metal surface. As described by Gustav Mie's theory, this resonance occurs when the frequency of the incoming light matches the natural oscillation frequency of the electrons, leading to a synchronized and amplified oscillation against the restoring force of the metal lattice.[86] The restoring force, often referred to as the Coulombic restoring force, acts on these displaced electrons, leading to a characteristic resonant frequency. (Figure 2).[87]

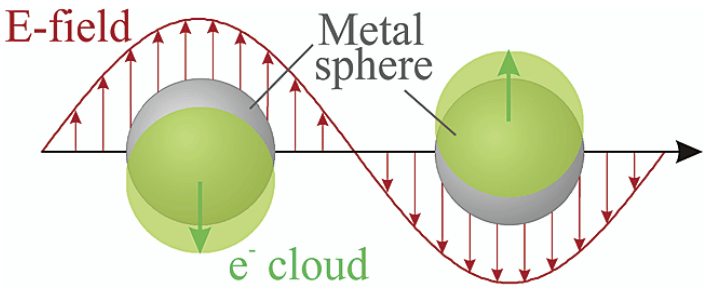

Figure 2: Schematic representation of the plasmon oscillation of electron showing the displacement of charge related to the nucleus. (Reproduced with permission).[87]

Two primary mechanisms emphasize plasmonic catalysis photothermal localized heating and activation of reactant molecules by localized surface plasmon resonance (LSPR)-generated hot electrons. [88–90]. As illustrated in Figure 3a-d, the initial

population of electronic states is depicted by the gray area. Hot electrons and holes are subsequently generated, represented by red and blue, respectively (Figure 3b). These hot carriers can decay through two main pathways (discussed in detail later). Radiative decay involves the emission of light, while non-radiative decay, specifically through Landau damping, generates additional hot carriers. These newly created hot carriers then undergo further energy redistribution through electron-electron scattering, ultimately achieving a Fermi-Dirac distribution. Finally, the remaining energy dissipates into the surrounding environment via thermal conduction.[91]

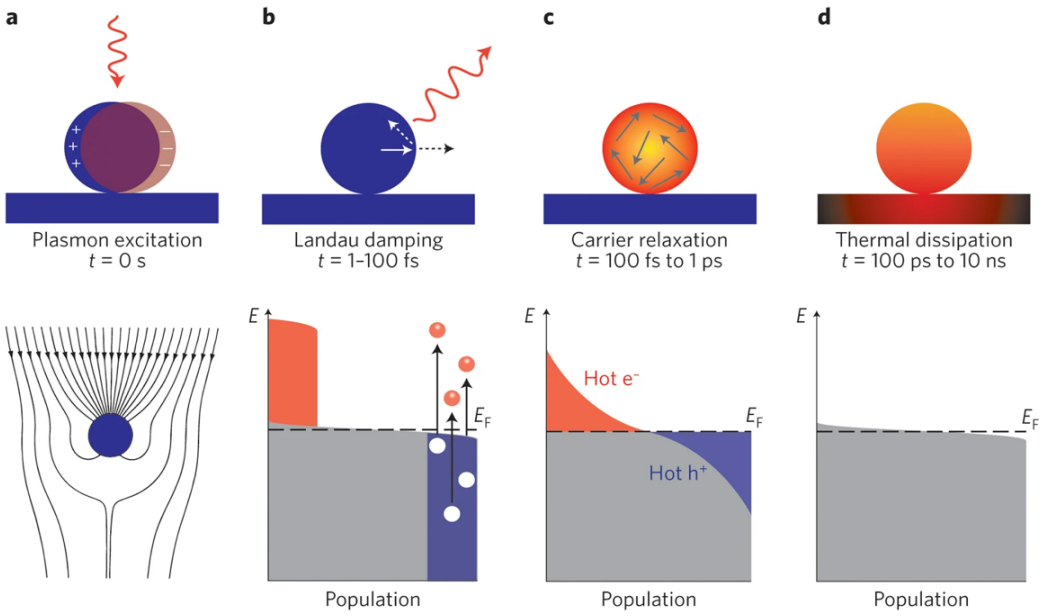

Figure 3: Photoexcitation and relaxation of metallic nanoparticles. (Reproduced with permission).[91]

Conversely, the radiative decay process facilitates intermolecular transitions (Figure 4a). These transitions involve the energy gap between a molecule's highest occupied molecular orbital (HOMO) and its lowest unoccupied molecular orbital (LUMO), which essentially represent the energy levels of the electrons that participate in chemical reactions. Several research suggests that in gas and liquid phases when a molecule adsorbs onto a plasmonic surface, the HOMO-LUMO energy gap narrows due to electronic interactions between the molecule and the plasmonic surface. This narrowing of the energy gap can significantly influence various molecular properties, including electrical conductivity, reactivity in chemical reactions, and light absorption properties. For instance, a smaller HOMO-LUMO gap can enhance a molecule's

electrical conductivity by facilitating the movement of electrons. Likewise, it can influence a molecule's reactivity by making it easier for electrons to be excited or transferred during chemical reactions. Additionally, a narrowed HOMO-LUMO gap can affect a molecule's light absorption properties, potentially making it more susceptible to absorbing light of specific wavelengths.[92]

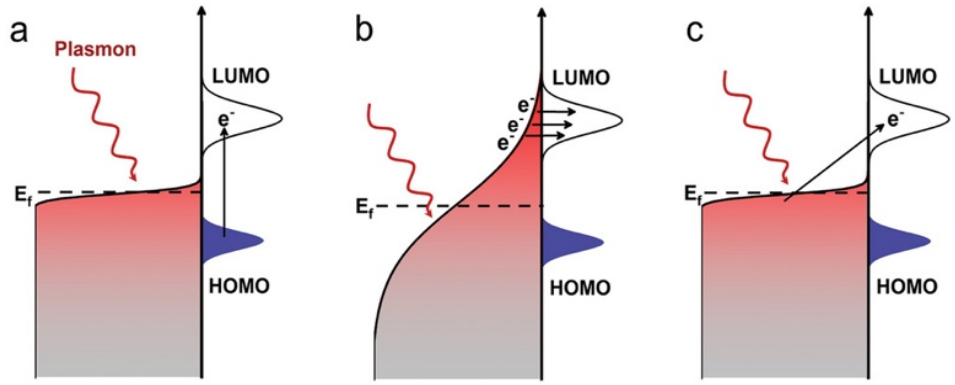

Figure 4. (a) Plasmon-induced intramolecular charge transfer mechanism; (b) indirect charge transfer and (c) direct charge transfer mechanism. (Reproduced with permission).[92]

Plasmonic surfaces offer a unique mechanism for energy transfer to adsorbed molecules through vibrational excitation. This process leverages the re-emitted energy from the plasmon decay and is facilitated by two primary charge transfer pathways, indirect and direct (Figure 4b-c). In the indirect mechanism, the decayed plasmon generates a non-equilibrium distribution of energetic "hot" electron-hole pairs within the metallic nanostructure. Electrons possessing sufficient energy can then be directly injected into the Lowest Unoccupied Molecular Orbital (LUMO) of the adsorbed molecule (Figure 4b). Conversely, the direct mechanism involves a more efficient transfer, where a hot electron directly tunnels from the plasmon to the LUMO of the adsorbed molecule, inducing vibrational excitation (Figure 4c). This ability to tailor energy transfer through these mechanisms has significant implications for various applications, including photocatalysis and sensing. [92]

As illustrated in Figure 5, the proposed mechanism relies on the interplay between plasmon-induced hot charge carriers and adsorbed reactants. This interaction is hypothesized to be the critical driving force behind the process. Initially, a molecule sits at its equilibrium position, requiring activation energy (E_a) to dissociate. Upon photoexcitation of the plasmonic nanoparticle, energy is transferred to the molecule, promoting it to an excited state. This excited molecule moves along the potential energy surface, potentially encountering another reactant and undergoing a chemical reaction. As the hot charge carrier returns to its ground state, the excess vibrational energy can further promote the transformation of the reactant or intermediate on the surface, facilitating subsequent reactions.[89] Furthermore, these LSPR-generated hot electrons and holes (hot charge carriers) exhibit a remarkable ability to influence chemical reactions. Studies suggest that these hot charge carriers can manipulate reaction selectivity and reaction rates, offering exciting possibilities for designing more efficient and targeted catalysts.[91]

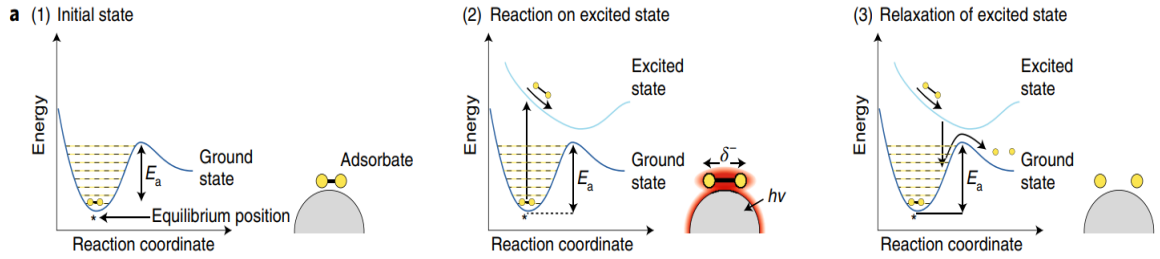

Figure 5: Electronic transition mechanism of plasmon-mediated bond activation. (Reproduced with permission).[89]

Plasmon-enhanced hot electron generation offers a distinct advantage over direct excitation. Direct excitation necessitates high light intensity, whereas plasmonic systems can generate hot electrons efficiently even with moderate light.[93,94] As illustrated in Figure 6, the plasmon excited state can undergo two competing decay pathways. Research suggests that the dominant decay mechanism, radiative or non-radiative, depends on the size of the nanoparticle.[95–98] Metal nanostructures exhibit a phenomenon known as non-radiative decay. This process involves the relaxation of excited electrons through inter-band or intra-band transitions. In inter-band transitions, the electron jumps from the conduction band to a lower energy level, such as the valence band. Conversely, intra-band transitions occur within the conduction

band itself, where the electron loses energy through interactions with phonons (vibrations) in the lattice.[95] Hot electron injection is a critical concept in unraveling the mechanisms behind plasmon-assisted chemistry. Interestingly, the efficiency of this process can be significantly influenced by tailoring the properties of nanomaterials. By manipulating factors like size, shape, and the surrounding environment, researchers can fine-tune hot electron injection, paving the way for advancements in plasmon-driven applications.[99]

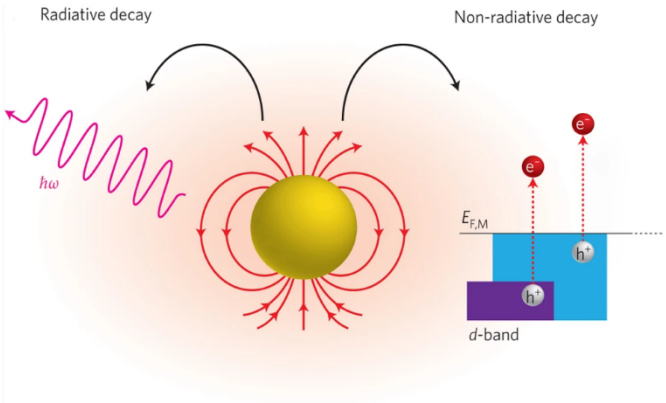

Figure 5: LSPR decays radiatively and non-radiatively via hot electrons. (Reproduced with permission)[95]

The optical properties of a material are dictated by its dielectric function, which arises from the interplay of free electrons and the excitation of bound electrons (induced by photons with energy exceeding the bandgap energy).[100]

From the Drude-Lorentz model dielectric function for solid materials is as follows:

$$\varepsilon(\omega) = \varepsilon_1(\omega) + i\,\varepsilon_2(\omega) \qquad (1)$$

where, $\varepsilon(\omega)$ is the dielectric function, $\varepsilon_1(\omega)$ is real, and $i\,\varepsilon_2(\omega)$ imaginary part with the frequency of incident light is given by ω. The real part of this model represents the polarizability of the materials and the imaginary part absorption of photons inside the medium concerning the frequency of light.[101] When *d* to *s* transition is accessible ε_2 is high and strong resonance can be observed when ε_1 is negative and ε_2 small value.[102,103]

The real and imaginary parts can therefore be given by,

$$\varepsilon_2(\omega) = \varepsilon_\infty - \frac{\omega_p^2}{\omega^2+\gamma_d^2} \quad (2)$$

and

$$\varepsilon_2(\omega) = \frac{\omega_p^2\gamma_d}{\omega(\omega^2+\gamma_d^2)'} \quad (3)$$

respectively. Where, ε_∞ is the high-frequency dielectric function, ω_p plasma frequency and γ is the damping factor used to describe the free electron scattering. Free electron carrier concentrations are related to the frequency functions can be shown by the equation as follows:

$$\omega_p = \sqrt{\frac{ne^2}{m_e\varepsilon_0}} \quad (4)$$

In this equation, n is the free carrier concentration, e is the free carrier charge, m_e effective mass and ε_0 is the dielectric constant of the medium.[104] Study suggested that the plasmonic property of materials can be evaluated by the dielectric function, Peng et al. found that materials with larger Electric field enhancements have negative real and positive imaginary parts though absolute values are opposite.[105,106]

2.2.2 Non-metal plasmonic materials

Transition metals like tungsten (W), molybdenum (Mo), copper (Cu), zinc (Zn), tin (Sn), and silicon (Si) are attracting significant interest as alternatives to scarce and expensive noble metals in plasmonic. These earth-abundant elements, often combined with non-noble metal nitrides and chalcogenides, exhibit promising catalytic, magnetic, and optical properties. Their potential as plasmonic materials stems from their ability to overcome limitations associated with noble metals, such as scarcity, high optical loss, restricted light-scattering wavelength range, and substantial cost (Figure 7).[107]

Recent research has identified non-noble metal catalysts as promising alternatives to their traditionally employed noble metal counterparts. This shift is driven by the significant cost advantage offered by non-noble metals. However, despite exhibiting excellent performance in certain applications, these non-noble materials still face challenges. The ability to synthesize these catalysts with targeted nanostructures and achieve precise control over their plasmonic properties remains a critical hurdle. Overcoming this challenge is essential for the widespread adoption of non-noble metal catalysts.

Degenerately doped semiconductors offer a unique approach to sustaining LSPR. By precisely controlling the doping level, these materials achieve LSPR despite having lower carrier concentrations compared to noble metals like gold and silver (whose free electron concentrations reach 5.9×10^{22} cm^{-3}).[108] Unlike noble metals, which primarily resonate in the lower wavelength visible light range, non-noble plasmonic materials exhibit resonance across a broader spectrum, encompassing the visible, near, and even mid-infrared regions.[107] Doping semiconductor materials not only broaden the scope of potential plasmonic materials, but also extends their light absorption spectrum into the infrared region. This expanded functionality opens doors for exciting applications like photothermal cancer therapy.

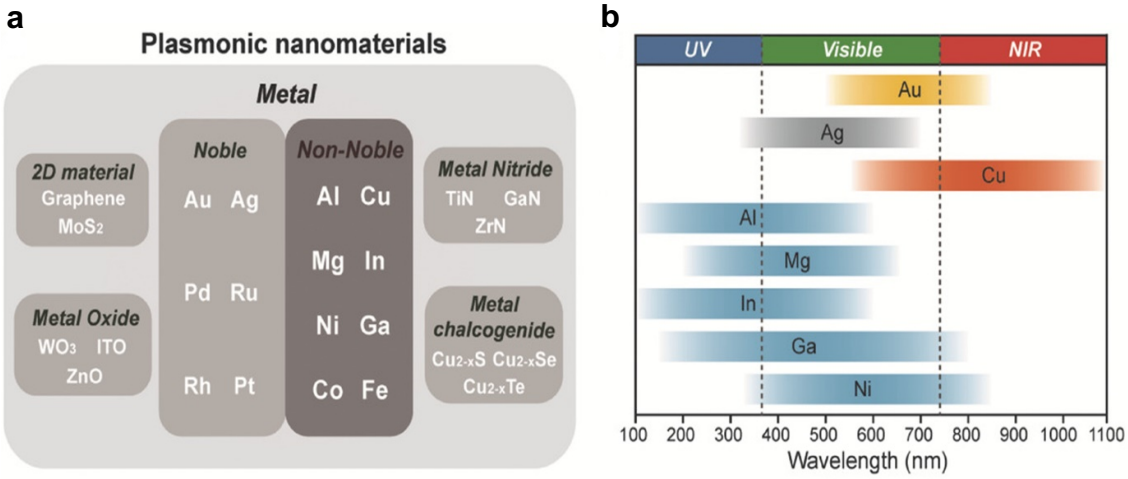

Figure 6: (a) Plasmonic materials including Metal, non-metals, 2D materials, metal nitride, chalcogenide, and oxides, (b) spectral ranges from ultraviolet (UV) to near-infrared region (NIR). (Reproduced with permission).[107]

Despite inherently low free carrier concentrations (below 10^{12} cm^{-3}), semiconductors offer remarkable flexibility. By manipulating their stoichiometry (elemental composition ratios) and dopant concentration (intentional impurities), their electrical properties can be precisely tailored.[109] A high concentration of free carriers is crucial for achieving a strong plasmonic response in doped semiconductors. These free carriers, which can be electrons (n-type) or holes (p-type), can significantly influence the host material's structure. This influence can manifest through distortion or hybridization of the lattice, potentially impacting the lattice itself and the mobility of free ions within it.[110]

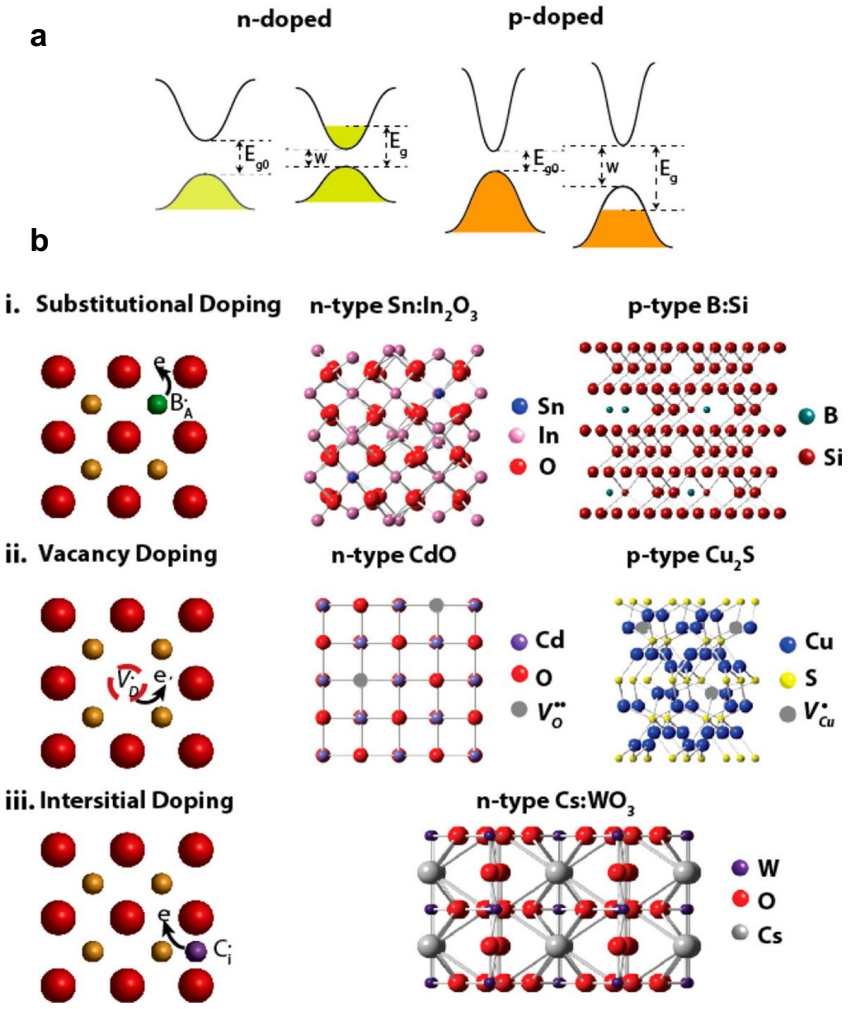

Figure 7: (a) Schematic of band structure of n-type and p-type materials and influence of doping of host lattice. (b) Scheme of common doping mechanisms of n-type and p-types with host cations and anions and corresponding examples. (Reproduced with permission).[110]

The scientific literature details three primary methods for introducing free carriers into semiconductors extrinsic substitutional doping, intrinsic doping by lattice vacancies, and, to a lesser extent, extrinsic interstitial doping (Figure 8). Each approach strategically modifies the crystal lattice of the semiconductor to alter its electrical conductivity.[110] The Burstein-Moss effect plays a crucial role in how doping influences the band gap of a material. This effect describes how the band gap, which represents the energy required to excite an electron from the valence band to the conduction band, can be modified by free carrier concentration. As illustrated in Figure 8a, n-type doping shifts the Fermi level (E_g) closer to the conduction band (CB), leading to a reduction in the band gap W. Conversely, p-type doping pushes the Fermi level down towards the valence band (VB), resulting in an increased band gap. This phenomenon highlights how doping allows for the tailored manipulation of a material's optical properties through controlled changes in free carrier concentration.[109]

Figure 8b illustrates the two main doping mechanisms.

I. Extrinsic Doping: This method involves introducing aliovalent atoms (atoms with a different valence) into the semiconductor lattice. These dopant atoms contribute free electrons (n-type) or holes (p-type) to the host material. Examples include tin-doped indium oxide ($Sn:In_2O_3$) for n-type transparent conductive oxides (TCOs) and boron-doped silicon (B:Si) for p-type semiconductors. Both n-type and p-type doped materials are crucial components in solar cells and electronics.

II. Intrinsic Doping: This mechanism relies on imperfections within the semiconductor lattice itself. Lattice vacancies, which can be missing anions (negatively charged ions) or cations (positively charged ions), can create free carriers. Oxygen-deficient metal oxides like MoO_{3-x} and WO_{3-x} become n-type due to these vacancies, while cation deficient chalcogenides like $Cu_{2-x}S$ and $Cu_{2-x}Se$ become p-type.[111–113] LSPR excitation is contingent upon a sufficient concentration of free carriers within the material. In non-stoichiometric materials, these free carriers can originate from variations in the oxidation state. This deviation from perfect stoichiometry can introduce either extra

electrons or holes into the conduction and valence bands, respectively. These introduced carriers subsequently modify the Fermi level and band gap of the material, enabling the conditions necessary for LSPR.

III. Extrinsic interstitial doping, while less frequently employed, can also introduce additional electrons to maintain plasmonic effects. This approach is particularly successful with materials possessing open crystal structures, such as MoO_3 and WO_3. In these materials, the small radius of the dopant ions facilitates interactions that promote electron delocalization within the conduction band.[114]

One study by Cheng et al. highlighted a potential challenge for plasmonic materials using non-noble semiconductors. Their research suggests that certain synthesis routes may introduce surface-capping agents that hinder the surface functionality of these materials.[115] Recently, various earth-abundant plasmonic materials have been investigated for example MoO_{3-x} nanosheets,[151] hybrid mesoporous $WO_{2.83}$[116], Pd/H_xMoO_3[117], $Rb_{0.33}WO_3$[118], Cu_7S_4/Pd heterostructure[119] Pd/Cu_{2-x} nanowires hybrids[120] rationally been prepared and show efficient and enhanced catalytic activity towards hydrogen evolution reactions, hydrogenations, selective oxidation of benzyl alcohol, CO_2 reduction and so on. Here we will only focus on WO_{3-x} based plasmonic materials.

2.2.2.1 WO_{3-x} based materials.

Tungsten trioxide (WO_3), an n-type semiconductor with a band gap of 2.8 eV, exhibits sub-stoichiometry (pioneered by Glemser and Sauer) and a diverse range of applications. These applications capitalize on its unique electrochromic and photochromic properties. WO_3 finds promise in photoelectrochemical water splitting and gas sensing due to its ability to manipulate light and respond to specific gas molecules.[121] This material holds promise due to its combination of self-doping characteristics, oxygen deficiency with abundant defect sites, and outer delocalized d-electrons that facilitate the LSPR.[112]

The introduction of vacancies within a metal lattice significantly impacts its electronic properties. These vacancies create variations in the electronic states, ultimately leading to an increase in the concentration of free carriers within the material. This phenomenon translates to enhanced conductivity, making the metal more suitable for applications in electrochemistry and photochemistry where efficient charge transport is crucial.[122] WO_3 exhibits a unique characteristic the ability to lose oxygen atoms from its crystal structure ($0 < x \leq 0.28$). This gradual oxygen elimination, known as sub-stoichiometry, imparts metal-like properties to the material. Notably, specific compositions within this range, such as $WO_{2.9}$ ($W_{20}O_{58}$), $WO_{2.83}$ ($W_{24}O_{68}$), and $WO_{2.72}$ ($W_{18}O_{49}$), fall under the category of Magneli phases.[116] Extended oxidation can transform these materials into stoichiometric WO_3 (tungsten trioxide). Interestingly, research suggests that smaller particle sizes lead to an increased band gap in WO_3. This phenomenon results in a blue shift of the material's photon absorption spectrum.[123,124]

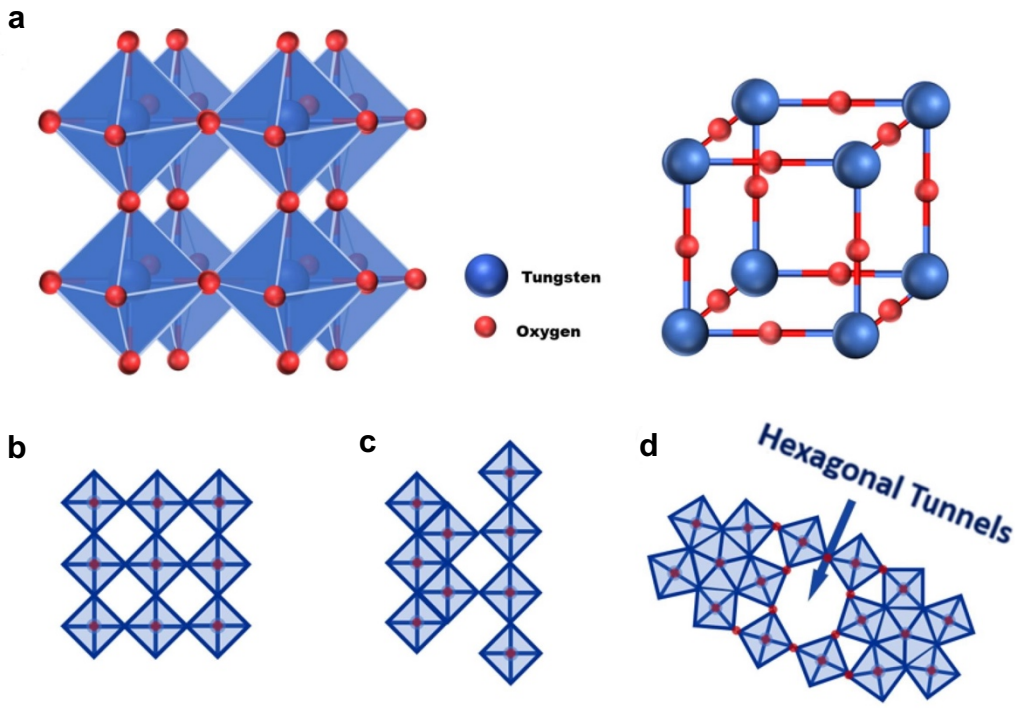

Figure 8: (a) Binary perovskite structure of WO_3 representation, (b) corner sharing mode, (c) edge sharing mode, (d) pentagonal Columns mode with a hexagonal cavity. (Reproduce with permission).[125]

Tungsten oxides, including WO_3, WO_{3-x} (oxygen-deficient tungsten oxide), and $WO_3 \cdot xH_2O$ (hydrated tungsten oxide), exhibit a perovskite-like structure (Figure 9a). Within this structure, WO_6 units form a three-dimensional network of corner- or edge-sharing octahedra (Figures 9, b-c). Each central tungsten atom is bonded to six oxygen atoms in an octahedral arrangement, with all oxygen atoms equidistant from the tungsten.,[126] WO_3 features W-O-W bond connectivity exhibiting a similar geometry to Rhenium oxide (ReO_2). Electronically, the material possesses a VB primarily composed of filled oxygen 2p orbitals, while CB originates from the vacant tungsten 5d orbitals.[127] Incorporation of charged compensating ions facilitates the reduction of W^{6+} to lower oxidation states like W^{5+} and W^{4+}. These partially reduced, non-stoichiometric tungsten ions contribute to achieving high electrical conductivity, leading to a metalized state.[126]

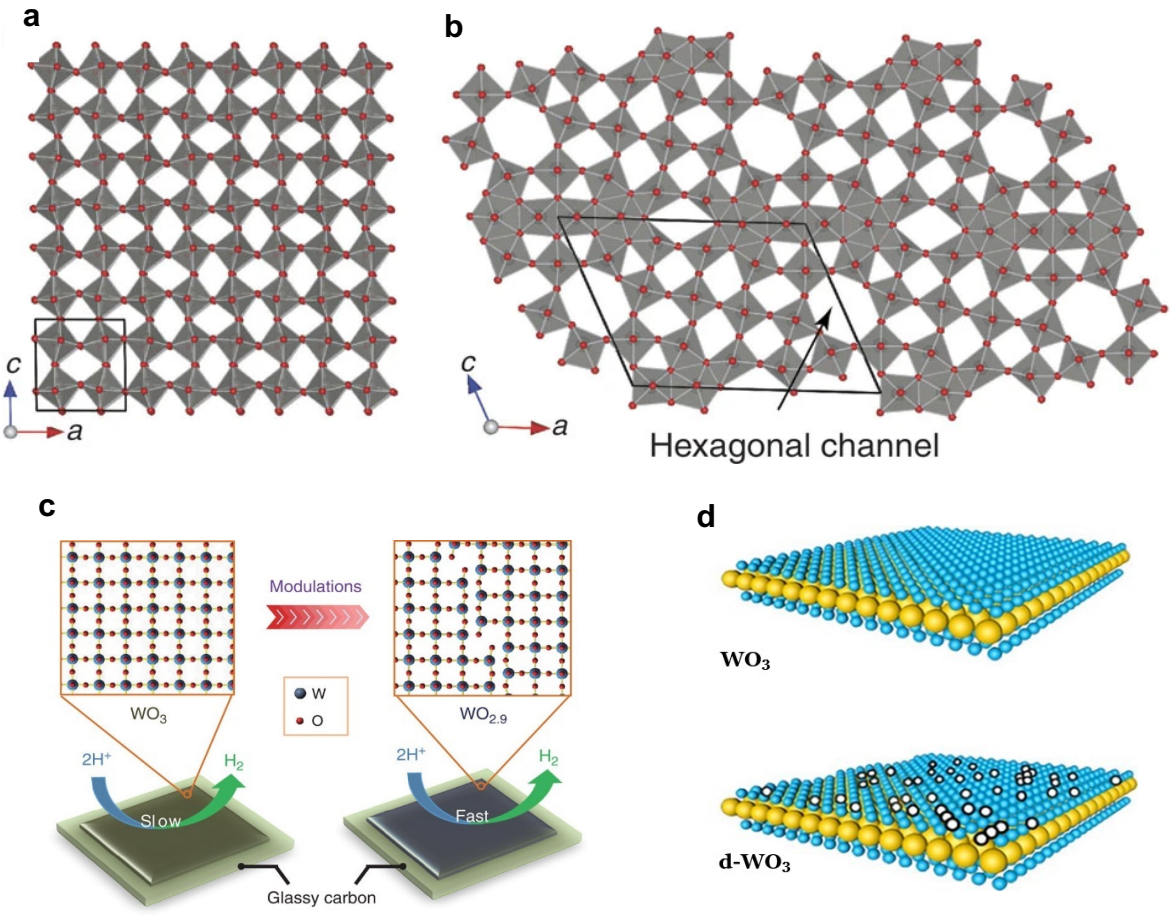

Figure 9: Structure illustration on [010] projection (a) The crystalline structure of WO_3 consists of octahedral layered of WO_6, (b) the defects in $W_{18}O_{49}$ with hexagonal channels, (c) schematic representation of WO_3 and defected $WO_{2.9}$ at reaction diagram and (d) defect rich WO_3 and pure WO_3). (Reproduce with permission).[128,129,130]

We compared the structures of pristine WO_3 and defect-rich $W_{18}O_{49}$ oriented along the [010] direction (Figure 10a). Perfect WO_3 consists of infinite slabs of corner-sharing WO_6 octahedra stacked along two dimensions (ac planes). In contrast, $W_{18}O_{49}$ possesses additional hexagonal channels within its structure (Figure 10b). These oxygen defects are believed to enhance the interaction between adsorbed molecules and the material's surface, as illustrated in Figures 10c and 10d.[128] Studies by Yu Hang Li et al. suggest that the low electrocatalytic activity of pure WO_3 for HER can be attributed to its high electrochemical adsorption energy (Figure 11b). In simpler terms, pure WO_3 binds hydrogen too strongly, hindering its efficient release. Conversely, $WO_{2.9}$ exhibits a more moderate binding energy, allowing for optimal hydrogen adsorption and desorption, leading to its superior HER performance.[130] UV reflectance spectroscopy revealed an absence of any plasmonic band in commercially available WO_3, contrasting with the desirable band observed for $W_{18}O_{49}$ (Figure 11c).

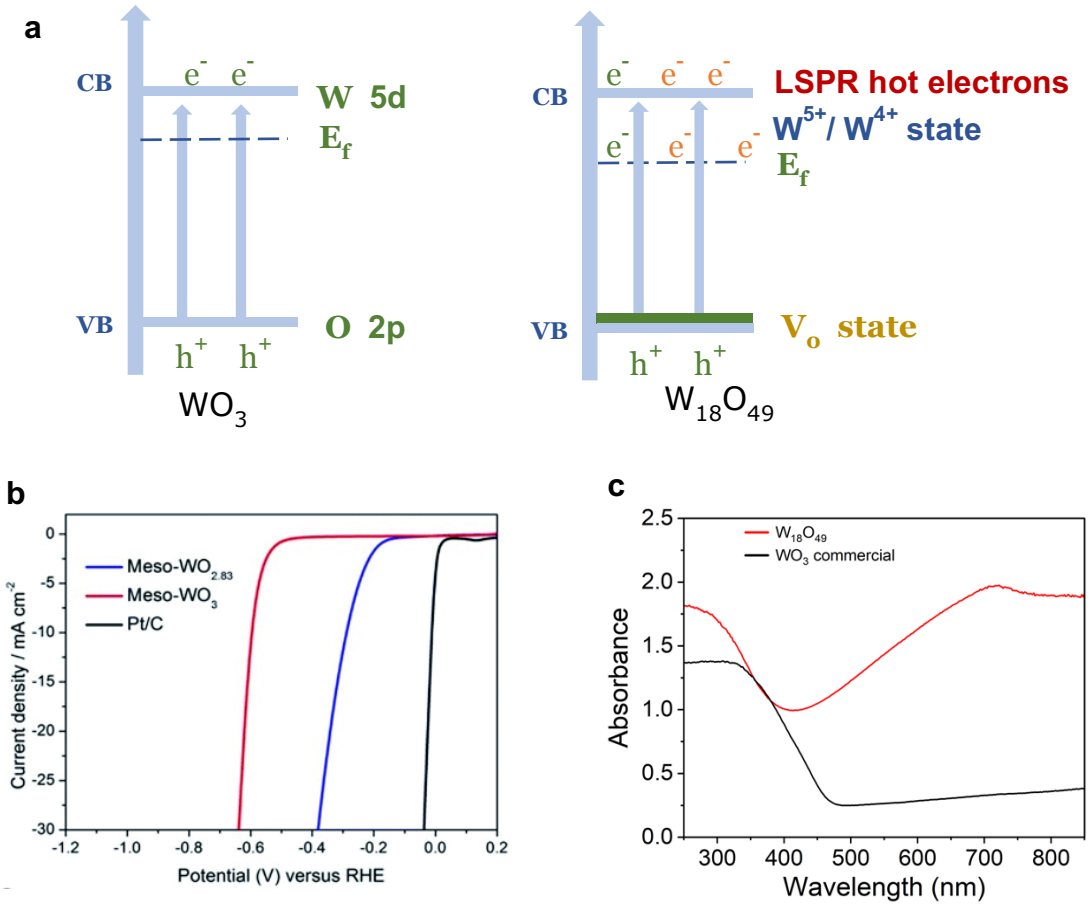

Figure 10: (a) Electronic band structure, (b) Hydrogen evolution reaction activity (polarization curve), of pure tungsten oxide and Oxygen deficient tungsten oxide, (c) UV-visible spectrum for commercial and plasmonic W-oxides. (Redraw and reproduced with permission).[131,132]

WO_{3-x} stands out as a compelling LSPR material due to its unique electronic structure. The presence of oxygen vacancies creates a discrete energy band positioned below the CB as shown in Figure 11a. This feature makes WO_{3-x} a distinct candidate for LSPR applications. However, it's important to remember that while materials with bandgap energy like the LSPR wavelength can exhibit a strong absorption peak, the intensity of the LSPR peak itself is ultimately proportional to the square root of the free electron density.[126] The material's morphology plays a critical role in its performance. A study by Cong et al. demonstrated that $W_{18}O_{49}$ exhibits an enhanced photocurrent compared to untreated WO_3. This improvement is attributed to the oxygen-deficient structure facilitating charge transport and promoting light absorption across a wider spectrum, ranging from ultraviolet to near-infrared.[124] Research suggests that substitutional doping may not be an ideal strategy for maintaining plasmonic properties in heterogeneous catalysts. The introduction of foreign atoms or ions can create recombination centers for photoexcited electrons and holes, hindering the catalyst's overall performance.

The tungsten oxide (WO_6) exhibits a fascinating property it's symmetry can be manipulated by temperature variations. Study suggest WO_6 can adopt various crystal structures, including monoclinic, hexagonal, orthorhombic, and tetragonal, depending on the temperature. This remarkable characteristic demonstrates the reversible nature of WO_6 symmetry. Zeb S. et al.[126] High-temperature annealing induces phase transitions in tungsten oxides (WO_x). Studies have shown that triclinic WO_x at room temperature transforms to monoclinic (17°C - 400°C), then orthorhombic (400°C - 740°C), and finally tetragonal at higher temperatures (>740°C). Specifically, W_3O_8 and $W_{32}O_{84}$ exhibit an orthorhombic crystal structure, while $W_{17}O_{47}$, $W_{18}O_{49}$, $W_{20}O_{58}$, and $W_{25}O_{73}$ become monoclinic, and W_5O_{14}.[126] transforms to a tetragonal structure.[126]

Among interstitial doping materials, tungsten bronzes with the general formula A_xWO_3 (where A can be H, Na, Li, K, Cs, or Rb) have recently attracted significant interest. This class of materials exhibits unique properties due to the presence of dopant atoms within the crystal structure.[115] Interstitial doping offers an alternative approach to enhance the plasmonic behavior of materials like WO_3. This technique

introduces new atoms within the crystal lattice, specifically exploiting the tunnel structure of WO_3 to readily accommodate hydrogen or alkali metals. The partial ionization of these dopant atoms contributes free carriers, ultimately leading to the generation of plasmon resonance.[117] Hydrogen, the lightest element, can be incorporated into the crystal lattice of oxides like WO_3 and MoO_3 by occupying interstitial sites. This process, while resulting in phases with structures very similar to the parent oxides, leads to fascinating property changes. Notably, the properties of these hydrogen-doped materials exhibit a strong dependence on the hydrogen content.[115] According to Cheng et al., the formation mechanism involves the H-spillover effect (Figure 12a). This process begins with the adsorption of hydrogen molecules onto the surface of metal nanoparticles. These adsorbed molecules dissociate into reactive hydrogen atoms. Subsequently, these reactive hydrogen atoms spill over and incorporate onto the semiconductor surface. Finally, the hydrogen atoms diffuse through the bulk of the semiconductor, facilitating its reduction to a bronze phase.[117] The formation of this material absent metal support typically necessitates high temperatures ranging from 400°C to 550°C. Conversely, the presence of a metal support can significantly reduce the formation temperature, even enabling room-temperature synthesis.[117]

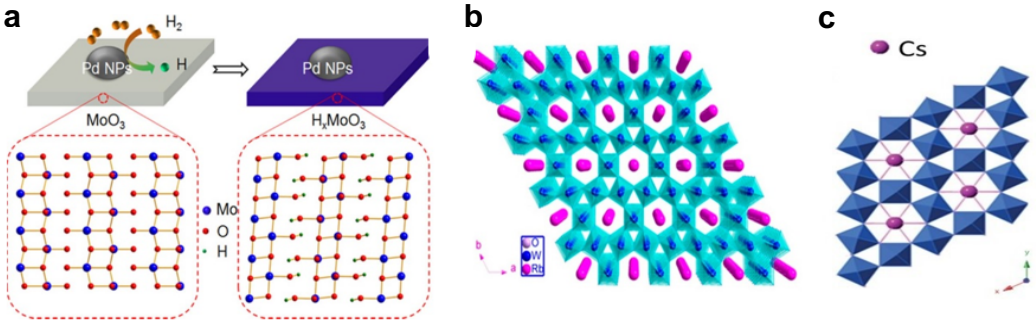

Figure 11: (a) schematic diagram for the formation of Hydrogen bronze, (b-c) $Rb_{0.33}WO_3$ and $Cs_{0.29}WO_3$. (Reproduced with permission).[117,118,133]

Doping with alkali metals and hydrogen introduces them into hexagonal tunnels (Figure 12, b-c). These dopants donate free carrier electrons, which significantly modify the material's electronic structure, leading to enhanced photocatalytic conversion reactions. This enhancement stems from three main factors, modification of the band structure, selective adsorption of gaseous molecules, and a decrease in activation energy, all of which contribute to improved catalytic activity.[118]

Cui et al. investigated a novel class of materials for photocatalytic water splitting. Specifically, they synthesized a hybrid material called WO_2-Na_xWO_3 through high-temperature reduction of the semiconductor Na_xWO_3 (where x is less than 0.25). This hybrid material exhibited promising performance in photochemical water splitting and hydrogen production.[134] This study investigates the impact of reduction temperature on the properties of a hybrid material. Notably, focused on the color changes and electrical behavior of the material as a function of temperature.

Scheme: Process to prepare hybrid WO_2 – Na_xWO_3.

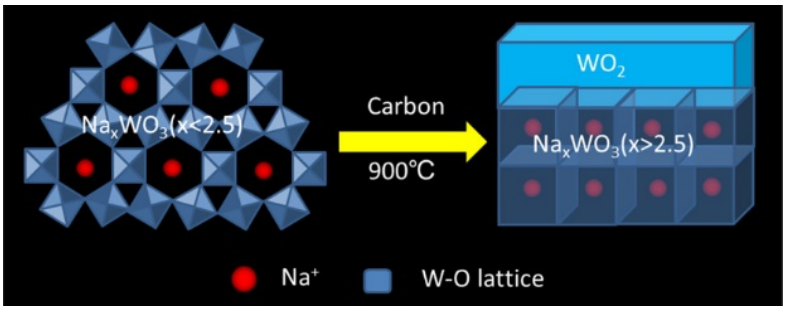

The color variation with reduction temperature (Figure 13a) reveals intriguing insights. As the reduction temperature varies, the hybrid material undergoes noticeable changes in color. The exact mechanism behind this variation remains a subject of interest. Study found that the material behaves as follows, when the Na content (denoted by "x") is less than 0.25, the hybrid acts as a semiconductor. Conversely, when x exceeds 0.25, it functions as a conductor. These findings highlight the sensitivity of the material's optical properties to the reduction process. A mechanistic overview (Figure 13b) sheds light on the underlying factors. The ladder-type energy band and barrier-free charge transport are crucial for the material's behavior. These properties arise from the electronic conductivity of WO_2, known for its favorable electronic behavior, and Na_xWO_3, which contributes significantly to the overall conductivity. The interplay between these components determines the material's performance.

Among the synthesized hybrid materials, NaHTB-C900 stands out. At a reduction temperature of 900°C, NaHTB-C900 exhibits the highest performance in terms of hydrogen evolution. Additionally, a localized surface plasmon resonance (LSPR) peak is observed in the visible spectrum, further enhancing its potential applications. (Figure 13, c-e).

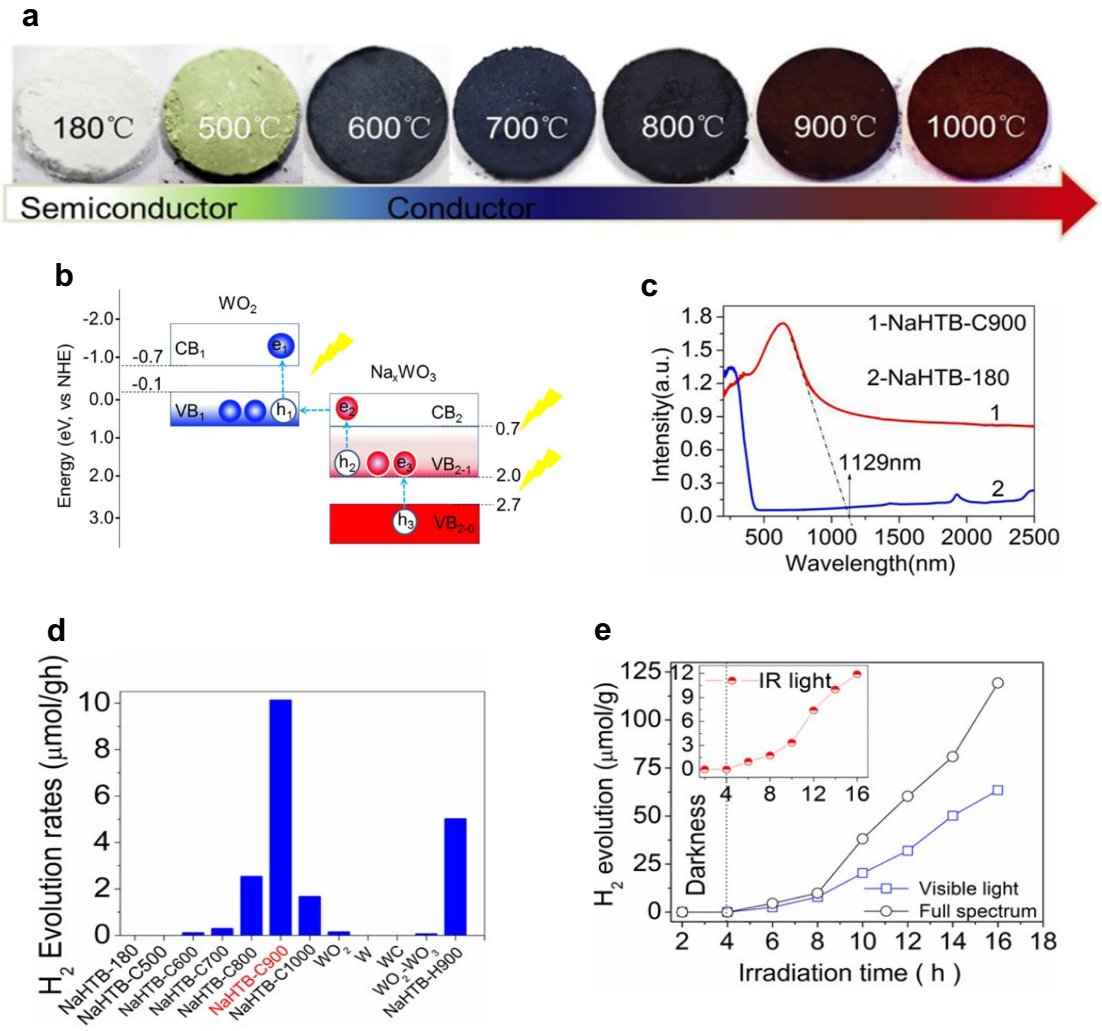

Figure 13: (a) Color change of different samples under calcination temperature, (b) Energy level diagram of hybrid WO_2 – Na_xWO_3, (c) UV-Vis diffuse reflectance spectra, (d) Photocatalytic activity of different samples, and (e) Photocatalytic activity of the best sample. (Reproduced with permission)[134]

2.3 Electrochemical water splitting

Electrochemical water splitting is a promising technology for generating clean, efficient, and sustainable green hydrogen, a potential replacement for fossil fuels. This process, also known as electrolysis, uses electricity to split water molecules (H_2O) into hydrogen (H_2) and oxygen (O_2). However, this reaction requires an energy input ($\Delta G^\circ = +237.2$ kJ mol^{-1}) and involves two half-reactions, the hydrogen evolution reaction (HER) at the cathode and the oxygen evolution reaction (OER) at the anode (Figure 14).

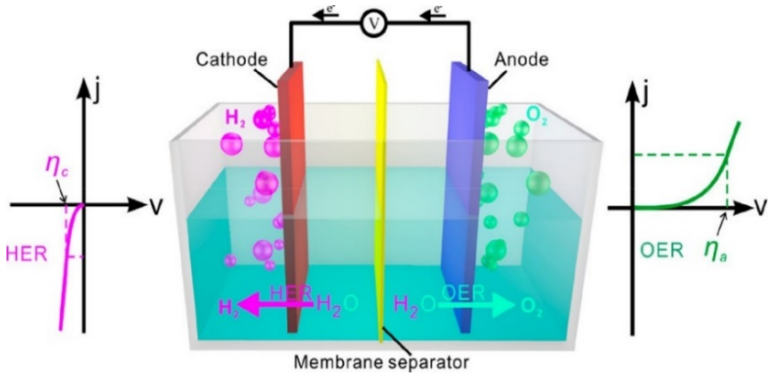

Figure 14: Electrocatalytic Hydrogen evolution reaction and Oxygen evolution reaction. (Reprinted with permission).[3]

The main challenge in water splitting lies in the sluggish reaction kinetics of both HER and OER, resulting in high overpotentials (η). Overpotential represents the additional electrical energy needed beyond the theoretical minimum to drive the reaction at a desired current density. Fortunately, catalysts can significantly reduce the overpotentials for HER and OER. The development of highly efficient and selective catalysts is crucial for the practical application of water splitting and the large-scale production of green hydrogen and oxygen.

$$H_2O\ (l) \rightarrow H_2\ (g) + 1/2\ O_2\ (g) \qquad \Delta E^\circ = 1.23\ V\ (vs\ RHE) \qquad (5)$$

Where, RHE is a reversible hydrogen electrode.

The two half-cell reactions are as follows,

HER,

$$2H^+ (aq) + 2e^- \rightarrow H_2 (g) \quad (6)$$

and OER,

$$2H_2O (l) \rightarrow 4H^+ (aq) + O_2 (g) + 4e^- \quad (7)$$

2.3.1 Hydrogen Evolution Reaction

The electrochemical hydrogen evolution reaction proceeds through a three-step mechanism: the Volmer reaction, the Heyrovsky reaction, and the Tafel step. In the first step, a hydrogen ion (H^+) from the electrolyte accepts an electron at the catalyst surface to form an adsorbed hydrogen atom (M-H*). The Heyrovsky reaction involves the interaction of another proton (H^+) with the adsorbed hydrogen, accepting another electron and desorbing it as a hydrogen molecule (H_2). Finally, the Tafel step involves the direct recombination of two adsorbed hydrogen atoms (H*) to form a hydrogen molecule (H_2) and desorb from the catalyst surface. This interplay between these steps is crucial for efficient HER. (Figure 15).

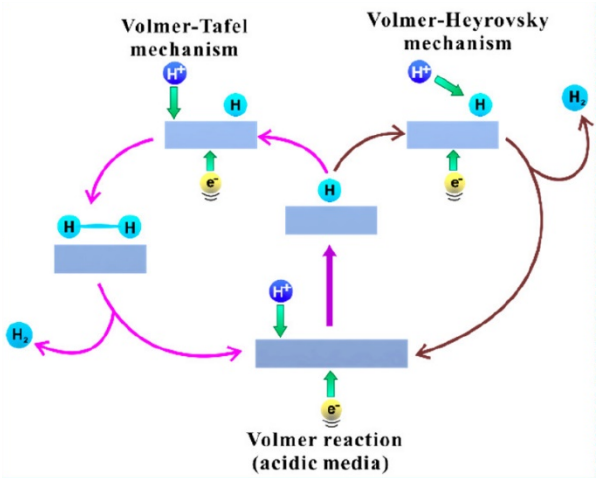

Figure 15: Mechanism of hydrogen evolution reaction (acidic electrolyte) solution on the surface of the metal. (Reproduced with permission).[3]

Mechanistic steps are as follows,

Volmer reaction,

$$H_3O^+ (aq) + M + e^- \leftrightharpoons M\text{-}H^* + H_2O (l) \quad (8)$$

Heyrovsky reaction,

$$H^+ (aq) + e^- + M\text{-}H^* \leftrightharpoons H_2 (g) + M \quad (9)$$

Or Tafel reaction

$$2\ M\text{-}H^* \leftrightharpoons H_2 (g) + 2M \quad (10)$$

According to the Sabatier principle, the interaction between the catalyst surface and the reactive species needs to be just right. If the interaction is too weak, the reactant molecules won't bind effectively to the catalyst surface, and the reaction will be slow. On the other hand, if the interaction is too strong, the product molecules will bond too strongly to the catalyst surface and block other reactant molecules from binding. This can poison the catalyst and stop the reaction from happening altogether.[135] The energy required for the adsorption (H*) and desorption of hydrogen can be evaluated by ΔG_{H^*}. In the context of ΔG_{H^*}, an ideal catalyst would have a ΔG_{H^*} value of zero, representing an ideal balance between adsorption and desorption energies, leading to the highest current density (*jo*). According to Parsons et al.[136], a plot of ΔG_{H^*} vs *jo* shows that when ΔG_{H^*} is positive ($\Delta G_{H^*} > 0$), the adsorption of H* is relatively weak. This weak adsorption requires extra energy for the Volmer step to initiate the reaction, leading to poor catalytic activity. This weak adsorption also leads to an exponential increase in *jo*. Conversely, when ΔG_{H^*} is negative ($\Delta G_{H^*} < 0$), H* adsorption is strong compared to the previous case. This strong adsorption affects the Heyrovsky or Tafel steps and leads to an exponential decrease in *jo* (Figure 16a). She et al. utilizes theoretical calculations and computational science to analyze a plot that incorporates various metals and ΔG_H values. This analysis helps to identify the most suitable metal for the process (Figure 16b). [137]

The Figure 16 suggests that Pt, Re, Pd, Ir, and Rh are promising candidates for electrocatalysts due to their optimal free energy and exchange current density values. In electrocatalysis, the ideal catalyst material should have an optimal binding energy for the reacting molecule. This balance is achieved when the free energy change (ΔG_H) for the adsorption of a molecule onto the catalyst surface is neither too positive nor too negative.

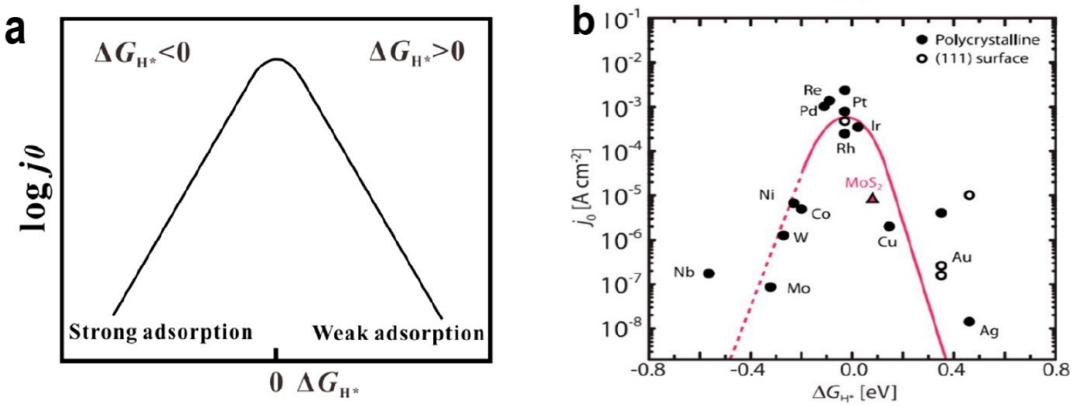

Figure 16: (a) Representation of the relationship between j_0 and ΔG_{H^*} according to Langmuir adsorption model (Reproduce with permission)[136]; (b) Volcano plot, Relationship between j_0 and ΔG_{H^*} on the surface of different Noble, Non-Noble metals, alloy compound (Reproduce with permission).[137]

2.3.2 Electrochemical parameters to evaluate HER catalyst.

The parameters used to evaluate and compare different electrocatalysts are as follows Overpotentials, Tafel slops, Electron impedance spectroscopy, Stability, and Turnover frequency.

2.3.2.1 Overpotentials

From the Nernst equation, the theoretical potential for the HER is zero under standard conditions. However, in practical applications, a greater potential, known as the applied potential, is required to overcome kinetic and thermodynamic limitations such as activation energy and energy inefficiency. The difference between this applied

potential and the theoretical Nernst potential is called the overpotential (η). Thus, the applied potential can be written as follows.

$$E = E_{HER} + \eta \quad (1)$$

The solution resistance, electrode and electrolyte contact resistance, wires, and equipment all contribute to what are known as overpotentials. These overpotentials cause a potential drop, which reduces the efficiency of the electrochemical system. This is why a greater potential is required in practical HER applications compared to the theoretical value predicted by the Nernst equation. Required correction of the following equation for HER drive again,

$$E = E_{HER} + \eta + iR \quad (2)$$

Where *iR* is the ohmic potential drop in the measurement system.

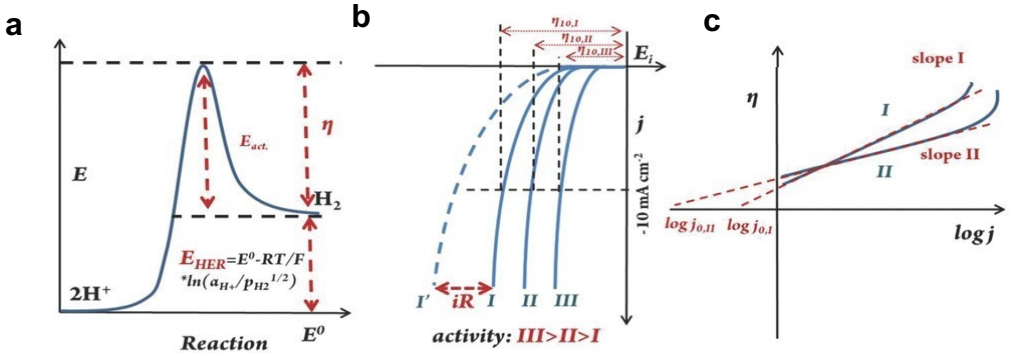

Figure 17: (a) HER energies diagram; (b) HER polarization curves with *iR* correction and indicated overpotentials; (c) Tafel plots of different electrocatalysts. (Reproduced with permission).[138]

To assess the catalytic activity of the materials, Figure 17 presents overpotentials calculated at three distinct current densities, 1 mA cm^{-2}, 10 mA cm^{-2} (η_{10}), and 100 mA cm^{-2} (η_{100}). Onset overpotential (η_1), signifying the initial current required for HER, catalysts materials are distinguished from η_{10}, which is commonly used for comparing catalyst performance. Notably, a current density of 10 mA cm^{-2} corresponds to approximately 12.0% efficiency in the solar water splitting reaction.[3,138] For an accurate comparison of catalytic activity using the η_{10} value, it's crucial to employ identical catalyst loadings and electrodes for all materials. This ensures a consistent

electrode surface area, eliminating the confounding factor of different exposed areas arising from varying loadings or electrode types. Furthermore, η_{100} serves as a valuable metric for assessing the practical applicability of catalyst materials. It reflects the overpotential required to achieve a higher current density (typically 100 mA cm^{-2}), which is more relevant for real-world applications compared to η_{10}. However, this also depend on the materials as well.

2.3.2.2 Tafel slops

Tafel slop used to get an idea about the kinetics of the reaction, by plotting η as a function of log |j|.

$$\eta = b \log |j/j_0| \quad (1)$$

where j and j_o are current density and intrinsic current density respectively, b can be obtained from the plot the smaller the value of b indicates the lower the value of η required for the reaction and faster reaction rates. A high-performance electrocatalyst should have a lower b value, smaller η, and high j and j_o. Recently Hu and coworker[139] developed a method to calculate b for the electrocatalysts that are not good electronic conductors this study uses the Electrochemical impedance spectroscopy (EIS) data to plot R_{ct} vs η (R_{ct} is the charge transfer resistance).

2.3.2.3 Electrochemical Impedance Spectroscopy

EIS is a potent technique that delves into the interfacial phenomena occurring at the electrode-electrolyte interface. It measures the system's impedance by applying a small AC potential across a spectrum of frequencies. This acquired impedance data can then be meticulously analyzed to extract valuable information regarding various processes that influence HER, including charge transfer limitations and mass transport dynamics.

In the context of HER research, EIS measurements are typically conducted within a frequency range spanning 100 kHz to 0.01 Hz. This range strategically probes the diverse time constants associated with the individual steps involved in HER. By fitting the obtained impedance spectra to established equivalent circuit models, researchers can gain critical insights into the rate of hydrogen adsorption, charge transfer resistance, and mass transport limitation. EIS analysis serves as a powerful tool for researchers to optimize HER catalysts. By identifying bottlenecks within the reaction pathway through this technique, researchers can tailor strategies to enhance the rate of hydrogen adsorption and ultimately improve the overall efficiency of the HER process.[140] By analyzing the Nyquist plot generated from EIS measurements, it possible to get crucial information about two key parameters, charge transfer resistance (R_{ct}) and ohmic resistance.

The R_s is the resistance that arises from the electrode and electrolyte interface hence HER is always measured within a narrow potential range so, R_s will not change that much in the same electrochemical measurement system (Figure 18). Rct reflects the ease of electron transfer between the electrode and reacting molecules. A lower Rct signifies faster reaction kinetics, leading to a faster reaction rate and a smaller overpotential for the reaction (like HER), translating to a more efficient catalyst. Ohmic resistance, on the other hand, encompasses the combined resistance of the electrolyte solution and the electrode-electrolyte interface. Notably, for HER measurements conducted within a limited potential range using the same setup, the solution resistance is expected to remain relatively constant. Therefore, EIS serves as a valuable tool for evaluating catalyst performance. A lower R_{ct} obtained from EIS analysis directly correlates with faster and more efficient electrocatalysis.[141]

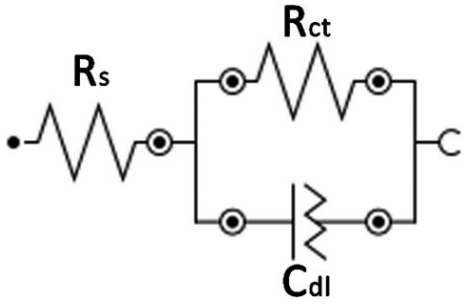

Figure 18: EIS equivalent model of Faradaic impedance of HER.[141]

2.3.2.4 Stability

The long-term performance of a HER electrocatalyst is paramount for its viability in practical applications. Therefore, a critical aspect of catalyst evaluation involves assessing its durability or stability. Two primary electrochemical measurement techniques are usually analyzed for this purpose namely voltammetry and galvanostatic/potentiostatic electrolysis. Voltammetry techniques, such as repetitive cyclic voltammetry (CV) and linear sweep voltammetry (LSV), involve cycling the catalyst's potential or sweeping it in a single direction. By comparing the initial and final current densities or overpotentials obtained during these measurements, it quantifies the extent of performance degradation over time.

In contrast, galvanostatic or potentiostatic electrolysis involves holding the catalyst at a constant current density (galvanostatic) or potential (potentiostatic) for an extended duration. This approach simulates real-world operating conditions. By monitoring the current density or potential throughout the test, it evaluates of the catalyst's ability to maintain its activity and efficiency under prolonged use. These techniques are invaluable tools for identifying HER electrocatalysts with superior durability, a key characteristic for successful implementation in practical applications.[142] Both the CV and LSV are valuable tools for assessing the stability or durability of HER catalysts.

The stability test by (CV) typically involves a large number of cycles (often exceeding 1000) within a specific potential range. This range usually encompasses the onset overpotential (the minimum potential required to initiate the reaction) and the overpotential required to achieve a specific current density (e.g., 10 mA cm^{-2}). During the test, a small change in overpotential is considered acceptable. A larger difference between the initial and final overpotentials indicates a greater degree of catalyst degradation. Therefore, catalysts with minimal change in overpotential after the stability test are considered more durable and promising for practical applications[3]. Beyond the initial assessment provided by voltammetry and electrolysis techniques, a deeper understanding of a catalyst's durability for HER can be gained through chronopotentiometry and chronoamperometry.

In chronopotentiometry, a constant current density, typically set at 10 mA/cm², is applied to the catalyst. The key measurement here is the change in potential over time. A stable catalyst will exhibit minimal change in potential under this constant current stress, indicating its ability to maintain its activity. Conversely, chronoamperometry keeps the potential constant while monitoring the current density response. A catalyst with superior durability will show a high and stable current density throughout the experiment.

The duration of these experiments is generally indicative of catalyst stability, with longer durations under constant current or potential suggesting a more robust material. However, it's important to remember that the specific measurement parameters, like the commonly used 12-hour minimum test, can be tailored depending on the catalyst itself and its intended application.[141]

2.3.2.5 Turnover frequency (TOF)

A key parameter for evaluating HER catalysts is the number of active sites per unit weight or volume. This value reflects the intrinsic activity of the catalyst. However, directly measuring these sites is challenging. In 1968, Michel Boudart[143] first introduced the evolution of a catalyst by TOF though recently its definition has been modified as the total number of molecules converted to products per catalytic site per unit time.[144]

TOF values of a catalyst are estimated by the following equation,

$$TOF = \frac{I}{xnF} \quad (1)$$

Where I represent the current (A), n is the number of moles of active sites, and x number of electron transfers during HER[145]. However, the calculation of TOF is not always precise as in the case of complex molecules it's complicated to determine the active site of the catalyst but still TOF can give sufficient information to compare the catalytic activity of various catalysts.

2.4 Final remark from the literature review

This section comprehensively reviewed the application and importance of noble metals in driving water splitting for hydrogen evolution. It subsequently explored the influence of various supporting materials on tuning the activity and morphology of catalysts. Notably, the primary focus of this work was to investigate earth-abundant plasmonic materials as catalyst supports. However, a critical gap exists in the literature regarding the utilization of plasmonic $W_{18}O_{49}$ as a support to enhance the catalytic activity of Pt, thereby enabling the development of an ultra-low loading electrocatalytic system. This research aspires to address this knowledge gap by exploring $W_{18}O_{49}$ as a support material.

3. The objective of the thesis

This work centered on exploring the potential of earth-abundant materials for developing a sustainable and HER catalysts to address green hydrogen production. We investigated the use of $W_{18}O_{49}$ based materials, known for their earth abundance and plasmonic properties, as catalyst supports. Additionally, state-of-the-art noble metal Pt was employed as a benchmark catalyst. Our overarching goal was to establish a system that significantly reduces the reliance on expensive noble metals by leveraging earth-abundant, cost-effective plasmonic materials. This approach paves the way for a more sustainable and scalable path towards renewable energy production and ultimately, a green hydrogen economy.

4. Experimental section

4.1 Materials

All the chemicals were used without further purification. Tungsten Chloride (VI) (purity ≥ 99.6%), Hexahydro Hexachloroplatinic acid salt (H_2PtCl_6. $6H_2O$, ≥ 99.9%), α-Naphthol (≥ 99.8%), 10% w/w Nafion solution (≥ 99.9%) were purchased from Sigma-Aldrich. Nitric acid (HNO_3, 37% w/w, purity ≥ 99.9%), Hydrochloric acid (HCl, 37% w/w, purity ≥ 99.9%), Iso-propyl alcohol (≥ 99.9%) was used from Fisher. Sulfuric acid (H_2SO_4, 98% w/w, purity ≥ 99.9%) from Honeywell. Absolute Ethanol for synthesis (purity ≥ 99.9%), and Ethanol for washing (96% w/v, purity ≥ 99.9%) were purchased from VWR. 20% Pt-C were from Alfa Aesar. Deionized water was used throughout the experiment.

4.2 Synthesis

In a typical procedure, 100 mg of WCl_6 was dissolved in 30 ml absolute ethanol solution under stirring which forms a yellow solution. To achieve the desired Pt loading, varying amounts of a platinum precursor, hexahydro hexachloroplatinic acid hydrate ($H_2PtCl_6{\cdot}6H_2O$), are incorporated into the solution. Three batch of solution prepared by adding 0.689 mg, 1.316 mg and 2.633 mg salt. Following the introduction of the Pt salt, 1 mL of α-naphthol is added to the reaction mixture, which is then stirred for 30 minutes to ensure adequate mixing. The resulting transparent solution is carefully transferred to a Teflon-lined stainless-steel autoclave. The sealed autoclave is then subjected to hydrothermal treatment at 180 °C for a reaction time of 24 hours. After the reaction is complete, the autoclave is allowed to cool naturally to room temperature. The resulting suspension is then centrifuged at 7,000 rpm for four cycles to isolate the Pt-doped tungsten oxide nanoparticles. The collected nanoparticles are subsequently washed thoroughly with absolute ethanol to remove any residual reaction byproducts or impurities. Finally, the purified nanoparticles are dried in an oven at 60 °C.

4.3 Characterization

4.3.1 Atomic Emission Spectroscopy

Microware Plasma-Atomic Emission Spectroscopy (MP-AES) is an analytical technique used to identify and quantify the inorganic elements in a sample. It works by analyzing the light emitted by the sample when it's introduced to a high-temperature, nitrogen-filled microwave plasma. This plasma reaches temperatures around 5,000 Kelvin, which excites the atoms in the sample, causing them to emit light at specific wavelengths. An instrument called a magnetron efficiently creates this nitrogen plasma from compressed air, making MP-AES a convenient and cost-effective technique. By measuring these characteristic wavelengths of emitted light, the MP-AES instrument can determine the elemental composition of the sample.[146].

The analysis began by introducing the sample as an aerosol via a nebulizer, placing it in the center of a hot plasma chamber. There, the sample rapidly dried and atomized, causing the elements within to emit characteristic light. This emitted light was then directed to a monochromator, which functioned like a prism, separating the unique light signature of each element from the others. Finally, a detector simultaneously measured both the desired elemental spectra and any background interference. To quantify the elements present, a calibration curve was established using a sample of known concentration. By comparing the measured emissions with this reference, the elemental composition of the original sample was determined.[147].

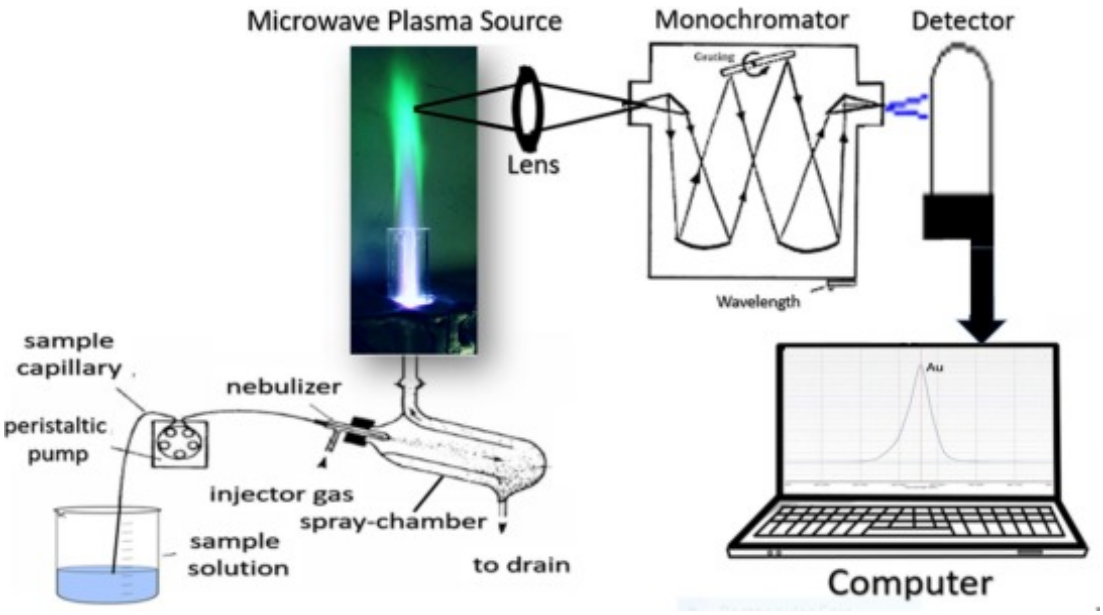

Figure 19: Schematic diagram of MP-AES (Reprinted with permission).[148]

The experiment began with 1 mg of the sample being dissolved in 4.0 ml of aqua regia. This mixture was then slowly evaporated at 75°C. After evaporation, 10.0 ml of 0.5 M HCl was added, and the solution was transferred using a syringe. This resulting solution is the stock solution with a concentration of 100 ppm. From this stock solution, dilutions were prepared to create 5 ppm and 25 ppm solutions for further elemental analysis. Finally, to establish a calibration curve, different standard solutions were prepared.

Table 2:Concentration of the reference sample for the calibration curve.

Sample	C/ ppm
Standard sample 1	1
Standard sample 2	2
Standard sample 3	3
Standard sample 4	5
Standard sample 5	7
Standard sample 6	10
Standard sample 7	25

4.3.2 UV-Vis spectrometry and Diffuse reflectance spectrometry

In the realm of material characterization, UV-spectrometry reigns as a ubiquitous and highly versatile technique for elucidating the optical properties of molecules and materials. This analytical workhorse functions by meticulously dissecting light-matter interactions, quantifying the extent to which light is absorbed, transmitted, or reflected by the sample under investigation. The core principle involves directing ultraviolet or visible light towards the sample and contrasting it with a reference, often a cuvette containing solely the solvent. Through a sophisticated splitting of the light beam, the instrument precisely measures the light absorbed uniquely by the sample (Figure 20). This information, meticulously graphed as a function of photon energy, unveils a treasure trove of knowledge regarding the electronic and atomic structures of the material. It is paramount to recognize that external factors such as temperature, mechanical stress, and even the sample's morphology can significantly influence light absorption, necessitating a nuanced approach to data interpretation. Commercially available UV-spectrometers boast an impressive spectral range, typically encompassing the near-ultraviolet region (around 200 nanometers) to the near-infrared region (around 3 micrometers).[149]

Diffuse Reflectance Spectroscopy (DRS) is a valuable technique for characterizing powder samples, particularly those that are nanostructured, opaque, and have rough surfaces. This method works by utilizing specially designed mirrors to capture the reflected light from such samples (Figure 21). The resulting reflectance spectrum is then compared to a standard known diffuse reflectance, allowing researchers to analyze the material's optical properties and composition.

When solid particles, like nanoparticles suspended in a liquid, interact with light, two main phenomena occur absorption and scattering in various directions. The combined effect, known as extinction, determines how much light is ultimately lost. Interestingly, for particles much smaller than the wavelength of light, absorption dominates scattering. This characteristic makes extinction spectra a valuable tool for identifying small nanoparticles with plasmonic properties. Specifically, if a plasmonic

peak falls within the measured wavelength range (around 171 nm in this case), it can be a strong indicator of the presence of such nanoparticles.[150–153].

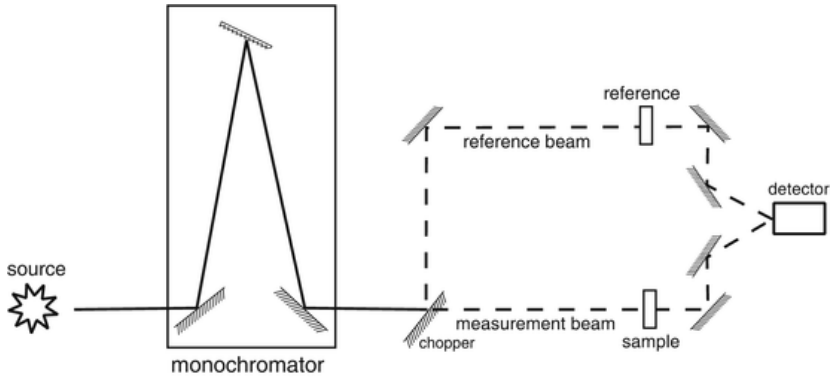

Figure 20: Schematic representation of dual beam spectrophotometer operating in transmittance mode. (Reproduced with permission).[149]

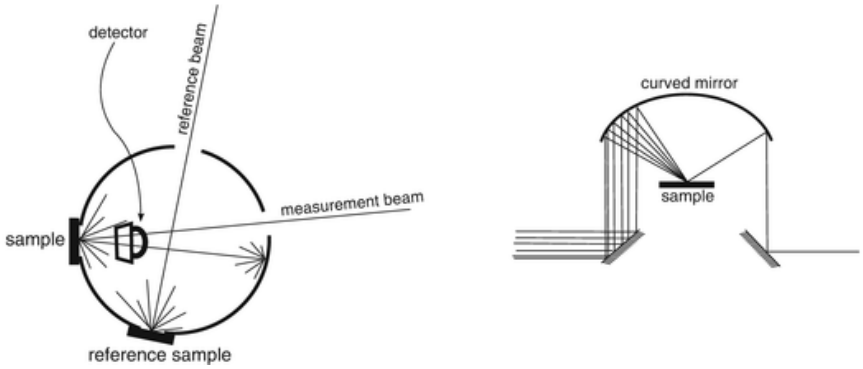

Figure 21: Schematic diagram for DRS based on integrating sphere (left) and collecting mirror (right). (Reproduce with permission).[149]

UV characterization was performed using a Shimadzu UV-2600 spectrophotometer scanning across a wavelength range of 200-800 nm. Diffuse reflectance spectroscopy (DRS) measurements were obtained on the same instrument equipped with an integrating sphere attachment (ISR-2600). Samples were prepared by pressing the powdered material into the sample holder and referenced against a standard barium sulfate ($BaSO_4$) sample.

4.3.3 Electron Microscopy

Electron microscopy stands as a powerful tool for material characterization, surpassing the capabilities of traditional light microscopy. By employing a beam of accelerated electrons instead of visible light, EM achieves significantly higher resolution and magnification, enabling the visualization of a specimen's structure and composition at the atomic or molecular level. This technique offers various operational modes, including transmission, scanning, and even a combined scanning transmission mode. Each mode tailors the interaction between the electron beam and the sample, providing researchers with a versatile platform to unveil the intricate details of a broad spectrum of materials.

Electron microscopy extends beyond high-resolution imaging, offering a potent suite of analytical techniques. These include electron diffraction, energy-dispersive X-ray spectroscopy, and electron energy-loss spectroscopy, allowing for comprehensive characterization of a sample's crystallographic structure, elemental composition, and chemical bonding. However, electron microscopy necessitates a meticulously controlled environment. To mitigate electron scattering, absorption, and radiation damage, the microscope chamber requires a high vacuum, and samples themselves must be exceptionally thin for optimal beam penetration. Despite these specialized requirements, electron microscopy remains an indispensable tool across diverse scientific and engineering disciplines. From the realms of physics and chemistry to biology, materials science, nanotechnology, and medicine, electron microscopes empower researchers to delve into the microscopic world, unlocking a deeper understanding of matter at its most fundamental level [154].

4.3.3.1 Scanning Electron Microscopy

The Scanning Electron Microscope (SEM) presents a highly sophisticated analytical technique, employing a focused beam of electrons to meticulously scan and magnify a specimen's surface. This method surpasses the capabilities of conventional light-based microscopes. The SEM harnesses the fundamental principles of electron-matter interactions. As the electron beam interacts with the specimen, it generates signals that unveil critical information about the morphology, elemental composition, and crystallographic structure of the sample.

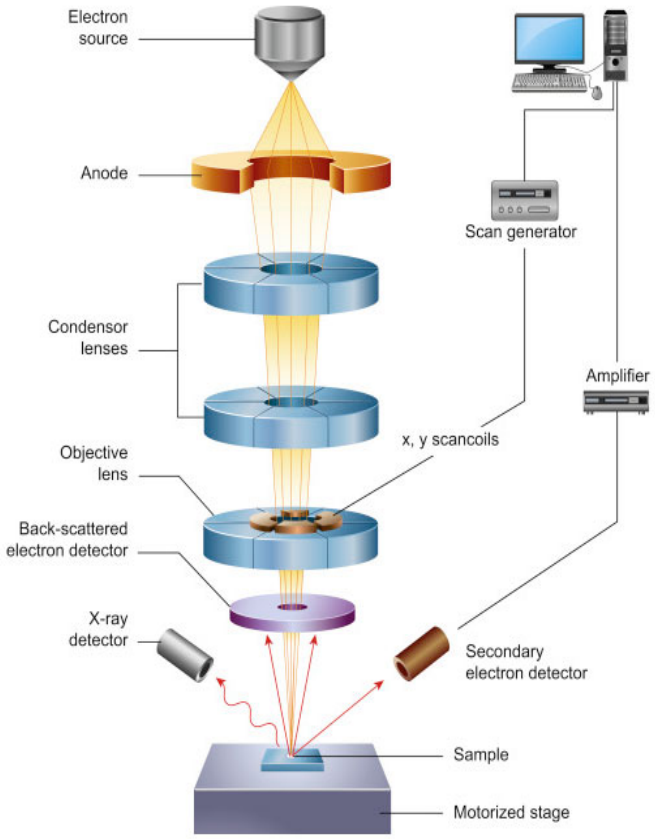

Figure 22: Schematic of a scanning electron microscope (Reproduced with permission from nanoscience.com)[157]

The core components of the SEM include the electron gun, electron column, specimen stage, and detection system. The electron gun meticulously generates a beam of electrons, which is subsequently accelerated and focused by a series of electromagnetic lenses within the column. This precisely controlled beam is then raster-scanned across

a designated area of the specimen, which is meticulously positioned on the stage. The interaction between the beam and the specimen produces various signals, including secondary and backscattered electrons alongside characteristic X-rays. These signals are meticulously collected by specialized detectors and subsequently transformed into a high-resolution image or an informative spectrum (Figure 22). By delivering exceptional spatial resolution and a substantial depth of field, SEM has become an indispensable instrument for researchers across diverse scientific disciplines. It empowers them to investigate the intricate surface characteristics and elemental composition of a wide range of materials. [155]

In SEM, a precisely focused beam of electrons scans across the surface of a specimen, inducing interactions with the sample's atoms. These interactions produce a variety of signals, including secondary and backscattered electrons, characteristic X-rays, and even cathodoluminescence. The type and intensity of these signals are influenced by several parameters, the accelerating voltage of the primary electrons, the material's density and elemental composition, and the depth of electron beam penetration. Dedicated detectors collect these signals, which hold crucial information about the specimen's topography, morphology, and elemental composition. Finally, the resolution and contrast of the resulting SEM images are dictated by the nature of the sample-electron interaction and the size of the interaction volume.[156]

4.3.3.2 Transmission Electron Microscopy

Transmission electron microscopy (TEM) constitutes a cornerstone technique within materials science and biological research. By employing a beam of high-energy electrons instead of visible light, TEM transcends the resolution constraints inherent to optical microscopy. The significantly shorter wavelength of electrons, achieved through acceleration within a strong electromagnetic field, permits TEM to achieve magnifications of up to 50 million times. This remarkable capability grants researchers the ability to visualize structures at the atomic level, unveiling a world of intricate detail that remains unseen with traditional methods.[158]

TEM offers unparalleled investigative power in materials science, particularly for deciphering structures at the nanoscale. Central to this technique is the electron source, often referred to as the electron gun. This critical component meticulously generates a high-energy electron beam and focuses it with exceptional precision using electromagnetic lenses and apertures. The electron source significantly influences the quality of the resulting TEM data by controlling the beam's brightness, coherence, and energy spread. These parameters demonstrably affect the resolution and contrast of the final images and spectra. Notably, two primary types of electron sources exist, thermionic and field emission, each with distinct advantages and disadvantages. Careful selection of the appropriate source is paramount for achieving optimal performance tailored to the specific analysis at hand.[159]

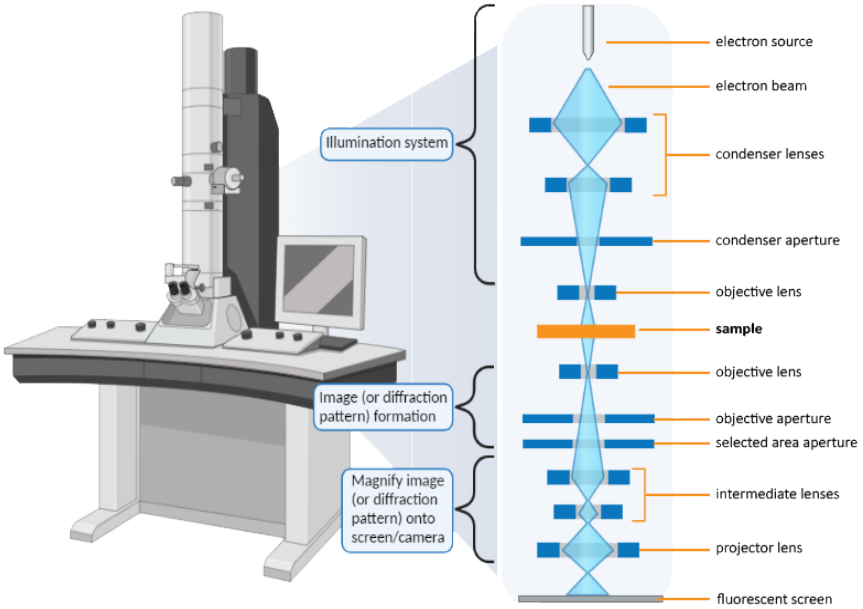

Figure 23: Simplified TEM diagram highlighting the major components throughout the column (Reproduced with permission from nanoscience.com)[157]

Following synthesis, the samples were examined using both the EM. A Hitachi S-4800 Field Emission SEM was employed for high-resolution imaging of the sample surface morphology. For TEM analysis, a JEOL JEM-2100 Plus model was utilized. To prepare the samples for SEM imaging, a drop-casting technique was used. This involved dispersing a minute amount of the sample suspension in ethanol onto a silicon (Si) substrate. The substrate was then secured onto a sample holder using carbon tape and left to dry for 3 hours to ensure complete solvent evaporation.

Consistent with the SEM sample preparation, TEM specimens underwent a meticulous deposition process. Sample was suspended in ethanol and carefully placed onto a carbon-coated copper grid. To ensure optimal electron transparency for high-resolution imaging, these samples were then left to dry under controlled conditions overnight. This standardized approach guaranteed the samples suitability for detailed analysis under both TEM and SEM.

4.3.4 X-Ray diffraction

X-ray diffraction (XRD) offers a powerful and non-destructive method for characterizing crystalline materials. It utilizes a monochromatic X-ray beam directed at the sample, where it interacts with the regularly arranged atoms within the crystal lattice. This interaction induces the X-rays to scatter at specific angles. Constructive interference of the scattered X-rays generates a characteristic diffraction pattern, with peak intensities reflecting the material's atomic distribution within the lattice. This unique fingerprint serves as a vital tool for scientists to elucidate the crystal structure and composition of crystalline materials.[160]

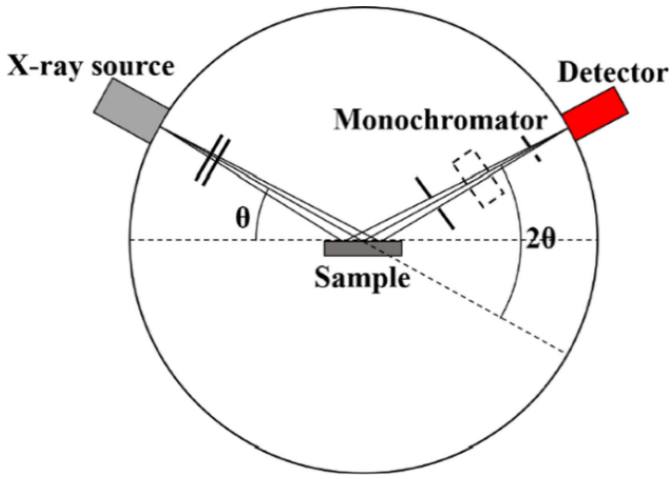

Figure 24: Schematic diagram of XRD (Reproduced with permission).[161]

XRD offers a sophisticated non-destructive method for characterizing crystalline materials. It leverages the principle of constructive interference to glean information about a crystal's atomic arrangement. Monochromatic X-rays, generated by a cathode ray tube and subsequently filtered, impinge upon the sample (Figure 24).

The interaction between these X-rays and the regularly spaced atomic planes within the crystal can result in constructive interference under specific conditions dictated by Bragg's Law ($n\lambda = 2d\sin\theta$). This phenomenon produces a diffracted X-ray beam, which serves as a fingerprint of the crystal's internal structure.

4.3.5 Electrochemical Measurement

A three-electrode cell interfaced with a Metrohm Autolab potentiostat was employed to assess the electrocatalytic activity of the catalyst. The working electrode (WE) consisted of a 6 mm diameter, 0.1257 cm^2 area L-shaped glassy carbon electrode coated with the catalyst. Prior to catalyst deposition, the WE surface was meticulously polished and ultrasonicated. The catalyst ink, containing the catalyst itself and Nafion solution (7:2.9:0.1 ml EtOH:H_2O:Nafion) as a binder (pre-ultrasonicated for 20 minutes), was loaded onto the WE at a density of 400 $\mu g\ cm^{-2}$. A homogenous catalyst film was achieved through subsequent drying in oven. A graphite rod and reversible hydrogen electrode served as the counter electrode (CE) and reference electrode (RE), respectively. To eliminate dissolved gases, the 0.5 M H_2SO_4 electrolyte solution was purged with Ar gas for 20 minutes before all electrochemical measurements. Linear sweep voltammetry (LSV) was employed to obtain HER polarization curves and the catalyst was subjected to a 24-hour chronopotentiometry test to evaluate its stability. Finally, electrochemical impedance spectroscopy (EIS) was performed in potentiostatic mode at -0.035 V with an amplitude of 0.005 V and a frequency range spanning 100 kHz to 10 Hz.[142]

4.4 Result

4.4.1 Atomic Emission Spectroscopy

In this study, microwave plasma-atomic emission spectroscopy (MP-AES) was employed to quantify the atomic percentages of platinum deposited on as synthesized samples. This precise analytical technique enabled the determination of the exact amount of platinum atoms present on the tungsten oxide surface. The demonstrated ultra-low platinum loading on the $W_{18}O_{49}$ material signifies its potential for cost-effective applications within the burgeoning carbon-free and hydrogen economies.

Table 2: Amount of added Pt-salt (mg) and elemental Pt (% wt.) incorporated on surface of $W_{18}O_{49}$.

No of Batch	Salt added (mg)	Elemental Pt (% wt.)	Sample
Batch 1	0.659	0.412	$Pt_{0.4}/W_{18}O_{49}$
Batch 2	1.317	0.832	$Pt_{0.8}/W_{18}O_{49}$
Batch 3	2.633	1.623	$Pt_{1.6}/W_{18}O_{49}$

Samples are named based on the percentages of elemental Pt on the substrate.

4.4.2 Structural characterization SEM and TEM of Pt-$W_{18}O_{49}$.

Scanning electron microscopy (SEM) analysis (Figure 25) revealed distinct morphologies for as-prepared $W_{18}O_{49}$ and Pt-$W_{18}O_{49}$. $W_{18}O_{49}$ exhibited a network of interconnected nanospheres (Figure 25a). In contrast, Pt-$W_{18}O_{49}$ displayed a more uniform particle diameter with a surface densely decorated by numerous nanorods (Figure 25b).

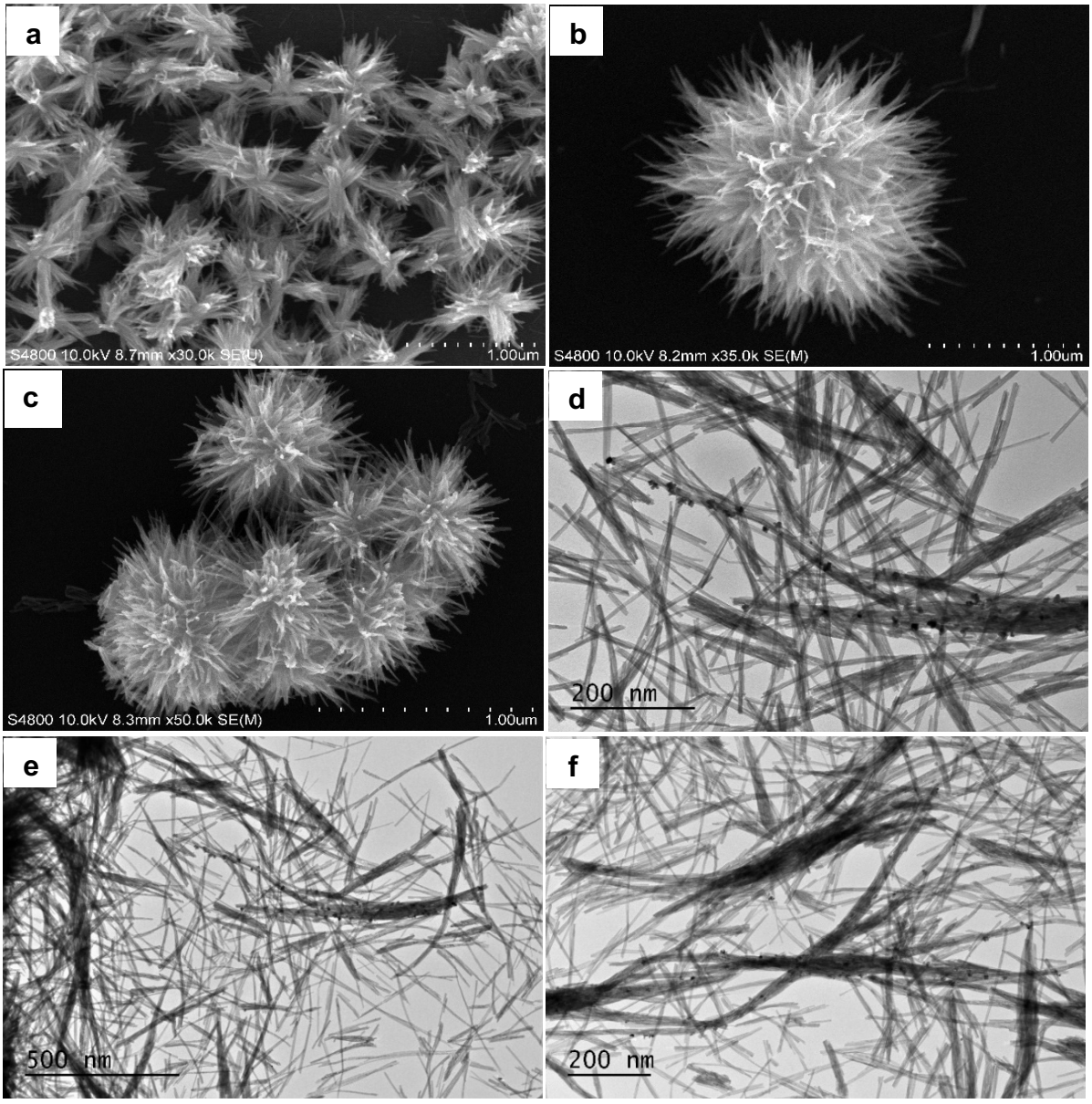

Figure 25: (a) SEM image of $W_{18}O_{49}$; (b-c) Pt-$W_{18}O_{49}$; (d-f) TEM image of Pt-$W_{18}O_{49}$

Notably, variations in Pt (% wt.) loading resulted in minimal observable differences in the SEM images. Transmission electron microscopy (TEM) analysis of fractured Pt-$W_{18}O_{49}$ (Figure 25d-f) corroborated the SEM observations, further confirming the

successful deposition of Pt atoms onto the $W_{18}O_{49}$ nanorods. Consistent with the SEM data, TEM images also showed minimal influence of Pt loading on the overall microstructure.

4.4.3 UV-Vis/DRS

Figure 26 depicts the UV-Vis Diffuse Reflectance Spectroscopy (DRS) spectrum of the analyzed sample. A pronounced absorption peak is observed at roughly 710 nm, corresponding to the LSPR peak characteristic of $W_{18}O_{49}$ nanoparticles. Interestingly, the extended tail of this peak towards the infrared region in the DRS spectrum suggests the presence of oxygen vacancies within the $W_{18}O_{49}$ crystal lattice. These oxygen vacancies can have a significant impact on the material's optical properties.[162]

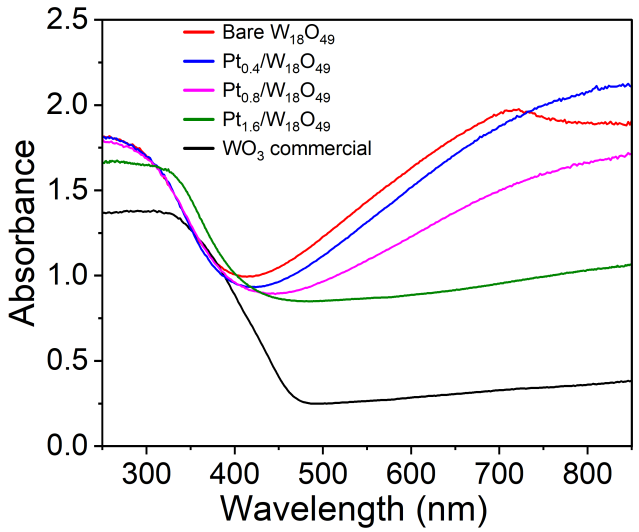

Figure 26: DRS spectra of pristine $W_{18}O_{49}$, commercial WO_3, and Pt supported $W_{18}O_{49}$.

Commercially available WO_3 lacks any absorption peak, suggesting an absence of oxygen vacancies. In contrast, Pt supported $W_{18}O_{49}$ exhibits an LSPR peak, confirming the presence of oxygen vacancies (Figure 26). However, the peak intensity weakens with increasing metal concentration. This decreases likely occurs because non-plasmonic metal particles cover the plasmonic surface of $W_{18}O_{49}$. Importantly, the consistent weakening of the plasmonic band absorption with increasing metal concentration signifies the successful and uniform deposition of metal onto the $W_{18}O_{49}$ support.

The analysis of metal-supported samples reveals an absorption tail in the spectra, suggesting a potential modification of the crystal structure during hydrothermal treatment. Additionally, the presence of a new peak indicates the possible formation of a new defect level. These observations are consistent with the observed color change of the material, transitioning from deep blue $Pt_{0.4}/W_{18}O_{49}$ to dark blue $Pt_{1.6}/W_{18}O_{49}$ (from 0.4% to 1.6% wt. Pt) upon Pt incorporation into the $W_{18}O_{49}$ structure. Furthermore, the remarkable stability of the samples is evidenced by the absence of any noticeable color change over several months.

4.4.4 X-ray diffraction (XRD)

Crystallographic analysis was performed using a PANalytical X'pert Pro MPD (materials powder diffractometer) equipped with Cu $K_{\alpha 1}$ radiation. The samples were mounted in a standard zero-background holder and scanned across a 2θ range of 20° to 60° with an optimized step size to maximize resolution. The collected data underwent shift correction and subsequent fitting using LeBail and FullProf software. Phase identification was achieved by referencing the International Centre for Diffraction Data (ICDD) database.

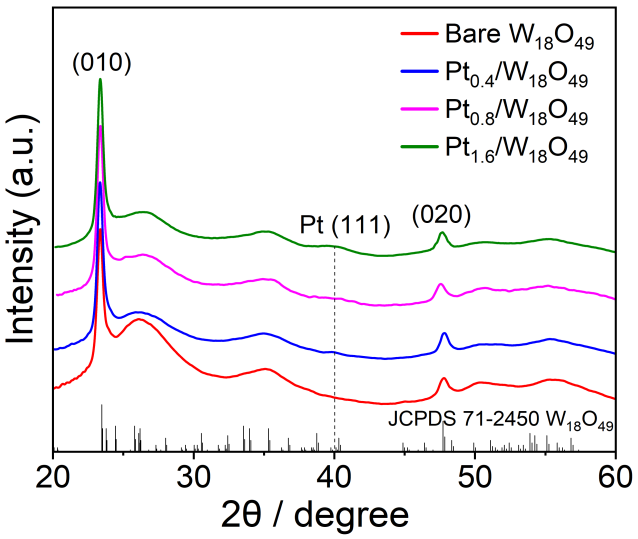

Figure 27: X-ray diffractogram for bare $W_{18}O_{49}$ and Pt-supported $W_{18}O_{49}$.

X-ray diffraction (XRD) analysis (Figure 27) revealed the crystalline structure of both Pt-supported and bare $W_{18}O_{49}$ nanostructures. The pristine $W_{18}O_{49}$ exhibited a well-

defined monoclinic crystal structure with lattice constants of a = 18.28 Å, b = 3.775 Å, c = 13.98 Å, and β = 115◦14 (JCPDS 71-2450). The XRD pattern displayed two prominent narrow peaks at 2θ = 23.3◦ and 47.7◦, corresponding to the [010] and [020] reflections, respectively. The broader nature of the remaining peaks suggested a preferential orientation of the $W_{18}O_{49}$ nanowires along the [010] direction. Notably, the incorporation of Pt did not introduce any new diffraction peaks, indicating homogeneous integration of Pt atoms within the $W_{18}O_{49}$ lattice. However, a slight shift (~0.2◦) in the peak positions of $Pt_{1.6}/W_{18}O_{49}$ compared to pristine $W_{18}O_{49}$ suggested subtle structural modifications upon Pt incorporation.

4.4.5 Raman spectroscopy

Raman spectroscopy non-destructive tool use to investigate crystal symmetry. However, temperature fluctuations can introduce inaccuracies in the resulting data. To mitigate this risk, meticulous attention was paid during the analysis of $W_{18}O_{49}$, a material particularly prone to oxidation. A low-power (sub-2 mW) laser operating at a wavelength of 633 nm was deliberately selected. This strategic choice minimized the potential for laser-induced oxidation, ensuring the integrity of the $W_{18}O_{49}$ sample and the validity of the acquired Raman spectrum.

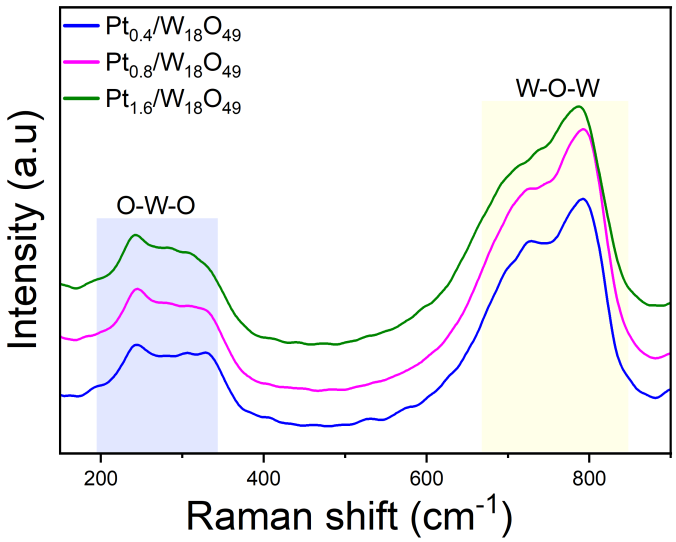

Figure 28: Representative Raman spectra for Pt- $W_{18}O_{49}$.

Figure 28 shows two distinct peaks for Pt-$W_{18}O_{49}$. These peaks correspond to the vibrational modes of the material. Interestingly, the peak positions do not vary

significantly with different Pt concentrations, likely due to the low concentration variations. The peak in the range of 267 cm-1 to 327 cm-1 is assigned to O-W-O bending modes, while the peaks at higher wavenumbers (714 cm-1 and 803 cm-1) correspond to W-O stretching modes.[163]

4.4.6 X-ray photoemission spectroscopy (XPS)

X-ray photoelectron spectroscopy (XPS) was employed to characterize the surface chemistry of pristine $W_{18}O_{49}$ and Pt-supported $W_{18}O_{49}$, as presented in Figure 29. The XPS binding energies were calibrated using a C 1s peak referenced to 284.8 eV. The presence of W, O, and Pt on the material surface was confirmed through the survey scan in Figure 29a. Deconvolution of the W 4f peaks revealed the coexistence of W^{6+} (stoichiometric) and W^{5+} (off-stoichiometric) oxidation states. The W $4f_{7/2}$ peaks for W^{6+} and W^{5+} were identified at 35.89 eV and 34.60 eV, respectively. Interestingly, Pt incorporation resulted in a slight positive shift (0.14 eV) in the binding energies of the W 4f peaks for Pt-supported $W_{18}O_{49}$ compared to the pristine material. Figure 29c depicts the deconvoluted Pt 4f spectrum, with peaks at 74.55 eV (Pt $4f_{7/2}$) and 71.55 eV (Pt $4f_{5/2}$), consistent with metallic platinum. Analysis of the O 1s peak revealed two components: one at 530.57 eV corresponding to W-O bonds and another at 531.20 eV attributed to oxygen vacancies (OVs). Notably, Pt incorporation induced subtle shifts in the binding energies of both W-O bonds (0.05 eV) and OVs (0.11 eV), suggesting a perturbation of the electronic structure of $W_{18}O_{49}$.

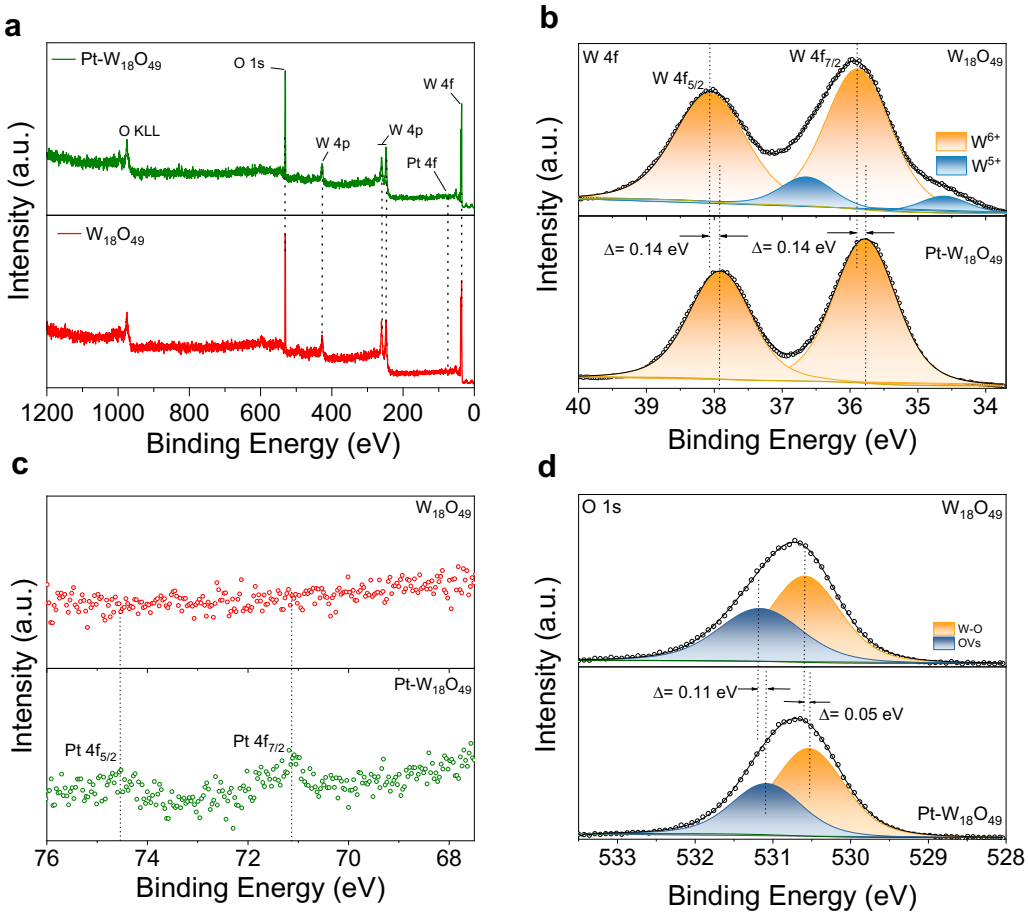

Figure 29: X-ray photoemission spectroscopy (XPS) spectra of $W_{18}O_{49}$ and Pt- $W_{18}O_{49}$ (a) Survey spectrum; (b) high-resolution spectra for W 4f; (c) Pt 4f and (d) O 1s.

4.4.7 Electrochemical measurement

The electrocatalytic activity of the synthesized materials for the hydrogen evolution reaction (HER) was assessed using linear sweep voltammetry (LSV) in 0.5 M H_2SO_4 electrolyte at a scan rate of 5 mV s-1. The HER performance of Pt-$W_{18}O_{49}$ was compared to a commercial 20% (wt.) Pt/C catalyst under identical conditions. The synthesized materials exhibited comparable onset overpotentials to the benchmark, with the best sample displaying a slight increase of only 18 mV for overpotential at current density -10 mA cm^{-2}. The favorable HER kinetics, as evidenced by the low Tafel slope and overpotential values, indicating a lower resistance for initiating the reaction. The minimal variation in overpotential observed among other synthesized materials

can be attributed to their similar Pt content (within a narrow atomic percentage range).

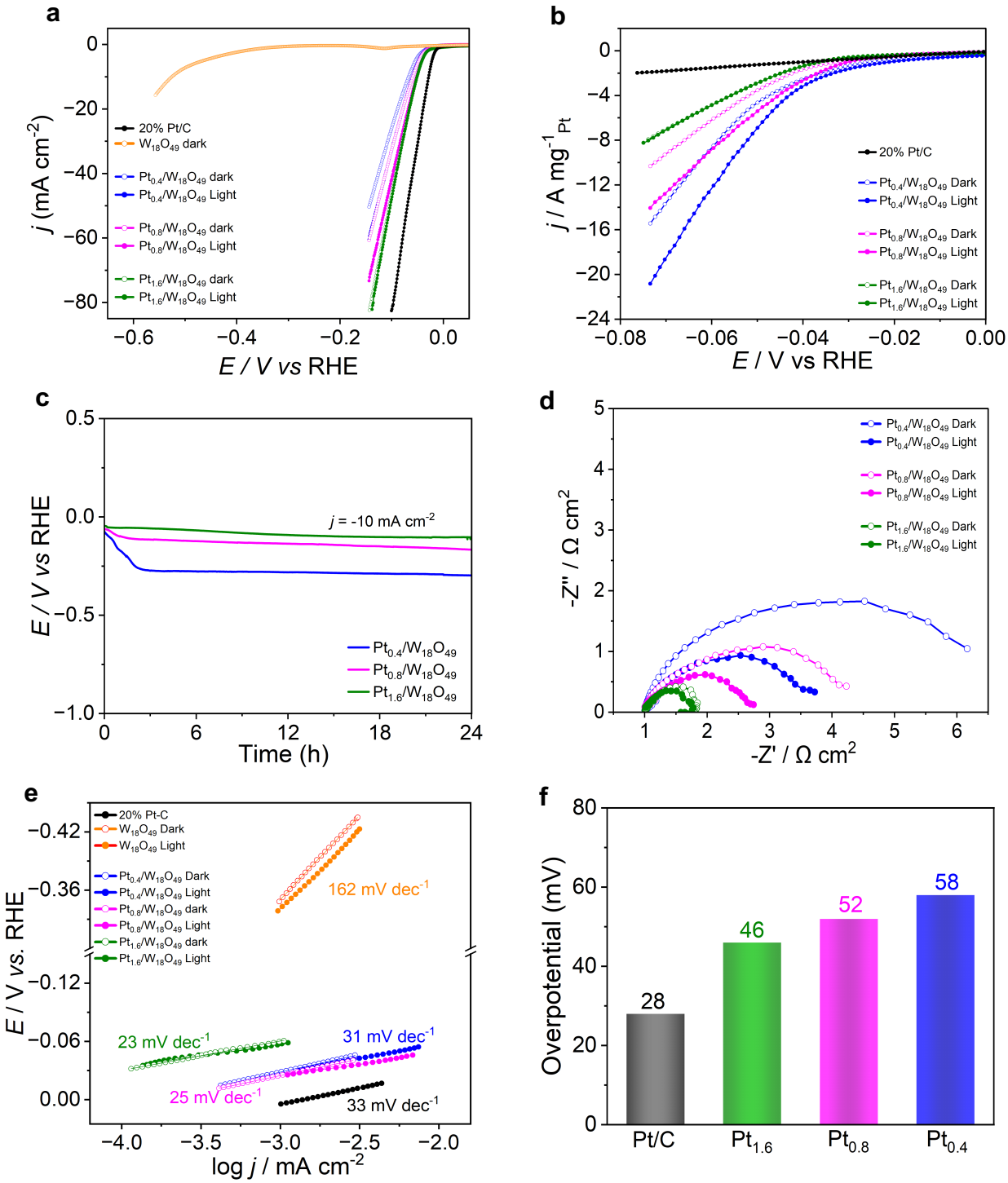

Figure 30: Electrochemical study for different samples (a-b) LSV by area and by mass of Pt; (c) chronopotentiometry at -10 mA cm-2 current density; (d) Nyquist plot for the measure EIS of Pt- $W_{18}O_{49}$; (e) Tafel plots and (f) Overpotential bar diagram obtained at current density -10 mA cm^{-2} and. All the polarization curves were measured in 0.5M H_2SO_4 with a catalyst loading of 400 µg cm^{-2} at a scan rate of 5 mV/s.

LSV reveled $Pt_{1.6}/W_{18}O_{49}$ (1.6% wt. of Pt) as the catalyst with the highest activity amongst the synthesized materials, demonstrating performance comparable to the established (20 wt.% Pt) Pt/C benchmark (Figure 30a). Notably, pristine $W_{18}O_{49}$ exhibited negligible HER activity in both illuminated and non-illuminated conditions. However, the incorporation of platinum nanoparticles significantly enhanced the composite's HER performance. Interestingly, normalization of LSV data to the mass of platinum (Figure 30b) shown superior HER performance for all synthesized materials compared to the reference Pt/C catalyst.

This finding suggests that the $W_{18}O_{49}$ substrate offers a compelling advantage over conventional carbon supports for HER applications. In this context, the $W_{18}O_{49}$ substrate is believed to facilitate the generation of hot electrons under light irradiation. These hot electrons can be transferred to Pt active sites, thereby promoting the HER kinetics. However, the light-induced enhancement diminishes at higher Pt concentrations ($Pt_{1.6}/W_{18}O_{49}$). This phenomenon is likely attributed to a diminishing plasmonic effect by the vanishment of the W^{5+} species and probably the OVs as increased Pt on the $W_{18}O_{49}$ (as observed in the XPS for W 4f in Figure 29b) that restricts the generation of hot electrons, thereby minimizing the influence of light.

Our study demonstrates the exceptional stability of the $Pt_{1.6}/W_{18}O_{49}$ material for the HER. As illustrated in Figure 30c, a 24-hour chronopotentiometry test conducted at a current density of -10 mA cm^{-2} revealed superior stability of the $Pt_{1.6}/W_{18}O_{49}$ sample compared to others. This enhanced stability signifies the system's superior durability for HER under these demanding conditions. Furthermore, Electrochemical impedance spectroscopy (EIS) analysis further elucidates the electrocatalytic kinetics. The Nyquist plot (Figure 30d) reveals a significantly lower charge transfer resistance for the $Pt_{1.6}/W_{18}O_{49}$ sample compared to others. This finding implies superior electrical conductivity and faster HER kinetics due to the reduced resistance. Interestingly, the EIS spectra for $Pt_{0.4}/W_{18}O_{49}$ and $Pt_{0.8}/W_{18}O_{49}$ demonstrate lower resistance under light illumination compared to dark conditions, suggesting that the plasmonic $W_{18}O_{49}$ enhances Pt catalytic activity under light.

The Tafel slopes obtained (Figure 30e) provide insight into the HER mechanism. The low value of 23 mV per decade for the $Pt_{1.6}/W_{18}O_{49}$ sample suggests a Volmer-Heyrovsky mechanism with the rate-determining step being electrochemical desorption. This finding aligns with the faster reaction kinetics observed for this sample compared to commercial Pt/C (33 mV per decade) and with established literature values (162 mV per decade for bare $W_{18}O_{49}$). Notably, the Tafel slopes for $Pt_{0.4}/W_{18}O_{49}$ (31 mV per decade) and $Pt_{0.8}/W_{18}O_{49}$ (25 mV per decade) decrease with increasing Pt content, indicating a positive correlation between Pt concentration and the availability of active sites. Lower Tafel slopes for Pt-supported $W_{18}O_{49}$ compared to Pt/C suggest a greater abundance of active catalytic sites. Overpotential measurements (Figure 30f) reveal a decreasing trend in overpotential required for HER with increasing Pt content. Lower overpotential signifies a lower resistance to initiate HER.

4.5 Discussion

Comprehensive characterization techniques unanimously corroborate the successful introduction of Pt nanoparticles onto the surface of plasmonic $W_{18}O_{49}$. The subsequent optimization process for Pt loading prioritized the preservation of plasmonic properties and the utilization of LSPR-generated hot electrons for catalytic activity, all while ensuring cost-effective Pt usage. UV-Vis spectroscopy revealed a systematic attenuation of the plasmonic band centered at 720 nm with increasing Pt content. Notably, XRD and Raman analyses exhibited minimal variations, potentially attributable to the subtle changes in Pt concentration. Consequently, XPS analysis was solely employed for the sample demonstrating the most promising performance. The XPS data unequivocally confirmed the successful integration of Pt into the $W_{18}O_{49}$ nanowires, accompanied by a concomitant alteration of the electronic structure. This observation strongly suggests the interaction of Pt in the $W_{18}O_{49}$ substrate and overall increasing catalytic performance.

This study explores the potential of plasmonic and defect-rich $W_{18}O_{49}$ as a platform for enhanced HER system. We demonstrate the remarkable intrinsic capability of tungsten oxide itself to dissociate water molecules, leading to a significant reduction in the HER energy barrier and accelerated reaction kinetics. Furthermore, the presence of oxygen vacancies facilitates efficient electron transfer, promote the HER process as itself behaves as metallic and combined effect with low amount of Pt significantly improved the system for sustainable and durable HER. These findings are substantiated by the LSV data, which clearly illustrate the limited inherent HER activity of pristine $W_{18}O_{49}$. However, the introduction of small amount of Pt leads to a dramatic enhancement in HER performance. Remarkably, even after normalization of the current density by Pt mass, the Pt supported $W_{18}O_{49}$ catalysts exhibit superior activity compared to the commercially available (20% wt. of Pt) Pt/C catalyst**.**

4.6 Conclusion

Our study conclusively demonstrates the efficacy of defect-rich plasmonic $W_{18}O_{49}$ as a support material for acidic water splitting, enabling efficient hydrogen evolution reaction even with minimal platinum content. This engineered composite, comprised of small Pt nanoparticles loaded onto tungsten oxide, exhibits analogous performance compared to commercial Pt/C catalysts, achieving lower overpotential and smaller Tafel slopes. The observed performance enhancement can be attributed to the synergistic effect of $W_{18}O_{49}$ towards water splitting acceleration and improved electron transfer capability. Notably, Pt supported $W_{18}O_{49}$ demonstrates superior performance (when normalized by Pt mass) and overall comparable performance compared to 20% Pt/C. Strong interaction between Pt and the $W_{18}O_{49}$ support as confirmed by XPS, and other characterization. This work paves the way for the utilization of earth-abundant and cost-effective plasmonic materials as supports for ultra-low noble metal catalysts, promoting the development of active, durable, and efficient electrocatalysts for acidic water-splitting applications. Further research can capitalize on this breakthrough by exploring alternative earth-abundant transition metals or alloys to replace platinum entirely. This could significantly reduce costs while maintaining or potentially improving catalytic activity. Additionally, investigation into the optimal size and distribution of Pt nanoparticles on the $W_{18}O_{49}$ support presents an opportunity for further performance optimization. Furthermore, long-term stability testing under realistic operating conditions is crucial to evaluate the suitability of these novel catalysts for practical water splitting applications. Finally, research into scalable fabrication processes is essential for the transition from fundamental research to real-world implementation and large-scale hydrogen production.

5. References

(1) Lewis, N. S.; Nocera, D. G. Powering the Planet: Chemical Challenges in Solar Energy Utilization. *Proc Natl Acad Sci U S A* **2006**, *103* (43), 15729–15735. https://doi.org/10.1073/PNAS.0603395103/ASSET/3DE8043E-D8A1-44B0-AFD0-FD0C4CC001CE/ASSETS/GRAPHIC/ZPQ03906360600E4.JPEG.

(2) *RENEWABLES 2018 GLOBAL STATUS REPORT*. https://www.ren21.net/gsr-2018/ (accessed 2024-03-07).

(3) Zhu, J.; Hu, L.; Zhao, P.; Lee, L. Y. S.; Wong, K. Y. Recent Advances in Electrocatalytic Hydrogen Evolution Using Nanoparticles. *Chem Rev* **2020**, *120* (2), 851–918. https://doi.org/10.1021/ACS.CHEMREV.9B00248.

(4) Elam, C. C.; Padró, C. E. G.; Sandrock, G.; Luzzi, A.; Lindblad, P.; Hagen, E. F. Realizing the Hydrogen Future: The International Energy Agency's Efforts to Advance Hydrogen Energy Technologies. *Int J Hydrogen Energy* **2003**, *28* (6), 601–607. https://doi.org/10.1016/S0360-3199(02)00147-7.

(5) Edwards, P. P.; Kuznetsov, V. L.; David, W. I. F. Hydrogen Energy. *Philosophical Transactions of the Royal Society A: Mathematical, Physical and Engineering Sciences* **2007**, *365* (1853), 1043–1056. https://doi.org/10.1098/RSTA.2006.1965.

(6) Nanda, S.; Li, K.; Abatzoglou, N.; Dalai, A. K.; Kozinski, J. A. Advancements and Confinements in Hydrogen Production Technologies. *Bioenergy Systems for the Future: Prospects for Biofuels and Biohydrogen* **2017**, 373–418. https://doi.org/10.1016/B978-0-08-101031-0.00011-9.

(7) Epelle, E. I.; Desongu, K. S.; Obande, W.; Adeleke, A. A.; Ikubanni, P. P.; Okolie, J. A.; Gunes, B. A Comprehensive Review of Hydrogen Production and Storage: A Focus on the Role of Nanomaterials. *Int J Hydrogen Energy* **2022**, *47* (47), 20398–20431. https://doi.org/10.1016/J.IJHYDENE.2022.04.227.

(8) Zhu, J.; Hu, L.; Zhao, P.; Lee, L. Y. S.; Wong, K. Y. Recent Advances in Electrocatalytic Hydrogen Evolution Using Nanoparticles. *Chem Rev* **2020**, *120* (2), 851–918. https://doi.org/10.1021/ACS.CHEMREV.9B00248.

(9) Sheng, W.; Myint, M.; Chen, J. G.; Yan, Y. Correlating the Hydrogen Evolution Reaction Activity in Alkaline Electrolytes with the Hydrogen Binding Energy on Monometallic Surfaces. *Energy Environ Sci* **2013**, *6* (5), 1509–1512. https://doi.org/10.1039/C3EE00045A.

(10) None, N. A National Vision of America's Transition to a Hydrogen Economy. To 2030 and Beyond. **2002**. https://doi.org/10.2172/1216144.

(11) Cheng, N.; Stambula, S.; Wang, D.; Banis, M. N.; Liu, J.; Riese, A.; Xiao, B.; Li, R.; Sham, T. K.; Liu, L. M.; Botton, G. A.; Sun, X. Platinum Single-Atom and Cluster Catalysis of the Hydrogen Evolution Reaction. *Nat Commun* **2016**, *7*. https://doi.org/10.1038/NCOMMS13638.

(12) Walter, M. G.; Warren, E. L.; McKone, J. R.; Boettcher, S. W.; Mi, Q.; Santori, E. A.; Lewis, N. S. Solar Water Splitting Cells. *Chem Rev* **2010**, *110* (11), 6446–6473. https://doi.org/10.1021/CR1002326.

(13) Zeng, M.; Li, Y. Recent Advances in Heterogeneous Electrocatalysts for the Hydrogen Evolution Reaction. *J Mater Chem A Mater* **2015**, *3* (29), 14942–14962. https://doi.org/10.1039/C5TA02974K.

(14) Kumar, A.; Xu, Q. Two-Dimensional Layered Materials as Catalyst Supports. *ChemNanoMat* **2018**, *4* (1), 28–40. https://doi.org/10.1002/CNMA.201700139.

(15) Greeley, J.; Jaramillo, T. F.; Bonde, J.; Chorkendorff, I.; Nørskov, J. K. Computational High-Throughput Screening of Electrocatalytic Materials for Hydrogen Evolution. *Nat Mater* **2006**, *5* (11), 909–913. https://doi.org/10.1038/NMAT1752.

(16) Tan, T. L.; Wang, L. L.; Zhang, J.; Johnson, D. D.; Bai, K. Platinum Nanoparticle during Electrochemical Hydrogen Evolution: Adsorbate Distribution, Active Reaction Species, and Size Effect. *ACS Catal* **2015**, *5* (4), 2376–2383. https://doi.org/10.1021/CS501840C/ASSET/IMAGES/LARGE/CS-2014-01840C_0004.JPEG.

(17) Nosheen, F.; Zhang, Z.; Xiang, G.; Xu, B.; Yang, Y.; Saleem, F.; Xu, X.; Zhang, J.; Wang, X. Three-Dimensional Hierarchical Pt-Cu Superstructures. *Nano Res* **2015**, *8* (3), 832–838. https://doi.org/10.1007/S12274-014-0565-1/METRICS.

(18) Zou, X.; Zhang, Y. Noble Metal-Free Hydrogen Evolution Catalysts for Water Splitting. *Chem Soc Rev* **2015**, *44* (15), 5148–5180. https://doi.org/10.1039/C4CS00448E.

(19) Cortie, M. B. The Weird World of Nanoscale Gold. *Gold Bull* **2004**, *37* (1–2), 12–19. https://doi.org/10.1007/BF03215512/METRICS.

(20) Li, Y.; Zhang, H.; Xu, T.; Lu, Z.; Wu, X.; Wan, P.; Sun, X.; Jiang, L. Under-Water Superaerophobic Pine-Shaped Pt Nanoarray Electrode for Ultrahigh-Performance Hydrogen Evolution. *Adv Funct Mater* **2015**, *25* (11), 1737–1744. https://doi.org/10.1002/ADFM.201404250.

(21) Rycenga, M.; Cobley, C. M.; Zeng, J.; Li, W.; Moran, C. H.; Zhang, Q.; Qin, D.; Xia, Y. Controlling the Synthesis and Assembly of Silver Nanostructures for Plasmonic Applications. *Chem Rev* **2011**, *111* (6), 3669–3712. https://doi.org/10.1021/CR100275D.

(22) Xia, Y.; Xiong, Y.; Lim, B.; Skrabalak, S. E. Shape-Controlled Synthesis of Metal Nanocrystals: Simple Chemistry Meets Complex Physics? *Angew Chem Int Ed Engl* **2009**, *48* (1), 60–103. https://doi.org/10.1002/ANIE.200802248.

(23) Huang, X.; Tang, S.; Mu, X.; Dai, Y.; Chen, G.; Zhou, Z.; Ruan, F.; Yang, Z.; Zheng, N. Freestanding Palladium Nanosheets with Plasmonic and Catalytic Properties. *Nature Nanotechnology 2011 6:1* **2010**, *6* (1), 28–32. https://doi.org/10.1038/nnano.2010.235.

(24) Daniel, M.; Astruc, D. Gold Nanoparticles: Assembly, Supramolecular Chemistry, Quantum-Size-Related Properties, and Applications Toward Biology, Catalysis, and Nanotechnology. *ChemInform* **2004**, *35* (16). https://doi.org/10.1002/CHIN.200416213.

(25) Burda, C.; Chen, X.; Narayanan, R.; El-Sayed, M. A. Chemistry and Properties of Nanocrystals of Different Shapes. *Chem Rev* **2005**, *105* (4), 1025–1102. https://doi.org/10.1021/CR030063A/ASSET/IMAGES/MEDIUM/CR030063AF00001.GIF.

(26) Polshettiwar, V.; Varma, R. S. Green Chemistry by Nano-Catalysis. *Green Chemistry* **2010**, *12* (5), 743–754. https://doi.org/10.1039/B921171C.

(27) Cole-Hamilton, D. J. Homogeneous Catalysis--New Approaches to Catalyst Separation, Recovery, and Recycling. *Science* **2003**, *299* (5613), 1702–1706. https://doi.org/10.1126/SCIENCE.1081881.

(28) Mitchell, S.; Qin, R.; Zheng, N.; Pérez-Ramírez, J. Nanoscale Engineering of Catalytic Materials for Sustainable Technologies. *Nature Nanotechnology 2020 16:2* **2020**, *16* (2), 129–139. https://doi.org/10.1038/s41565-020-00799-8.

(29) Friend, C. M.; Xu, B. Heterogeneous Catalysis: A Central Science for a Sustainable Future. *Acc Chem Res* **2017**, *50* (3), 517–521. https://doi.org/10.1021/ACS.ACCOUNTS.6B00510/ASSET/IMAGES/LARGE/AR-2016-00510E_0003.JPEG.

(30) McCash, E. Surface Chemistry / Elaine M. McCash. **2001**.

(31) Tan, T. L.; Wang, L. L.; Zhang, J.; Johnson, D. D.; Bai, K. Platinum Nanoparticle during Electrochemical Hydrogen Evolution: Adsorbate Distribution, Active Reaction Species, and Size Effect. *ACS Catal* **2015**, *5* (4), 2376–2383. https://doi.org/10.1021/CS501840C/ASSET/IMAGES/LARGE/CS-2014-01840C_0004.JPEG.

(32) Kaneda, K.; Ebitani, K.; Mizugaki, T.; Mori, K. Design of High-Performance Heterogeneous Metal Catalysts for Green and Sustainable Chemistry. *Bull Chem Soc Jpn* **2006**, *79* (7), 981–1016. https://doi.org/10.1246/BCSJ.79.981.

(33) Oh, A.; Sa, Y. J.; Hwang, H.; Baik, H.; Kim, J.; Kim, B.; Joo, S. H.; Lee, K. Rational Design of Pt–Ni–Co Ternary Alloy Nanoframe Crystals as Highly Efficient Catalysts toward the Alkaline Hydrogen Evolution Reaction. *Nanoscale* **2016**, *8* (36), 16379–16386. https://doi.org/10.1039/C6NR04572C.

(34) Chen, C.; Kang, Y.; Huo, Z.; Zhu, Z.; Huang, W.; Xin, H. L.; Snyder, J. D.; Li, D.; Herron, J. A.; Mavrikakis, M.; Chi, M.; More, K. L.; Li, Y.; Markovic, N. M.; Somorjai, G. A.; Yang, P.; Stamenkovic, V. R. Highly Crystalline Multimetallic Nanoframes with Three-Dimensional Electrocatalytic Surfaces. *Science (1979)* **2014**, *343* (6177), 1339–1343. https://doi.org/10.1126/SCIENCE.1249061.

(35) Jang, H. J.; Hong, S.; Park, S. Shape-Controlled Synthesis of Pt Nanoframes. *J Mater Chem* **2012**, *22* (37), 19792–19797. https://doi.org/10.1039/C2JM34187E.

(36) *Mahata, A.; Rawat, K. S.; Choudhuri, I.; Pathak, B. Single layered platinum nanocage: a highly selective and efficient catalyst for fuel cells. J. Mater. Chem. A 2016, 4, 12756–12767 - Search.* https://www.bing.com/search?q=Mahata%2C+A.%3B+Rawat%2C+K.+S.%3B+Choudhuri%2C+I.%3B+Pathak%2C+B.+Single%02layered+platinum+nanocage%3A+a+highly+selective+and+efficient+catalyst+for+fuel+cells.+J.+Mater.+Chem.+A+2016%2C+4%2C+12756%E2%88%9212767&qs=n&form=QBRE&sp=-1&lq=1&pq=mahata%2C+a.%3B+rawat%2C+k.+s.%3B+choudhuri%2C+i.%3B+pathak%2C+b.+single%02layered+platinum+nanocage%3A+a+highly+selective+and+efficient+catalyst+for+fuel+cells.+j.+mater.+chem.+a+2016%2C+4%2C+12756%E2%88%9212767&sc=0-182&sk=&cvid=172C0D2D8F4E4D55BDA3679DD07322FC&ghsh=0&ghacc=0&ghpl= (accessed 2024-03-19).

(37) Cao, Z.; Li, H.; Zhan, C.; Zhang, J.; Wang, W.; Xu, B.; Lu, F.; Jiang, Y.; Xie, Z.; Zheng, L. Monocrystalline Platinum-Nickel Branched Nanocages with Enhanced Catalytic Performance towards the Hydrogen Evolution Reaction. *Nanoscale* **2018**, *10* (11), 5072–5077. https://doi.org/10.1039/C7NR09116H.

(38) Wang, S.; Yang, G.; Yang, S. Pt-Frame@Ni Quasi Core–Shell Concave Octahedral PtNi3 Bimetallic Nanocrystals for Electrocatalytic Methanol Oxidation and Hydrogen Evolution. *Journal of Physical Chemistry C* **2015**, *119* (50), 27938–27945. https://doi.org/10.1021/ACS.JPCC.5B10083.

(39) He, D.; Zhang, L.; He, D.; Zhou, G.; Lin, Y.; Deng, Z.; Hong, X.; Wu, Y.; Chen, C.; Li, Y. Amorphous Nickel Boride Membrane on a Platinum–Nickel Alloy Surface for Enhanced Oxygen Reduction Reaction. *Nature Communications 2016 7:1* **2016**, *7* (1), 1–8. https://doi.org/10.1038/ncomms12362.

(40) Hsu, I. J.; Kimmel, Y. C.; Jiang, X.; Willis, B. G.; Chen, J. G. Atomic Layer Deposition Synthesis of Platinum-Tungsten Carbide Core-Shell Catalysts for the Hydrogen Evolution Reaction. *Chem Commun (Camb)* **2012**, *48* (7), 1063–1065. https://doi.org/10.1039/C1CC15812K.

(41) Yin, H.; Zhao, S.; Zhao, K.; Muqsit, A.; Tang, H.; Chang, L.; Zhao, H.; Gao, Y.; Tang, Z. Ultrathin Platinum Nanowires Grown on Single-Layered Nickel

Hydroxide with High Hydrogen Evolution Activity. *Nat Commun* **2015**, *6*. https://doi.org/10.1038/NCOMMS7430.

(42) Zhu, E.; Yan, X.; Wang, S.; Xu, M.; Wang, C.; Liu, H.; Huang, J.; Xue, W.; Cai, J.; Heinz, H.; Li, Y.; Huang, Y. Peptide-Assisted 2-D Assembly toward Free-Floating Ultrathin Platinum Nanoplates as Effective Electrocatalysts. *Nano Lett* **2019**, *19* (6), 3730–3736. https://doi.org/10.1021/ACS.NANOLETT.9B00867.

(43) Ji, L.; Wang, J.; Zuo, S.; Chen, Z. In Situ Preparation of Pt Nanoparticles Supported on N-Doped Carbon as Highly Efficient Electrocatalysts for Hydrogen Production. *Journal of Physical Chemistry C* **2017**, *121* (16), 8923–8930. https://doi.org/10.1021/ACS.JPCC.7B01447.

(44) Tan, T. L.; Wang, L. L.; Zhang, J.; Johnson, D. D.; Bai, K. Platinum Nanoparticle during Electrochemical Hydrogen Evolution: Adsorbate Distribution, Active Reaction Species, and Size Effect. *ACS Catal* **2015**, *5* (4), 2376–2383. https://doi.org/10.1021/CS501840C.

(45) Nosheen, F.; Zhang, Z.; Xiang, G.; Xu, B.; Yang, Y.; Saleem, F.; Xu, X.; Zhang, J.; Wang, X. Three-Dimensional Hierarchical Pt-Cu Superstructures. *Nano Res* **2015**, *8* (3), 832–838. https://doi.org/10.1007/S12274-014-0565-1/METRICS.

(46) Klinkova, A.; Larin, E. M.; Prince, E.; Sargent, E. H.; Kumacheva, E. Large-Scale Synthesis of Metal Nanocrystals in Aqueous Suspensions. *Chemistry of Materials* **2016**, *28* (9), 3196–3202. https://doi.org/10.1021/ACS.CHEMMATER.6B00936.

(47) Jana, R.; Bhim, A.; Bothra, P.; Pati, S. K.; Peter, S. C. Electrochemical Dealloying of PdCu3 Nanoparticles to Achieve Pt-like Activity for the Hydrogen Evolution Reaction. *ChemSusChem* **2016**, *9* (20), 2922–2927. https://doi.org/10.1002/CSSC.201601081.

(48) Chen, J.; Lim, B.; Lee, E. P.; Xia, Y. Shape-Controlled Synthesis of Platinum Nanocrystals for Catalytic and Electrocatalytic Applications. *Nano Today* **2009**, *4* (1), 81–95. https://doi.org/10.1016/J.NANTOD.2008.09.002.

(49) Somorjai, G. A.; Frei, H.; Park, J. Y. Advancing the Frontiers in Nanocatalysis, Biointerfaces, and Renewable Energy Conversion by Innovations of Surface

Techniques. *J Am Chem Soc* **2009**, *131* (46), 16589–16605. https://doi.org/10.1021/JA9061954.

(50) Appleby, A. J. From Sir William Grove to Today: Fuel Cells and the Future. *J Power Sources* **1990**, *29* (1–2), 3–11. https://doi.org/10.1016/0378-7753(90)80002-U.

(51) Yu, X.; Ye, S. Recent Advances in Activity and Durability Enhancement of Pt/C Catalytic Cathode in PEMFC: Part I. Physico-Chemical and Electronic Interaction between Pt and Carbon Support, and Activity Enhancement of Pt/C Catalyst. *J Power Sources* **2007**, *172* (1), 133–144. https://doi.org/10.1016/J.JPOWSOUR.2007.07.049.

(52) Antolini, E. Carbon Supports for Low-Temperature Fuel Cell Catalysts. *Appl Catal B* **2009**, *88* (1–2), 1–24. https://doi.org/10.1016/J.APCATB.2008.09.030.

(53) Luo, Y.; Alonso-Vante, N. The Effect of Support on Advanced Pt-Based Cathodes towards the Oxygen Reduction Reaction. State of the Art. *Electrochim Acta* **2015**, *179*, 108–118. https://doi.org/10.1016/J.ELECTACTA.2015.04.098.

(54) Wang, M.; Lv, H.; Dong, B.; He, W.; Yuan, D.; Wang, X.; Wang, R. Photoelectron Migration Boosted by Hollow Double-Shell Dyads Based on Covalent Organic Frameworks for Highly Efficient Photocatalytic Hydrogen Generation. *Angewandte Chemie International Edition* **2024**, e202401969. https://doi.org/10.1002/ANIE.202401969.

(55) Wang, S.; Lu, A.; Zhong, C. J. Hydrogen Production from Water Electrolysis: Role of Catalysts. *Nano Converg* **2021**, *8* (1). https://doi.org/10.1186/S40580-021-00254-X.

(56) Sun, Y.; Wu, Q.; Shi, G. Graphene Based New Energy Materials. *Energy Environ Sci* **2011**, *4* (4), 1113–1132. https://doi.org/10.1039/C0EE00683A.

(57) Antolini, E. Graphene as a New Carbon Support for Low-Temperature Fuel Cell Catalysts. *Appl Catal B* **2012**, *123–124*, 52–68. https://doi.org/10.1016/J.APCATB.2012.04.022.

(58) Lv, H.; Mu, S. Nano-Ceramic Support Materials for Low Temperature Fuel Cell Catalysts. *Nanoscale* **2014**, *6* (10), 5063–5074. https://doi.org/10.1039/C4NR00402G.

(59) Cho, K. Y.; Yeom, Y. S.; Seo, H. Y.; Lee, A. S.; Huy Do, X.; Hong, J. P.; Jeong, H. K.; Baek, K. Y.; Yoon, H. G. Fine-Sized Pt Nanoparticles Dispersed on PdPt Bimetallic Nanocrystals with Non-Covalently Functionalized Graphene toward Synergistic Effects on the Oxygen Reduction Reaction. *Electrochim Acta* **2017**, *257*, 412–422. https://doi.org/10.1016/J.ELECTACTA.2017.10.075.

(60) Wang, Y.; Luo, W.; Gong, S.; Luo, L.; Li, Y.; Zhao, Y.; Li, Z. Synthesis of High-Entropy-Alloy Nanoparticles by a Step-Alloying Strategy as a Superior Multifunctional Electrocatalyst. *Advanced Materials* **2023**, *35* (36), 2302499. https://doi.org/10.1002/ADMA.202302499.

(61) Li, D.; Wang, C.; Strmcnik, D. S.; Tripkovic, D. V.; Sun, X.; Kang, Y.; Chi, M.; Snyder, J. D.; Van Der Vliet, D.; Tsai, Y.; Stamenkovic, V. R.; Sun, S.; Markovic, N. M. Functional Links between Pt Single Crystal Morphology and Nanoparticles with Different Size and Shape: The Oxygen Reduction Reaction Case. *Energy Environ Sci* **2014**, *7* (12), 4061–4069. https://doi.org/10.1039/C4EE01564A.

(62) Park, J.; You, I.; Shin, S.; Jeong, U. Material Approaches to Stretchable Strain Sensors. *ChemPhysChem* **2015**, *16* (6), 1155–1163. https://doi.org/10.1002/CPHC.201402810.

(63) Bagheri, S.; Muhd Julkapli, N.; Bee Abd Hamid, S. Titanium Dioxide as a Catalyst Support in Heterogeneous Catalysis. *Scientific World Journal* **2014**, *2014*. https://doi.org/10.1155/2014/727496.

(64) Wu, X.; Zhuang, W.; Lu, L.; Li, L.; Zhu, J.; Mu, L.; Li, W.; Zhu, Y.; Lu, X. Excellent Performance of Pt-C/TiO2 for Methanol Oxidation: Contribution of Mesopores and Partially Coated Carbon. *Appl Surf Sci* **2017**, *426*, 890–896. https://doi.org/10.1016/J.APSUSC.2017.07.219.

(65) Huynh, T. T.; Pham, H. Q.; Nguyen, A. Van; Nguyen, S. T.; Bach, L. G.; Ho, V. T. T. High Conductivity and Surface Area of Mesoporous Ti 0.7 W 0.3 O 2 Materials as Promising Catalyst Support for Pt in Proton-Exchange Membrane Fuel Cells

. *J Nanosci Nanotechnol* **2018**, *19* (2), 877–881. https://doi.org/10.1166/JNN.2019.15937.

(66) Yao, C.; Li, F.; Li, X.; Xia, D. Fiber-like Nanostructured Ti4O7 Used as Durable Fuel Cell Catalyst Support in Oxygen Reduction Catalysis. *J Mater Chem* **2012**, *22* (32), 16560–16565. https://doi.org/10.1039/C2JM32866F.

(67) Pan, C. J.; Tsai, M. C.; Su, W. N.; Rick, J.; Akalework, N. G.; Agegnehu, A. K.; Cheng, S. Y.; Hwang, B. J. Tuning/Exploiting Strong Metal-Support Interaction (SMSI) in Heterogeneous Catalysis. *J Taiwan Inst Chem Eng* **2017**, *74*, 154–186. https://doi.org/10.1016/J.JTICE.2017.02.012.

(68) Hsieh, B. J.; Tsai, M. C.; Pan, C. J.; Su, W. N.; Rick, J.; Chou, H. L.; Lee, J. F.; Hwang, B. J. Tuning Metal Support Interactions Enhances the Activity and Durability of TiO2-Supported Pt Nanocatalysts. *Electrochim Acta* **2017**, *224*, 452–459. https://doi.org/10.1016/J.ELECTACTA.2016.12.020.

(69) Li, F.; Gong, H.; Wang, Y.; Zhang, H.; Wang, Y.; Liu, S.; Wang, S.; Sun, C. Enhanced Activity, Durability and Anti-Poisoning Property of Pt/W18O49 for Methanol Oxidation with a Sub-Stoichiometric Tungsten Oxide W18O49 Support. *J Mater Chem A Mater* **2014**, *2* (47), 20154–20163. https://doi.org/10.1039/C4TA04220D.

(70) Yang, M. Q.; Wang, J.; Wu, H.; Ho, G. W. Noble Metal-Free Nanocatalysts with Vacancies for Electrochemical Water Splitting. *Small* **2018**, *14* (15), 1703323. https://doi.org/10.1002/smll.201703323.

(71) Song, J.; Huang, Z. F.; Pan, L.; Zou, J. J.; Zhang, X.; Wang, L. Oxygen-Deficient Tungsten Oxide as Versatile and Efficient Hydrogenation Catalyst. *ACS Catal* **2015**, *5* (11), 6594–6599. https://doi.org/10.1021/ACSCATAL.5B01522/ASSET/IMAGES/LARGE/CS-2015-01522V_0006.JPEG.

(72) Yang, M.-Q.; Wang, J.; Wu, H.; Ho, G. W.; Yang, M.-Q.; Wang, J.; Wu, H.; Ho, G. W. Noble Metal-free Nanocatalysts with Vacancies for Electrochemical Water Splitting. *Wiley Online LibraryMQ Yang, J Wang, H Wu, GW HoSmall, 2018•Wiley Online Library* **2018**, *14* (15). https://doi.org/10.1002/smll.201703323.

(73) Zhou, H.; Shi, Y.; Dong, Q.; Lin, J.; Wang, A.; Ma, T. Surface Oxygen Vacancy-Dependent Electrocatalytic Activity of W18O49 Nanowires. *Journal of Physical Chemistry C* **2014**, *118* (35), 20100–20106. https://doi.org/10.1021/JP504368V/SUPPL_FILE/JP504368V_SI_001.PDF.

(74) Kimmel, Y. C.; Xu, X.; Yu, W.; Yang, X.; Chen, J. G. Trends in Electrochemical Stability of Transition Metal Carbides and Their Potential Use as Supports for Low-Cost Electrocatalysts. *ACS Catal* **2014**, *4* (5), 1558–1562. https://doi.org/10.1021/CS500182H/ASSET/IMAGES/LARGE/CS-2014-00182H_0005.JPEG.

(75) Tang, C.; Wang, D.; Wu, Z.; Duan, B. Tungsten Carbide Hollow Microspheres as Electrocatalyst and Platinum Support for Hydrogen Evolution Reaction. *Int J Hydrogen Energy* **2015**, *40* (8), 3229–3237. https://doi.org/10.1016/J.IJHYDENE.2014.12.105.

(76) Jiang, Y.; Wu, X.; Yan, Y.; Luo, S.; Li, X.; Huang, J.; Zhang, H.; Yang, D. Coupling PtNi Ultrathin Nanowires with MXenes for Boosting Electrocatalytic Hydrogen Evolution in Both Acidic and Alkaline Solutions. *Small* **2019**, *15* (12). https://doi.org/10.1002/SMLL.201805474.

(77) Zhang, J.; Zhao, Y.; Guo, X.; Chen, C.; Dong, C. L.; Liu, R. S.; Han, C. P.; Li, Y.; Gogotsi, Y.; Wang, G. Single Platinum Atoms Immobilized on an MXene as an Efficient Catalyst for the Hydrogen Evolution Reaction. *Nature Catalysis 2018 1:12* **2018**, *1* (12), 985–992. https://doi.org/10.1038/s41929-018-0195-1.

(78) Ding, L. X.; Wang, A. L.; Li, G. R.; Liu, Z. Q.; Zhao, W. X.; Su, C. Y.; Tong, Y. X. Porous Pt-Ni-P Composite Nanotube Arrays: Highly Electroactive and Durable Catalysts for Methanol Electrooxidation. *J Am Chem Soc* **2012**, *134* (13), 5730–5733. https://doi.org/10.1021/JA212206M/SUPPL_FILE/JA212206M_SI_001.PDF.

(79) Hoque, M. A.; Hassan, F. M.; Jauhar, A. M.; Jiang, G.; Pritzker, M.; Choi, J. Y.; Knights, S.; Ye, S.; Chen, Z. Web-like 3D Architecture of Pt Nanowires and Sulfur-Doped Carbon Nanotube with Superior Electrocatalytic Performance. *ACS Sustain Chem Eng* **2018**, *6* (1), 93–98. https://doi.org/10.1021/ACSSUSCHEMENG.7B03580.

(80) Venarusso, L. B.; Boone, C. V.; Bettini, J.; Maia, G. Carbon-Supported Metal Nanodendrites as Efficient, Stable Catalysts for the Oxygen Reduction Reaction. *J Mater Chem* **2018**, *6* (4), 1714–1726. https://doi.org/10.1039/C7TA08964C.

(81) Grozovski, V.; Kasuk, H.; Nerut, J.; Härk, E.; Jäger, R.; Tallo, I.; Lust, E. Oxygen Reduction at Shape-Controlled Platinum Nanoparticles and Composite Catalysts Based on (100)Pt Nanocubes on Microporous–Mesoporous Carbon Supports. *ChemElectroChem* **2015**, *2* (6), 847–851. https://doi.org/10.1002/CELC.201500021.

(82) Hoque, M. A.; Hassan, F. M.; Jauhar, A. M.; Jiang, G.; Pritzker, M.; Choi, J. Y.; Knights, S.; Ye, S.; Chen, Z. Web-like 3D Architecture of Pt Nanowires and Sulfur-Doped Carbon Nanotube with Superior Electrocatalytic Performance. *ACS Sustain Chem Eng* **2018**, *6* (1), 93–98. https://doi.org/10.1021/ACSSUSCHEMENG.7B03580.

(83) Tian, X. L.; Wang, L.; Deng, P.; Chen, Y.; Xia, B. Y. Research Advances in Unsupported Pt-Based Catalysts for Electrochemical Methanol Oxidation. *Journal of Energy Chemistry* **2017**, *26* (6), 1067–1076. https://doi.org/10.1016/J.JECHEM.2017.10.009.

(84) Bhunia, K.; Khilari, S.; Pradhan, D. Trimetallic PtAuNi Alloy Nanoparticles as an Efficient Electrocatalyst for the Methanol Electrooxidation Reaction. *Dalton Transactions* **2017**, *46* (44), 15558–15566. https://doi.org/10.1039/C7DT02608K.

(85) Omasta, T. J.; Wang, L.; Peng, X.; Lewis, C. A.; Varcoe, J. R.; Mustain, W. E. Importance of Balancing Membrane and Electrode Water in Anion Exchange Membrane Fuel Cells. *J Power Sources* **2018**, *375*, 205–213. https://doi.org/10.1016/J.JPOWSOUR.2017.05.006.

(86) Sarina, S.; Waclawik, E. R.; Zhu, H. Photocatalysis on Supported Gold and Silver Nanoparticles under Ultraviolet and Visible Light Irradiation. *Green Chemistry* **2013**, *15* (7), 1814–1833. https://doi.org/10.1039/C3GC40450A.

(87) Kelly, K. L.; Coronado, E.; Zhao, L. L.; Schatz, G. C. The Optical Properties of Metal Nanoparticles: The Influence of Size, Shape, and Dielectric Environment. *Journal of Physical Chemistry B* **2003**, *107* (3), 668–677.

https://doi.org/10.1021/JP026731Y/ASSET/IMAGES/LARGE/JP026731YF00014.JPEG.

(88) Baffou, G.; Quidant, R. Nanoplasmonics for Chemistry. *Chem Soc Rev* **2014**, *43* (11), 3898–3907. https://doi.org/10.1039/C3CS60364D.

(89) Aslam, U.; Rao, V. G.; Chavez, S.; Linic, S. Catalytic Conversion of Solar to Chemical Energy on Plasmonic Metal Nanostructures. *Nat Catal* **2018**, *1* (9), 656–665. https://doi.org/10.1038/S41929-018-0138-X.

(90) Linic, S.; Aslam, U.; Boerigter, C.; Morabito, M. Photochemical Transformations on Plasmonic Metal Nanoparticles. *Nat Mater* **2015**, *14* (6), 567–576. https://doi.org/10.1038/NMAT4281.

(91) Brongersma, M. L.; Halas, N. J.; Nordlander, P. Plasmon-Induced Hot Carrier Science and Technology. *Nature Nanotechnology 2015 10:1* **2015**, *10* (1), 25–34. https://doi.org/10.1038/nnano.2014.311.

(92) Li, S.; Miao, P.; Zhang, Y.; Wu, J.; Zhang, B.; Du, Y.; Han, X.; Sun, J.; Xu, P.; Li, S.; Miao, P.; Zhang, Y.; Wu, J.; Zhang, B.; Du, Y.; Han, X.; Sun, J.; Xu, P. Recent Advances in Plasmonic Nanostructures for Enhanced Photocatalysis and Electrocatalysis. *Advanced Materials* **2021**, *33* (6), 2000086. https://doi.org/10.1002/ADMA.202000086.

(93) Fang, Z.; Thongrattanasiri, S.; Schlather, A.; Liu, Z.; Ma, L.; Wang, Y.; Ajayan, P. M.; Nordlander, P.; Halas, N. J.; García De Abajo, F. J. Gated Tunability and Hybridization of Localized Plasmons in Nanostructured Graphene. *ACS Nano* **2013**, *7* (3), 2388–2395. https://doi.org/10.1021/NN3055835.

(94) Knight, M. W.; Sobhani, H.; Nordlander, P.; Halas, N. J. Photodetection with Active Optical Antennas. *Science* **2011**, *332* (6030), 702–704. https://doi.org/10.1126/SCIENCE.1203056.

(95) Clavero, C. Plasmon-Induced Hot-Electron Generation at Nanoparticle/Metal-Oxide Interfaces for Photovoltaic and Photocatalytic Devices. *Nat Photonics* **2014**, *8* (2), 95–103. https://doi.org/10.1038/NPHOTON.2013.238.

(96) Mukherjee, S.; Libisch, F.; Large, N.; Neumann, O.; Brown, L. V.; Cheng, J.; Lassiter, J. B.; Carter, E. A.; Nordlander, P.; Halas, N. J. Hot Electrons Do the

Impossible: Plasmon-Induced Dissociation of H 2 on Au. *Nano Lett* **2013**, *13* (1), 240–247. https://doi.org/10.1021/NL303940Z.

(97) Kale, M. J.; Avanesian, T.; Christopher, P. Direct Photocatalysis by Plasmonic Nanostructures. *ACS Catal* **2014**, *4* (1), 116–128. https://doi.org/10.1021/CS400993W.

(98) Govorov, A. O.; Zhang, H.; Gun'Ko, Y. K. Theory of Photoinjection of Hot Plasmonic Carriers from Metal Nanostructures into Semiconductors and Surface Molecules. *Journal of Physical Chemistry C* **2013**, *117* (32), 16616–16631. https://doi.org/10.1021/JP405430M/ASSET/IMAGES/JP405430M.SOCIAL.JPEG_V03.

(99) Wu, K.; Rodríguez-Córdoba, W. E.; Yang, Y.; Lian, T. Plasmon-Induced Hot Electron Transfer from the Au Tip to CdS Rod in CdS-Au Nanoheterostructures. *Nano Lett* **2013**, *13* (11), 5255–5263. https://doi.org/10.1021/NL402730M/ASSET/IMAGES/NL402730M.SOCIAL.JPEG_V03.

(100) Matlab, O.; Teare, S. W.; Pileggi, L.; Tt, V. Plasmonic Optics Theory and Applications Tutorial Texts Series.

(101) Maier, S. A. PLASMONICS: FUNDAMENTALS AND APPLICATIONS.

(102) Ringe, E. Shapes, Plasmonic Properties, and Reactivity of Magnesium Nanoparticles. *Journal of Physical Chemistry C* **2020**, *124* (29), 15665–15679. https://doi.org/10.1021/ACS.JPCC.0C03871.

(103) Linic, S.; Chavez, S.; Elias, R. Flow and Extraction of Energy and Charge Carriers in Hybrid Plasmonic Nanostructures. *Nature Materials 2021 20:7* **2021**, *20* (7), 916–924. https://doi.org/10.1038/s41563-020-00858-4.

(104) Agrawal, A.; Cho, S. H.; Zandi, O.; Ghosh, S.; Johns, R. W.; Milliron, D. J. Localized Surface Plasmon Resonance in Semiconductor Nanocrystals. *Chem Rev* **2018**, *118* (6), 3121–3207. https://doi.org/10.1021/ACS.CHEMREV.7B00613/ASSET/IMAGES/MEDIUM/CR-2017-006132_M026.GIF.

(105) Shaganov, I. I.; Perova, T. S.; Berwick, K. The Effect of the Local Field and Dipole-Dipole Interactions on the Absorption Spectra of Noble Metals and the Plasmon Resonance of Their Nanoparticles. *Photonics Nanostruct* **2017**, *27*, 24–31. https://doi.org/10.1016/J.PHOTONICS.2017.09.003.

(106) Peng, S.; McMahon, J. M.; Schatz, G. C.; Gray, S. K.; Sun, Y. Reversing the Size-Dependence of Surface Plasmon Resonances. *Proc Natl Acad Sci U S A* **2010**, *107* (33), 14530–14534. https://doi.org/10.1073/PNAS.1007524107.

(107) Kim, S.; Kim, J. M.; Park, J. E.; Nam, J. M. Nonnoble-Metal-Based Plasmonic Nanomaterials: Recent Advances and Future Perspectives. *Advanced Materials* **2018**, *30* (42), 1704528. https://doi.org/10.1002/ADMA.201704528.

(108) Yan, L.; Fu, Z.; Zhang, Z. Plasmon-Induced Hot Electrons in Metallic Nanoparticles. **2022**, 155–175. https://doi.org/10.1007/978-3-030-87544-2_7.

(109) Comin, A.; Manna, L. New Materials for Tunable Plasmonic Colloidal Nanocrystals. *Chem Soc Rev* **2014**, *43* (11), 3957–3975. https://doi.org/10.1039/C3CS60265F.

(110) Agrawal, A.; Cho, S. H.; Zandi, O.; Ghosh, S.; Johns, R. W.; Milliron, D. J. Localized Surface Plasmon Resonance in Semiconductor Nanocrystals. *Chem Rev* **2018**, *118* (6), 3121–3207. https://doi.org/10.1021/ACS.CHEMREV.7B00613/ASSET/IMAGES/MEDIUM/CR-2017-006132_M026.GIF.

(111) Huang, Q.; Hu, S.; Zhuang, J.; Wang, X. MoO3-x-Based Hybrids with Tunable Localized Surface Plasmon Resonances: Chemical Oxidation Driving Transformation from Ultrathin Nanosheets to Nanotubes. *Chemistry - A European Journal* **2012**, *18* (48), 15283–15287. https://doi.org/10.1002/CHEM.201202630.

(112) Manthiram, K.; Alivisatos, A. P. Tunable Localized Surface Plasmon Resonances in Tungsten Oxide Nanocrystals. *J Am Chem Soc* **2012**, *134* (9), 3995–3998. https://doi.org/10.1021/JA211363W/ASSET/IMAGES/JA211363W.SOCIAL.JPEG_V03.

(113) Zhao, Y.; Pan, H.; Lou, Y.; Qiu, X.; Zhu, J.; Burda, C. Plasmonic Cu 2-XS Nanocrystals: Optical and Structural Properties of Copper-Deficient Copper(I) Sulfides. *J Am Chem Soc* **2009**, *131* (12), 4253–4261. https://doi.org/10.1021/JA805655B.

(114) Dickens, P. G.; Crouch-Baker, S.; Weller, M. T. Hydrogen Insertion in Oxides. *Solid State Ion* **1986**, *18–19* (PART 1), 89–97. https://doi.org/10.1016/0167-2738(86)90092-5.

(115) Cheng, H.; Kuwahara, Y.; Yamashita, H. Earth-Abundant Plasmonic Catalysts. *Plasmonic Catalysis: From Fundamentals to Applications* **2021**, 231–259. https://doi.org/10.1002/9783527826971.CH8.

(116) Cheng, H.; Klapproth, M.; Sagaltchik, A.; Li, S.; Thomas, A. Ordered Mesoporous WO2.83: Selective Reduction Synthesis, Exceptional Localized Surface Plasmon Resonance and Enhanced Hydrogen Evolution Reaction Activity. *J Mater Chem A Mater* **2018**, *6* (5), 2249–2256. https://doi.org/10.1039/C7TA09579A.

(117) Cheng, H.; Wen, M.; Ma, X.; Kuwahara, Y.; Mori, K.; Dai, Y.; Huang, B.; Yamashita, H. Hydrogen Doped Metal Oxide Semiconductors with Exceptional and Tunable Localized Surface Plasmon Resonances. *J Am Chem Soc* **2016**, *138* (29), 9316–9324. https://doi.org/10.1021/JACS.6B05396.

(118) Wu, X.; Li, Y.; Zhang, G.; Chen, H.; Li, J.; Wang, K.; Pan, Y.; Zhao, Y.; Sun, Y.; Xie, Y. Photocatalytic CO2 Conversion of Mo0.33WO3 Directly from the Air with High Selectivity: Insight into Full Spectrum-Induced Reaction Mechanism. *J Am Chem Soc* **2019**, *141* (13), 5267–5274. https://doi.org/10.1021/JACS.8B12928.

(119) Cui, J.; Li, Y.; Liu, L.; Chen, L.; Xu, J.; Ma, J.; Fang, G.; Zhu, E.; Wu, H.; Zhao, L.; Wang, L.; Huang, Y. Near-Infrared Plasmonic-Enhanced Solar Energy Harvest for Highly Efficient Photocatalytic Reactions. *Nano Lett* **2015**, *15* (10), 6295–6301. https://doi.org/10.1021/ACS.NANOLETT.5B00950.

(120) Liu, P. H.; Wen, M.; Tan, C. S.; Navlani-García, M.; Kuwahara, Y.; Mori, K.; Yamashita, H.; Chen, L. J. Surface Plasmon Resonance Enhancement of Production of H2 from Ammonia Borane Solution with Tunable Cu2−xS

Nanowires Decorated by Pd Nanoparticles. *Nano Energy* **2017**, *31*, 57–63. https://doi.org/10.1016/J.NANOEN.2016.10.064.

(121) Huang, Z. F.; Song, J.; Pan, L.; Zhang, X.; Wang, L.; Zou, J. J. Tungsten Oxides for Photocatalysis, Electrochemistry, and Phototherapy. *Advanced Materials* **2015**, *27* (36), 5309–5327. https://doi.org/10.1002/ADMA.201501217.

(122) Kim, H. S.; Cook, J. B.; Lin, H.; Ko, J. S.; Tolbert, S. H.; Ozolins, V.; Dunn, B. Oxygen Vacancies Enhance Pseudocapacitive Charge Storage Properties of MoO3–x. *Nature Materials 2016 16:4* **2016**, *16* (4), 454–460. https://doi.org/10.1038/nmat4810.

(123) Yu, H.; Guo, J.; Wang, C.; Zhang, J.; Liu, J.; Dong, G.; Zhong, X.; Diao, X. Essential Role of Oxygen Vacancy in Electrochromic Performance and Stability for WO3-y Films Induced by Atmosphere Annealing. *Electrochim Acta* **2020**, *332*, 135504. https://doi.org/10.1016/J.ELECTACTA.2019.135504.

(124) Cong, S.; Geng, F.; Zhao, Z.; Cong, S.; Zhao, Z.; Geng, F. Tungsten Oxide Materials for Optoelectronic Applications. *Advanced Materials* **2016**, *28* (47), 10518–10528. https://doi.org/10.1002/ADMA.201601109.

(125) Zhou, Z.; Tang, R.; Li, L.; Xiong, S.; Zeng, H.; Zheng, J.; Gong, D.; Huang, Y.; Deng, Y. W18O49-Based Photocatalyst: Enhanced Strategies for Photocatalysis Employment. *Sep Purif Technol* **2023**, *319*, 124028. https://doi.org/10.1016/J.SEPPUR.2023.124028.

(126) Zeb, S.; Sun, G.; Nie, Y.; Xu, H.; Cui, Y.; Advances, X. J.-M.; 2021, undefined. Advanced Developments in Nonstoichiometric Tungsten Oxides for Electrochromic Applications. *pubs.rsc.org* **2021**, *2*, 6839. https://doi.org/10.1039/d1ma00418b.

(127) Liu, J.; Margeat, O.; Dachraoui, W.; Liu, X.; Fahlman, M.; Ackermann, J. Gram-Scale Synthesis of Ultrathin Tungsten Oxide Nanowires and Their Aspect Ratio-Dependent Photocatalytic Activity. *Adv Funct Mater* **2014**, *24* (38), 6029–6037. https://doi.org/10.1002/ADFM.201401261.

(128) Cong, S.; Yuan, Y.; Chen, Z.; Hou, J.; Yang, M.; Su, Y.; Zhang, Y.; Li, L.; Li, Q.; Geng, F.; Zhao, Z. Noble Metal-Comparable SERS Enhancement from Semiconducting Metal Oxides by Making Oxygen Vacancies. *Nature*

Communications 2015 6:1 **2015**, *6* (1), 1–7. https://doi.org/10.1038/ncomms8800.

(129) Zhai, X. P.; Gao, L. F.; Zhang, H.; Peng, Y.; Zhang, X. D.; Wang, Q.; Zhang, H. L. Defect Engineering of Ultrathin WO3 Nanosheets: Implications for Nonlinear Optoelectronic Devices. *ACS Appl Nano Mater* **2022**, *5* (1), 1169–1177. https://doi.org/10.1021/ACSANM.1C03791/ASSET/IMAGES/LARGE/AN1C03791_0007.JPEG.

(130) Li, Y. H.; Liu, P. F.; Pan, L. F.; Wang, H. F.; Yang, Z. Z.; Zheng, L. R.; Hu, P.; Zhao, H. J.; Gu, L.; Yang, H. G. Local Atomic Structure Modulations Activate Metal Oxide as Electrocatalyst for Hydrogen Evolution in Acidic Water. *Nature Communications 2015 6:1* **2015**, *6* (1), 1–7. https://doi.org/10.1038/ncomms9064.

(131) Cheng, H.; Klapproth, M.; Sagaltchik, A.; Li, S.; Thomas, A. Ordered Mesoporous WO2.83: Selective Reduction Synthesis, Exceptional Localized Surface Plasmon Resonance and Enhanced Hydrogen Evolution Reaction Activity. *J Mater Chem A Mater* **2018**, *6* (5), 2249–2256. https://doi.org/10.1039/C7TA09579A.

(132) Yan, J.; Wang, T.; Wu, G.; Dai, W.; Guan, N.; Li, L.; Gong, J.; Yan, J.; Wang, T.; Wu, G.; Dai, W.; Guan, N.; Li, L.; Gong, J. Tungsten Oxide Single Crystal Nanosheets for Enhanced Multichannel Solar Light Harvesting. *Advanced Materials* **2015**, *27* (9), 1580–1586. https://doi.org/10.1002/ADMA.201404792.

(133) Mattox, T. M.; Bergerud, A.; Agrawal, A.; Milliron, D. J. Influence of Shape on the Surface Plasmon Resonance of Tungsten Bronze Nanocrystals. *Chemistry of Materials* **2014**, *26* (5), 1779–1784. https://doi.org/10.1021/CM4030638/SUPPL_FILE/CM4030638_SI_001.PDF.

(134) Cui, G.; Wang, W.; Ma, M.; Xie, J.; Shi, X.; Deng, N.; Xin, J.; Tang, B. IR-Driven Photocatalytic Water Splitting with WO2-NaxWO3 Hybrid Conductor Material. *Nano Lett* **2015**, *15* (11), 7199–7203. https://doi.org/10.1021/ACS.NANOLETT.5B01581/ASSET/IMAGES/LARGE/NL-2015-01581X_0005.JPEG.

(135) Sabatier, P. Hydrogénations et Déshydrogénations Par Catalyse. *Berichte der deutschen chemischen Gesellschaft* **1911**, *44* (3), 1984–2001. https://doi.org/10.1002/CBER.19110440303.

(136) Parsons, R. The Rate of Electrolytic Hydrogen Evolution and the Heat of Adsorption of Hydrogen. *Transactions of the Faraday Society* **1958**, *54* (0), 1053–1063. https://doi.org/10.1039/TF9585401053.

(137) She, Z. W.; Kibsgaard, J.; Dickens, C. F.; Chorkendorff, I.; Nørskov, J. K.; Jaramillo, T. F. Combining Theory and Experiment in Electrocatalysis: Insights into Materials Design. *Science (1979)* **2017**, *355* (6321). https://doi.org/10.1126/SCIENCE.AAD4998.

(138) Gao, Q.; Zhang, W.; Shi, Z.; Yang, L.; Tang, Y. Structural Design and Electronic Modulation of Transition-Metal-Carbide Electrocatalysts toward Efficient Hydrogen Evolution. *Advanced Materials* **2019**, *31* (2), 1802880. https://doi.org/10.1002/ADMA.201802880.

(139) Vrubel, H.; Moehl, T.; Grätzel, M.; Hu, X. Revealing and Accelerating Slow Electron Transport in Amorphous Molybdenum Sulphide Particles for Hydrogen Evolution Reaction. *Chemical Communications* **2013**, *49* (79), 8985–8987. https://doi.org/10.1039/C3CC45416A.

(140) Wang, J.; Xu, F.; Jin, H.; Chen, Y.; Wang, Y. Non-Noble Metal-Based Carbon Composites in Hydrogen Evolution Reaction: Fundamentals to Applications. *Advanced Materials* **2017**, *29* (14). https://doi.org/10.1002/ADMA.201605838.

(141) Guo, F.; Macdonald, T. J.; Sobrido, A. J.; Liu, L.; Feng, J.; He, G. Recent Advances in Ultralow-Pt-Loading Electrocatalysts for the Efficient Hydrogen Evolution. *Advanced Science* **2023**, *10* (21), 2301098. https://doi.org/10.1002/ADVS.202301098.

(142) Zhou, L.; Lu, S.-Y.; Guo, S. Recent Progress on Precious Metal Single Atom Materials for Water Splitting Catalysis. *SusMat* **2021**, *1* (2), 194–210. https://doi.org/10.1002/SUS2.15.

(143) Boudart, M. *Kinetics of Chemical Processes: Butterworth-Heinemann Series in Chemical Engineering*; 2014.

(144) Boudart, M. Turnover Rates in Heterogeneous Catalysis. *Chem Rev* **1995**, *95* (3), 661–666. https://doi.org/10.1021/CR00035A009/ASSET/CR00035A009.FP.PNG_V03 .

(145) Guo, F.; Macdonald, T. J.; Sobrido, A. J.; Liu, L.; Feng, J.; He, G. Recent Advances in Ultralow-Pt-Loading Electrocatalysts for the Efficient Hydrogen Evolution. *Advanced Science* **2023**, *10* (21), 2301098. https://doi.org/10.1002/ADVS.202301098.

(146) *Microwave Plasma Atomic Emission Spectroscopy (MP-AES) Application EHandbook*.

(147) Balaram, V. Microwave Plasma Atomic Emission Spectrometry (MP-AES) and Its Applications – A Critical Review. *Microchemical Journal*. Elsevier Inc. December 1, 2020. https://doi.org/10.1016/j.microc.2020.105483.

(148) *Schematic diagram explains the principle of MP-AES and REE analysis,... | Download Scientific Diagram*. https://www.researchgate.net/figure/Schematic-diagram-explains-the-principle-of-MP-AES-and-REE-analysis-modified-after_fig2_371387869 (accessed 2024-04-12).

(149) Soares, J. A. N. T. Introduction to Optical Characterization of Materials. *Practical Materials Characterization* **2014**, 43–92. https://doi.org/10.1007/978-1-4614-9281-8_2/FIGURES/19.

(150) Weckhuysen, B. M. *In-Situ Spectroscopy of Catalysts*; American Scientific Publishers, 2004.

(151) Kortüm, G.; Braun, W.; Herzog, G. Principles and Techniques of Diffuse-Reflectance Spectroscopy. *Angewandte Chemie International Edition in English* **1963**, *2* (7), 333–341. https://doi.org/10.1002/anie.196303331.

(152) Bohren, C. F.; Huffman, D. R.; Verlag GmbH, W.-V.; KGaA, C. *Absorption and Scattering of Light by Small Particles*.

(153) Torrent, J.; Barrón, V. *Diffuse Refl Ectance Spectroscopy*; 2008.

(154) Egerton, R. F. *Physical Principles of Electron Microscopy*.

(155) Zhou, W.; Apkarian, R. P.; Lin Wang, Z.; Joy, D. *Fundamentals of Scanning Electron Microscopy*.

(156) Egerton, R. F. *Physical Principles of Electron Microscopy*.

(157) *Nanoscience Instruments | Serving the Nano World*. https://www.nanoscience.com/ (accessed 2024-04-08).

(158) Carter, C. B.; Williams, D. B. *Transmission Electron Microscopy*.

(159) Egerton, R. F. Electron Energy-Loss Spectroscopy in the TEM. *Reports on Progress in Physics* **2009**, *72* (1). https://doi.org/10.1088/0034-4885/72/1/016502.

(160) Bunaciu, A. A.; Udriştioiu, E. gabriela; Aboul-Enein, H. Y. X-Ray Diffraction: Instrumentation and Applications. *Critical Reviews in Analytical Chemistry*. Taylor and Francis Ltd. October 2, 2015, pp 289–299. https://doi.org/10.1080/10408347.2014.949616.

(161) Jung, H.; Jeong, S.; Park, Y.; Shin, Y.; Jeong, H. X-Ray Diffraction Analysis of Damaged Layer During Polishing of Silicon Carbide. *International Journal of Precision Engineering and Manufacturing* **2023**, *24* (1), 25–32. https://doi.org/10.1007/s12541-022-00711-5.

(162) Zhong, X.; Sun, Y.; Chen, X.; Zhuang, G.; Li, X.; Wang, J. G. Mo Doping Induced More Active Sites in Urchin-Like W18O49 Nanostructure with Remarkably Enhanced Performance for Hydrogen Evolution Reaction. *Adv Funct Mater* **2016**, *26* (32), 5778–5786. https://doi.org/10.1002/ADFM.201601732.

(163) Pagnier, T.; Boulova, M.; Sergent, N.; Bouvier, P.; Lucazeau, G. Nanopowders and Nanostructured Oxides: Phase Transitions and Surface Reactivity. *Journal of Raman Spectroscopy* **2007**, *38* (6), 756–761. https://doi.org/10.1002/JRS.1687.

Appendices

Table: Measured the Pt concentration in the standard and samples at different wavelength.

Samples **mg/L**	**Pt 265.945 nm mg/L**	**Pt 292.979 nm mg/L**	**Pt 299.796 nm mg/L**	**Pt 306.471 nm mg/L**	**Average** **mg/L**	**% wt. of Pt**
Blank	0.00	0.00	0.00	0.00	0.00	0.00
Standard 1	1.00	1.00	1.00	1.00	1.00	-------
Standard 2	2.00	2.00	2.00	2.00	2.00	-------
Standard 3	3.00	3.00	3.00	3.00	3.00	-------
Standard 5	5.00	5.00	5.00	5.00	5.00	-------
Standard 7	7.00	7.00	7.00	7.00	7.00	-------
Standard 10	10.00	10.00	10.00	10.00	10.00	-------
Standard 20	20.00	20.00	20.00	20.00	20.00	-------
$Pt_{0.4}/W_{18}O_{49}$	2.02	1.99	2.10	2.13	2.06	0.412
$Pt_{0.8}/W_{18}O_{49}$	4.13	4.08	4.23	4.19	4.16	0.832
$Pt_{1.6}/W_{18}O_{49}$	7.98	8.09	8.34	8.19	8.15	1.629

All the sample prior to AES measurement was prepared 500 mg/L with HCl used as a solvent.

Dispersion image:

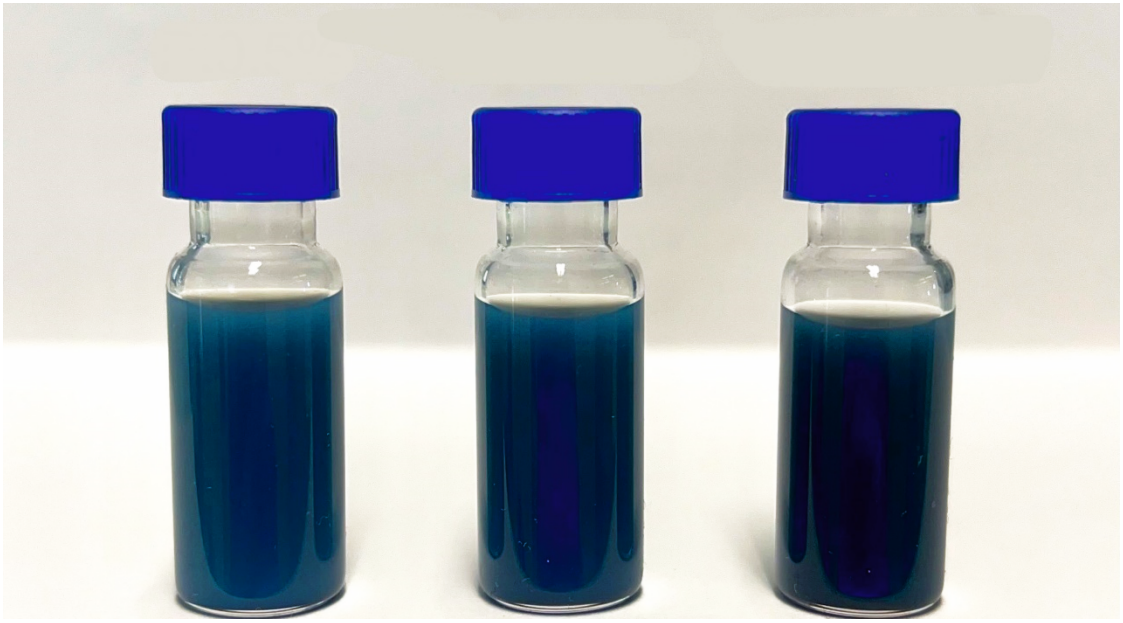

Figure: Samples dispersed on ethanol solvent. From left to right the sample is light blue to deep blue with Pt 0.4% to 1.6% respectively.

SEM image with different Pt amount on the surface of $W_{18}O_{49}$ substrate:

$Pt_{0.4}/W_{18}O_{49}$ with 0.412 % wt. of Pt on the surface

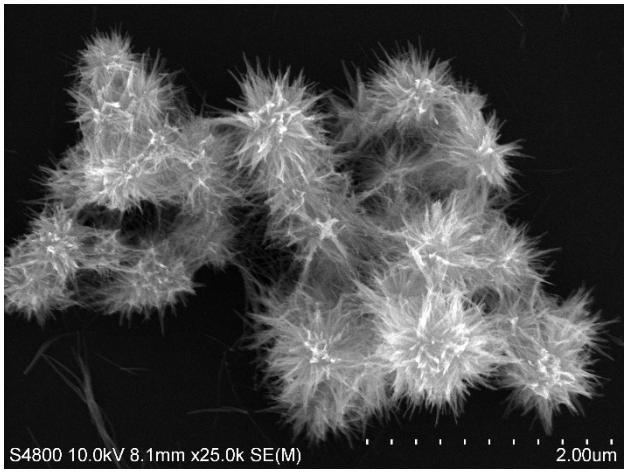

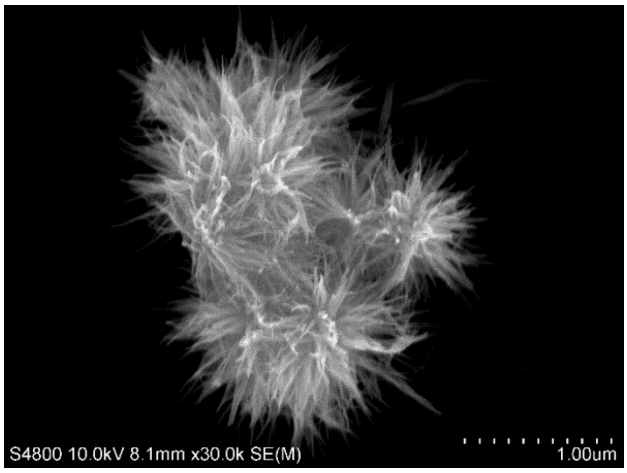

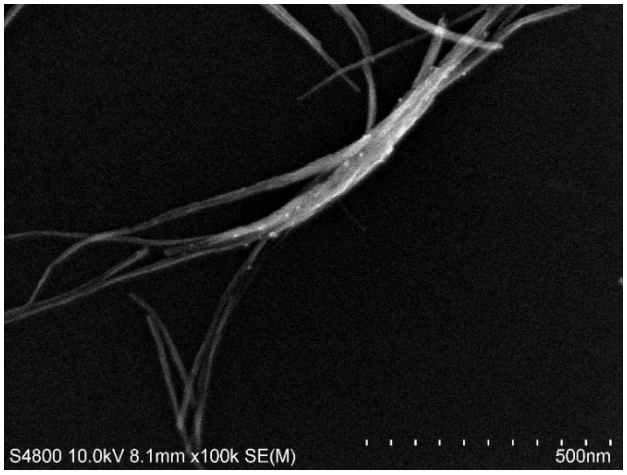

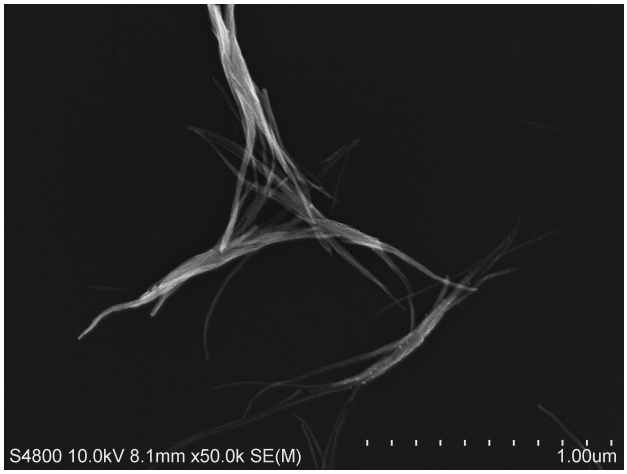

$Pt_{0.8}/W_{18}O_{49}$ with 0.832 % wt. of Pt on the surface

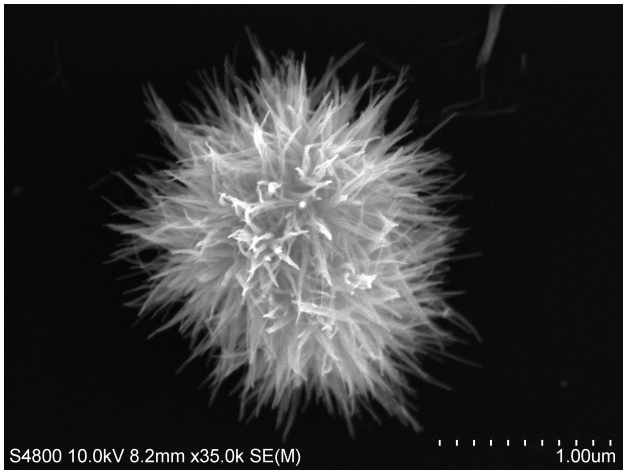

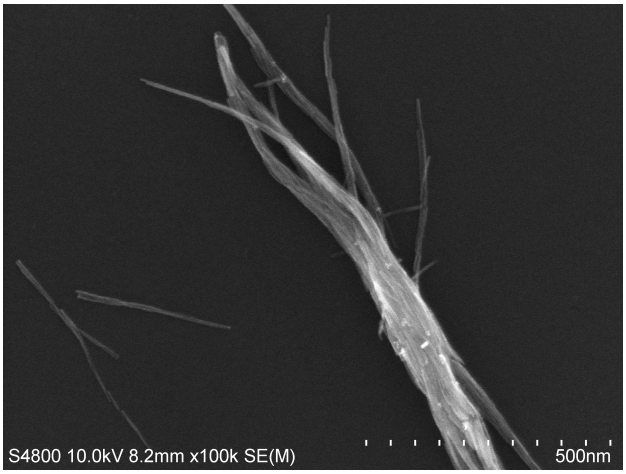

$Pt_{1.6}/W_{18}O_{49}$ with 1.63 % wt. of Pt on the surface

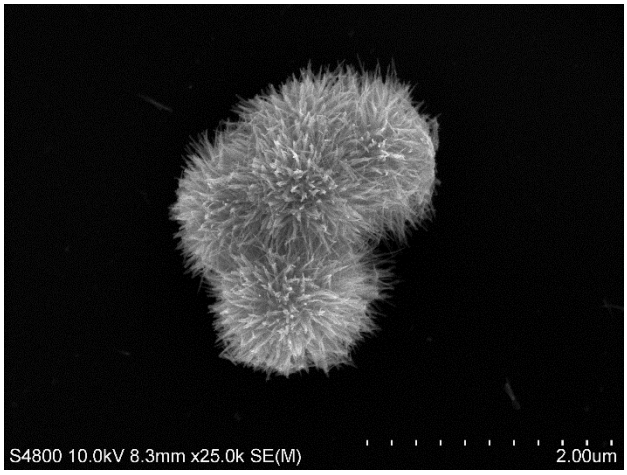

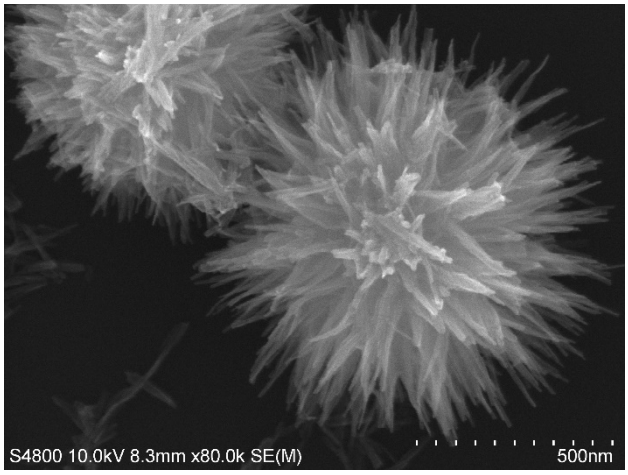

SEM after the stability test (24hr chronopotentiometry):

